# TREX: A SMALL ANTENNA RF SPECTROMETER

by

Saša Nedeljković

A thesis submitted in conformity with the requirements
for the degree of Doctor of Philosophy
Graduate Department of Physics
University of Toronto

Library and
Archives Canada

Published Heritage
Branch

395 Wellington Street
Ottawa ON K1A 0N4
Canada

Bibliothèque et
Archives Canada

Direction du
Patrimoine de l'édition

395, rue Wellington
Ottawa ON K1A 0N4
Canada

*Your file Votre référence*
*ISBN: 978-0-494-39630-8*
*Our file Notre référence*
*ISBN: 978-0-494-39630-8*

NOTICE:
The author has granted a non-exclusive license allowing Library and Archives Canada to reproduce, publish, archive, preserve, conserve, communicate to the public by telecommunication or on the Internet, loan, distribute and sell theses worldwide, for commercial or non-commercial purposes, in microform, paper, electronic and/or any other formats.

The author retains copyright ownership and moral rights in this thesis. Neither the thesis nor substantial extracts from it may be printed or otherwise reproduced without the author's permission.

AVIS:
L'auteur a accordé une licence non exclusive permettant à la Bibliothèque et Archives Canada de reproduire, publier, archiver, sauvegarder, conserver, transmettre au public par télécommunication ou par l'Internet, prêter, distribuer et vendre des thèses partout dans le monde, à des fins commerciales ou autres, sur support microforme, papier, électronique et/ou autres formats.

L'auteur conserve la propriété du droit d'auteur et des droits moraux qui protège cette thèse. Ni la thèse ni des extraits substantiels de celle-ci ne doivent être imprimés ou autrement reproduits sans son autorisation.

In compliance with the Canadian Privacy Act some supporting forms may have been removed from this thesis.

While these forms may be included in the document page count, their removal does not represent any loss of content from the thesis.

Conformément à la loi canadienne sur la protection de la vie privée, quelques formulaires secondaires ont été enlevés de cette thèse.

Bien que ces formulaires aient inclus dans la pagination, il n'y aura aucun contenu manquant.

Canada

# Abstract

TREX: A Small Antenna RF Spectrometer

Saša Nedeljković

Doctor of Philosophy

Graduate Department of Physics

University of Toronto

2007

TREX (21 cm Reionization EXperiment/Trail Reflection EXperiment) is a digital spectrometer with a broadband antenna optimized for frequencies of 70-250 MHz. A frequency-independent rectangular approximation of a two arm conical spiral antenna has been designed, built and tested. I have developed a short integer fast Fourier transform which performs faster than any other known algorithm on Intel platforms. There are two primary scientific goals for TREX: detection of the reionization epoch, and observations of forward scattering of meteors at multiple frequencies.

A method to detect the reionization signature via the red-shifted 21 cm hydrogen line is discussed in detail. If the spectrum signature due to this line is in the form of a sharp "temperature step" of $\sim 0.02K$, it should be possible to detect it by using two specially designed antennas each rescaled by 1% in the frequency range of 150-250 MHz. I have measured the levels of noise in Algonquin Park, Canada, and concluded that activity in the sporadic E layer of the ionosphere seriously affects observations of the 21 cm reionization signature.

Meteor forward-scattering is a well known method of detecting meteors using a radio telescope to receive signals emitted by distant transmitters and scattered from a meteor trail. If the same meteoroid is detected at additional frequencies due to forward scattering of rays coming from spatially separated transmitters, it is possible to estimate where the scattering occurred, and find the meteoroid velocity vector. Previously, there were no known methods to estimate orbital parameters from forward-scattering observations. In this project, a pipeline to find orbital parameters from the observations is developed.

I performed a set of meteor observations at the Algonquin Radio Telescope site and used data to demonstrate the method of measuring the speed of a meteoroid. The data gathered show increased activity during the Lyrid meteor shower as expected. Finally, no evidence was found for the Pegasid shower.

# Acknowledgements

If you strongly believe
that your name should be mentioned here,
then you are most likely right.

# Contents

# List of Figures

# List of Tables

# Chapter 1

# Introduction

Advances in high speed digital electronics and data acquisition have enabled the development of new radio frequency spectrometers capable of exploring exciting astrophysical questions. At the same time, the processing power of affordable computers is becoming sufficient for real time data analysis. A simple instrument to measure spectra up to 250MHz will be presented. The setup is designed to detect the epoch of reionization of the Universe, as well as to conduct forward-scattering meteor observations [86].

## 1.1 Thesis Overview

In this chapter, an overview will be given of the experimental specifications for detecting the signature of the first luminous objects in the Universe. How the setup is used to observe meteor forward-scattering will also be discussed.

The instrument design will be presented in Chapter 2. The antenna beam patterns for a set of conical spiral antennas are shown, and the actual design overview is given. A short integer FFT algorithm using Single Instruction Multiple Data technology is developed and tested. The format for recording the observed data is described.

In Chapter 3, the basics of meteor astronomy with a focus on forward-scattering observation techniques are presented. It is shown that a typical radio meteor trail is in the state of plasma. A simple derivation of the dispersion equation leads to a division of meteor trails into underdense and overdense classes. The numerical condition required to check whether a given trail can be detected in a fixed receiver for a given transmitter is derived. The solution is used to generate meteor footprints and observability functions. An algorithm to find the velocity vector of a meteoroid is also discussed.

Chapter 4 looks at the data gathered using the TREX apparatus described in Chapter 2. The measurements were done in April, June and July of 2006 at Algonquin Radio Observatory, Algonquin Park, Ontario, Canada. The North American FM broadcasting is described, and the Toronto broadcast footprint is found in the observed data. The data also show raised activity for the Lyrid meteor shower, but no evidence for the Pegasids.

The summary, conclusion and ideas for future work are given in the last Chapter.

## 1.2 21 cm Reionization Experiment

The epoch of reionization defines the time when the first luminous objects in the universe were formed. At redshift $5 - 50$ (see Fig. 1.1), the light of the first generation of stars reionized the Universe, ending the Dark Ages. In this section we first briefly describe the history of the Universe, and then focus on a method to measure the time of the reionization.

### 1.2.1 History of the Universe

According to the Big Bang theory, the universe originated from a gravitational singularity about 13.7 billion years ago. After the Big Bang, the distance between any two individual points increases with time. Since the laws of physics are independent of the metric expansion, objects bound by physical forces do not expand. For example, the Earth does not expand together with the expansion of the Universe because of the influence of the gravitational force, but the distance between galaxies increases [103]. During the first

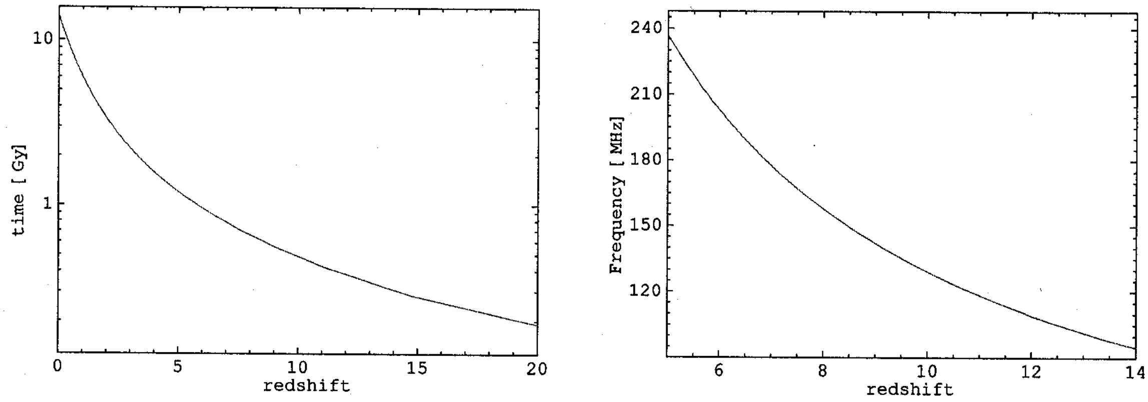

Figure 1.1: Redshift vs age of the Universe (left) and redshift vs frequency of the redshifted 21 cm line for a standard ΛCDM cosmological model.

$10^{-43}$ s, all four fundamental forces were unified and particles did not exist. According to quantum mechanics, it is meaningless to speak of durations shorter than this interval, known as Planck time. At about $10^{-35}$ s, the universe experienced exponential growth during a cosmic inflation period when elementary particles were created. After inflation, these particles were in a relativistic quark-gluon plasma state. The very early Universe was homogeneous and isotropic with high energy density, temperature and pressure. The radiation and plasma were in the thermal equilibrium. Individual photons were absorbed and re-emitted, making the universe opaque to the radiation. With time, space expanded and the Universe cooled. Eventually, the temperature was low enough for quarks and gluons to combine into baryons such as protons and neutrons (at ~1 s). During this process, an unexplained asymmetry between matter and antimatter was created. Later, protons and neutrons formed deuterium and helium nuclei.

After about 300,000 years the temperature of the Universe dropped below 3000 K and electrons and nuclei combined into atoms of mostly hydrogen. As a result, the primordial plasma suddenly became a neutral gas largely transparent to the radiation. Today, the remnant of this primordial radiation is well-known as the cosmic microwave background radiation [33], [106], [19]. The time period when most of the matter in the universe was neutral is called the Dark Ages. The only significant radiation emitted during the Dark Ages is the 21 cm line of neutral hydrogen. The cooling of the cosmic background radiation triggered recombination in the intergalactic medium (IGM) as explained in [103]. The darkness lasted until the formation of the first star-like objects, when the Universe was lit up again.

The new radiation sources, formed from the cold and neutral self-gravitating gas clumps, reheated and reionized the surrounding clouds. The complete physical image of the reionizing sources is yet to be understood, but according to known spectral properties, these objects were more likely stars than quasars [142]. The epoch when ionized HII shells surrounding the first individual sources overlapped is called the reionization epoch, defined by the redshift of reionization $z_{rei}$. Studies of quasar spectra at redshifts $z < 5$ show no absorption of quasar emission redshifted into the Lyman series due to neutral hydrogen along the line of sight. This is known as absence of Gunn-Peterson effect and is attributed to the IGM being highly ionized for $z < 5$ [127]. According to popular models, the first sources of light began to form at redshift $z \approx 50$ and reionized most of the hydrogen in the universe by $z \approx 5$. More optimistic models put limits into the range $20 \geq z_{rei} \geq 5$ [119]. A good overview of the formation of the first star-like objects and their influence on the surrounding media is given by Loeb and Barkana, 2001 [66].

The early universe was very simple, while the universe today is very complex and rich in structure. The first structures were formed due to small irregularities in the density of the universe. The places with larger density attracted more material and became more dense, until eventually the first objects were formed. The light from the first luminous objects ionized the surrounding universe again. Today, most of the gas in the universe is ionized.

### 1.2.2 Probing Reionization with Redshifted 21 cm Hydrogen Line

It is possible to detect the reionization epoch by observing the redshifted hydrogen 21 cm line. Emitted during the Dark Ages, the line disappeared after the reionization epoch, leaving a spectrum signature in the form of a "temperature step". Even though the predicted value for the reionization step is very small compared to the sky noise, using the all sky feature of the reionization signature, I will show that in certain models the step may be measurable with a system of two or more small antennae.

Different methods of measuring $z_{rei}$ have been proposed in the last few years, but the most promising method is looking at the 21 cm hydrogen line [121]. The observed frequency of the temperature step $\nu$ is a function of the redshift $z$ and rest frequency of the 21 cm line, $\nu_{21\text{ cm}} = 1420.4057$ MHz given by

$$\nu = \frac{\nu_{21\text{ cm}}}{1+z}.$$

If the transition from a neutral to almost completely ionized IGM occurred at $20 \geq z_{rei} \geq 5$, the 21 cm line would be redshifted to the interval 70-240 MHz. The relation between redshift and the age of the Universe for the standard $\Lambda$CDM (Lambda-Cold Dark Matter) cosmology is given in Fig. 1.1. The model assumes the Universe to be homogeneous and isotropic on large scales, spatially flat and filled with radiation, dark energy, ordinary and dark matter. Six parameters describing the model can be found in [129].

The 21 cm signature is detectable only if an efficient mechanism exists to decouple the spin temperature from the cosmic background radiation. Otherwise, neither emission nor absorption would be detectable. Two possible processes responsible for the decoupling are collisions between hydrogen atoms, and scattering by Ly$\alpha$ photons. The dominant process, except in very dense IGM regions, is Ly$\alpha$ scattering [76]. As was first pointed out by Field and Wouthuysen [31, 153], this process involves the intermediate transition of an electron to the 2p state, in order to make a hyperfine transition and change the spin direction. During the Dark Ages, the Field-Wouthuysen process would produce a signal which disappears after the reionization epoch, leaving a spectrum signature in the form of a step.

Combining observational and numerically simulated data gives us more than enough inspiration to try to measure the redshift of reionization. Data obtained from quasar SDSS 1044-0125 discovered by Fan *et al,* 2000 provides strong evidence that reionization occurs around $z \approx 6$ [20]. Using numerical simulation, Gnedin suggested that $z_{rei}$ is well defined by looking at the time derivative of the mean free path of ionizing radiation [34].

The detection of the reionization step is not an easy task. In 1997, the observation of two frequency bands with central frequencies corresponding to redshifts 5.0 and 8.5 was proposed [69]. The method requires a still non-existent giant metrewave radio telescope such as the Square Kilometre Array (SKA). The step should be detectable for an Einstein-de Sitter universe with $h = 0.5$, as shown in [121]. It is supposed to be an edge of more than $0.02K$, somewhere between $70 - 240$MHz (Fig. 1 in Shaver et all, 1999 [121], same as Fig. 1 in Shaver and Bruyn, 1999 [120] and Fig. 1 in Tozzi et all, 2000 [137]).

The reionization step should be present over the whole sky, which opens the possibility of detections with a small telescope. The main requirement is to obtain very accurate spectra over the required frequency range. However, when changing frequencies, telescope parameters also change [62]. Even the best small broadband antennas cannot be used in a single mode to measure the step. It only can be measured by using a specially designed system composed of rescaled antennas.

By building a system of two rescaled antennas, the broadband problem may be reduced. If the second antenna is rescaled by a factor $s$, the antenna beam pattern for some frequency $s\nu$ is going to be the same as in the case of the non rescaled antenna at frequency $\nu$. Assuming that synchrotron emmision and the reionization signature are the only two components contributing to the antenna's temperature, the antenna temperature measured by an antenna with the beam pattern $P(\nu, \mathbf{r})$ at frequency $\nu$ is

$$T(\nu) = T_{rei}(\nu)\frac{\Omega_{sky}(\nu)}{\Omega_A(\nu)} + T_{GR}\frac{\Omega_{GR}(\nu)}{\Omega_A(\nu)} + \iint\limits_{sky} P(\nu, \mathbf{r}) T_0(\mathbf{r}) \left(\frac{\nu}{\nu_0}\right)^{\alpha(\mathbf{r})} d\Omega, \tag{1.1}$$

where $T_{rei}$ and $T_{GR}$ are the temperature contribution from reionization and from the ground (back lobes), and $\Omega_A$, $\Omega_{sky}$, $\Omega_{GR}$ are solid angles of the whole antenna, the part of the antenna which can "see" the sky, and the antenna's back lobes, respectively, where $\Omega_{GR} = \Omega_A - \Omega_{sky}$ [61]. $T_0(\mathbf{r})$ is the temperature of a point in the sky defined by the vector $\mathbf{r}$ for the frequency $\nu_0$, and $\alpha(\mathbf{r})$ is the spectral index. The integration is done over the surface of the visible sky.

Equation (1.1) can be simplified using two approximations. Firstly, a specially designed telescope system could completely reflect the sky signal to the antenna's side lobes, and remove the background term. Secondly, if the spectral index can be assumed to be constant over the sky

$$\overline{\alpha} = \iint\limits_{sky} \alpha(\mathbf{r}) d\Omega = const, \tag{1.2}$$

then the difference between temperatures measured by an antenna rescaled by a factor $s$ at the frequency $s\nu$ and a non-rescaled antenna at the frequency $\nu$ is

$$T_1(\nu) - \frac{T_2(s\nu)}{s^{\overline{\alpha}}} = T_{rei}(\nu) - \frac{T_{rei}(s\nu)}{s^{\overline{\alpha}}}. \tag{1.3}$$

In order to adequately simulate the reionization signature observations, we must include all important physical processes. The sky emission in the observed range is composed of galactic synchrotron emission ($\sim 70\%$) with spectral index $\sim -2.6$, galactic thermal emission ($\sim 1\%$), with $\alpha \sim -2.1$, integrated emission from extragalactic sources ($\sim 27\%$), with $\alpha \sim -2.75$, and the 2.73 K cosmic background [61], [65], [80]. In our simulations we unite galactic synchrotron, galactic thermal, and extragalactic synchrotron emission into a single component by using different spectral indices for different directions in the sky. The cosmic background radiation can be included in the reionization signature itself. All-sky maps at 34.5 MHz [22] and 408 MHz [40] are used as boundary conditions for simulating the sky's temperature at different frequencies. The simulated all-sky map at 180 MHz is shown in Fig. 1.2. Because the 34.5 MHz map covers the declination range from −50° to +70° there are three clearly distinct regions in our simulated map.

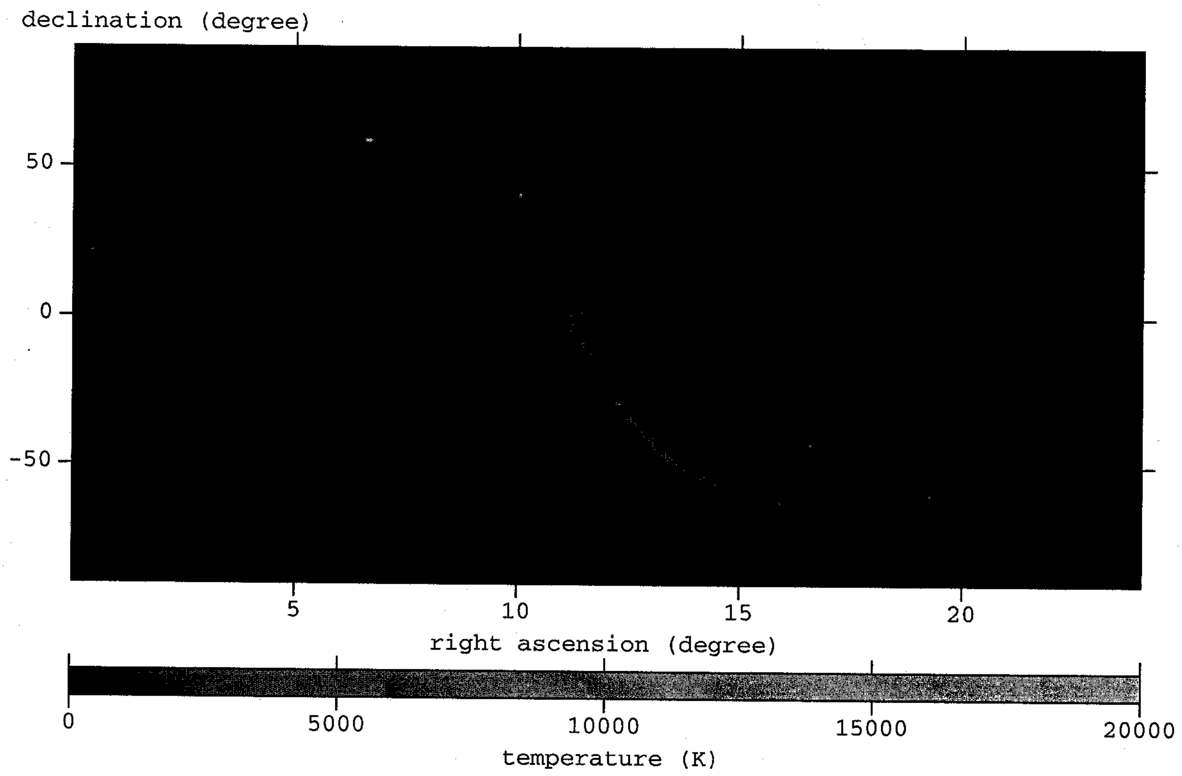

Figure 1.2: Simulated map of the entire sky at 180 MHz in equatorial coordinates.

A conical spiral antenna was chosen for the simulated observation because of its broadband characteristics and relative simplicity [62]. The reionization step from equation (1.3) does not depend on the antenna beam pattern. In a more detailed model, where the spectral index is not constant over the whole sky, the ability to measure the step will depend on the antenna's parameters. For this antenna, the opening angle of the cone is set to $\theta = 15$ degrees, the radius of the top of the cone is $r_{min} = 0.125$ m, and the radius of the bottom of the cone is $r_{max} = 2.25$ m. The design of the antenna, as well as the appropriate beams, will be discussed in the next chapter. To minimize the influence of the Earth's rotation, the antennas in the simulation were pointed toward Polaris. The site of the simulated observation was chosen to have the geographical latitude of 45 degrees North.

The reionization signature is included in the simulation as the function

$$T_{rei} = \begin{cases} T_{step} & \text{for } \nu \leq \nu_1; \\ T_{step}\frac{\nu_2-\nu}{\nu_2-\nu_1} & \text{for } \nu_1 < \nu < \nu_2; \\ 0.0K & \text{for } \nu \geq \nu_2, \end{cases} \tag{1.4}$$

where $T_{step} \sim 0.02$ K, and $\nu_1$ and $\nu_2$ are the beginning and the end of the transition. Fig. 1.3 shows a function $dT = T_1(\nu) - \frac{T_2(s\nu)}{s^{\overline{\alpha}}}$ plotted versus frequency for different rescaling factors of antennas, assuming that the spectral index over the whole sky is constant. Under such assumptions, the reionization signature can be detected (for any rescaling factor) from the graph. For each curve three frequency regions can be discussed. Large frequencies, $\nu > \nu_2$, have $dT = 0$ and define a completely ionized Universe. The transition region is defined with $\nu_2 > \nu > s\nu_1$, and finally the Dark Ages can be seen at frequencies lower than $s\nu_1$.

A more realistic model includes the spectral index variations over the sky. In Fig. 1.4 the reionization signature is given for a normally distributed spectral index, with mean at $-2.7$, and 0.1 variance. The signal was produced for a 24-hour time period using 24-minute steps. By using different sizes of sky with the same spectral index, two curves were produced. For the first run, the sky consisted of $1600 \times 800$ points, all with a different spectral index. In the second run, it was assumed that squares of $2 \times 2$ map points have the same spectral index. The curves strongly depend on the chosen $\overline{\alpha}$. As in figure 1.3, three regions of the signature are present. To be able to see the reionization signature, construction of a system composed of two antennas rescaled by $\sim 1\%$ is needed. Since the signature strongly depends on the step temperature value, rather than the frequency range, it might be detected even with a larger rescaling factor system (see Fig. 1.5).

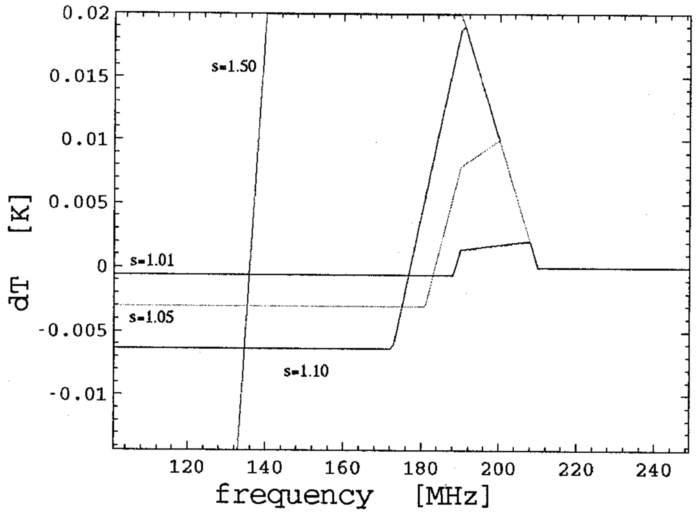

Figure 1.3: The reionization signature $dT = T_1(\nu) - \frac{T_2(s\nu)}{s^{\alpha}}$ versus frequency. The spectral index is constant over the whole sky, $\alpha(\mathbf{r}) = -2.9$, and the reionization step is defined as in (1.4), with $T_{step} = 0.02$ K, $\nu_1 = 190$ MHz and $\nu_2 = 210$ MHz. Different curves are obtained for different antenna rescale factors: $s = 1.5$, 1.1, 1.05 and 1.01.

However, smaller $s$ provides stronger constraints on the reionization epoch.

Using such a model one can conclude that the signature is measurable with the system rescaled by 1% if the reionization of $T_{step} \sim 0.02$ K occurred at redshift $z \lesssim 8$ (frequency $\frac{\nu_1+\nu_2}{2} \gtrsim 150$ MHz), as shown in figure 1.5. A smaller rescaling would give a better view of the reionization epoch, but construction of such a system would be much more difficult.

To obtain the necessary sensitivity and reduce noise, an integration time of $\sim 100$ hours is needed. The minimum detectable temperature $\Delta T_{min}$ is [61]:

$$\Delta T_{min} = \frac{K_s T_{sys}}{\sqrt{\Delta\nu t}}, \tag{1.5}$$

where $K_s$ is a sensitivity constant, $T_{sys}$ is the total system temperature, $\Delta\nu$ is the bandwidth and $t$ is the integration time. For a bandwidth of 1 MHz, with $T_{sys} = 300$ K (overestimated), $K_s \sim 1$ and the needed sensitivity of 0.0002 K, the integration time is $\sim 625$ hours.

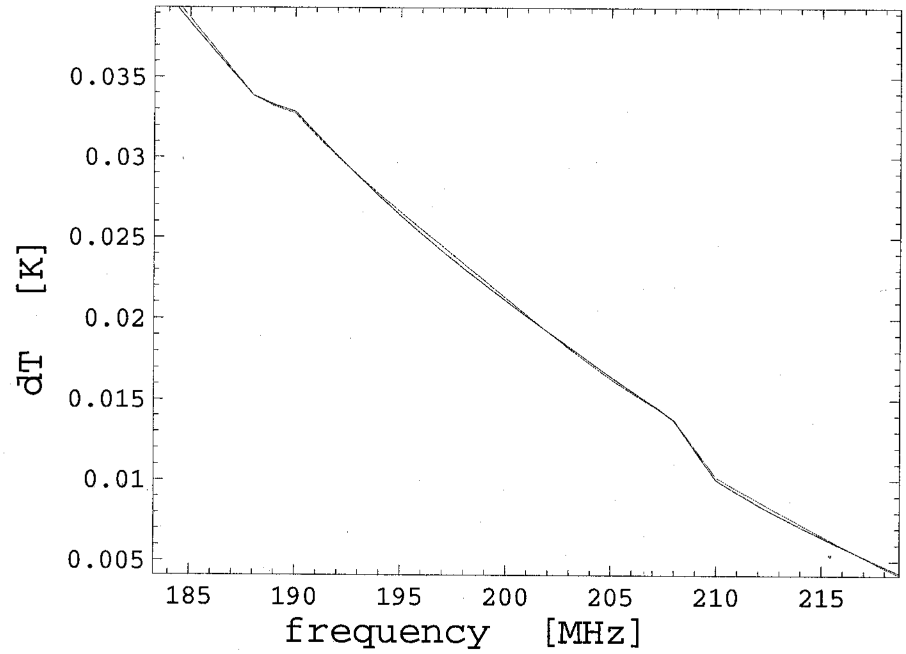

Figure 1.4: The reionization signature versus frequency, plotted with Gaussian distribution of spectral indices over the sky with mean at -2.7 and 0.1 variance. The two curves are obtained by taking different-size sky areas with the same $\alpha$. The rescaling factor is taken to be 1.01, and all other parameters are the same as in Fig. 1.3.

The main sources of potential contamination are the spectral lines and terrestrial interference. Radio lines of various origins occur often in the given radio band, but can be identified and removed with higher resolution spectroscopy. Terrestrial sources are in relatively narrow-bands and vary with time. Interference with FM and TV bands can be avoided by a careful choice of observational site.

There is a number of proposed observatories with the task of probing the epoch of reionization [30]. Many of them are a part of the Square Kilometer Array (SKA) project, a future giant radio telescope with a total collective area of one square kilometer [124]. When finished, SKA will be over 30 times the size of the Arecibo Radio Telescope. The low Frequency Array (LOFAR) is an array of small antennas currently under construction

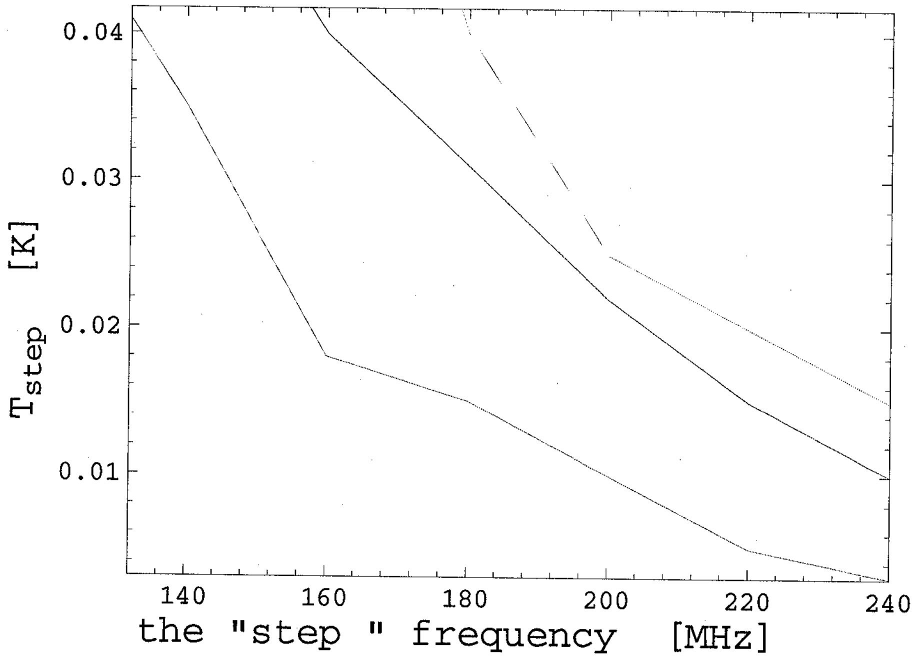

Figure 1.5: Measurable reionization signature as a function of step temperature, frequency $\frac{\nu_1+\nu_2}{2}$ and the rescaling factor. Three different curves were modeled: for $s = 0.1$ (top line), $s = 0.05$ (middle line) and $s = 0.01$ (bottom line). The area above the curves presents the signatures which are possible to measure. The spectral indexes and the antenna beam patterns are the same as in the previous figure. The difference $\nu_2 - \nu_1$ is set to be 20 MHz.

in the Netherlands [45]. It will have 77 stations filled with almost 200 antennas spread over a circle 150 km in diameter. Two types of antennas will scan the sky in two frequency ranges, 30-80 MHz and 120-240 MHz. At the present time, the construction of the first station is almost done and the station is supposed to be operational in 2007 [39]. Another radio array targeting the reionization epoch is the Mileura Widefield Array (MWA) [84]. It will have 8000 dipole antennas optimized for 80-300 MHz. These arrays will have a spatial resolution high enough to look at the fluctuations of the 21 cm reionization signal. This project is still in the planning stage. Other smaller scale experiments will use the all-sky property of the reionization step. The global reionization signature will be a target of the Cosmological Reionization Experiment (CORE) [16]. CORE is a small antenna project, in parts very similar to the system proposed in this thesis. At this time, CORE is still in development.

Success of detection of the global 21 cm reionization step depends on the ability to identify and isolate all the different sources of noise. In the data collected during our observational campaign we have estimated that the stability of the spectrum for a system with a single antenna (Fig. 4.2) is not sufficient enough for performing high precision measurements as required to identify 21 cm reionization signature. Activity in a sporadic E-layer of the atmosphere due to meteor forward scattering interferes with single antenna observations. Removing all meteor-caused signals is very hard since they occur frequently. For our system, we have estimated a meteor flux in FM bands for one year of observations of over $10^{7.6}$ meteors with brightness temperature greater than 500 K. This amounts to more than one meteor reflection per second visible in one of the FM bands. Since the number of meteors with $T < 500$ K is even higher (see Fig. 4.12), it becomes extremely difficult to find a time period without any meteor activity over the needed bandwidth. A possible solution might be to perform integration over each individual frequency band with all meteor detections above certain threshold at a given frequency. However, this approach must be carefully planned, since the 21 cm step intensity is expected to be only $\sim 20$ mK, so just by having more meteor counts below the threshold level at some frequency, and less counts at some other frequency, might lead toward the false 21cm signature detection.

During the past three years, we have tested the levels of radio noise at a number of locations in and around Algonquin Park, Ontario, Canada. As it will be shown in Section 1.4 and Chapter 4, none of these locations are quiet enough for observing the redshifted 21 cm line. The main sources of spectral contamination are man-made transmitters and the activity of the sporadic E layer of the ionosphere (see Chapter 3). Thus, we have decided to shift the focus of this thesis towards the investigation of processes inside the sporadic E layer, in particular, meteor trail detection via forward-scattering. In Chapter 5, we will discuss the effects of this noise on the future 21-cm reionization signature instruments.

## 1.3 Trail Reflection Experiment

Another purpose of the instrument is the detection of meteors through forward scattering [89]. When signals produced by FM radio and TV stations are reflected by a meteor trail, vital information describing the meteor can be extracted. When a meteoric particle enters the ionosphere at a height of 70-160 kilometers, it produces a trail of free electrons due to collisions with air molecules. Any radio wave incident on such a trail is partially scattered. When the transmitter (radio or TV station) is located far enough from the receiver that direct contact is impossible due to the curvature of the Earth, the signal reflected from a meteor trail can be detected. This technique is known as forward meteor scattering. Even when all characteristics of the transmitter and receiver beams are known, the orbital elements of a meteor cannot be resolved. One possible way to find the orbital elements is to have one transmitter and many receivers looking at the same trail. By comparing data from different receivers, the path of the meteoroid can be calculated. In another approach, a system such as TREX, with a resolution of a few kHz, can resolve different terrestrial signals at very high frequencies (VHF). An example of the spectra recorded with TREX is given in Fig. 1.6. All non-field-of-view VHF sources can be used as transmitters for the forward-scattering method. Knowing the frequency, directivity, and the power of the transmitters, and keeping in mind that there are a large number of sources, it is possible to extract all meteor parameters by having only one receiver. The meteor multi-frequency forward scattering observations will be described in detail in chapter 3.

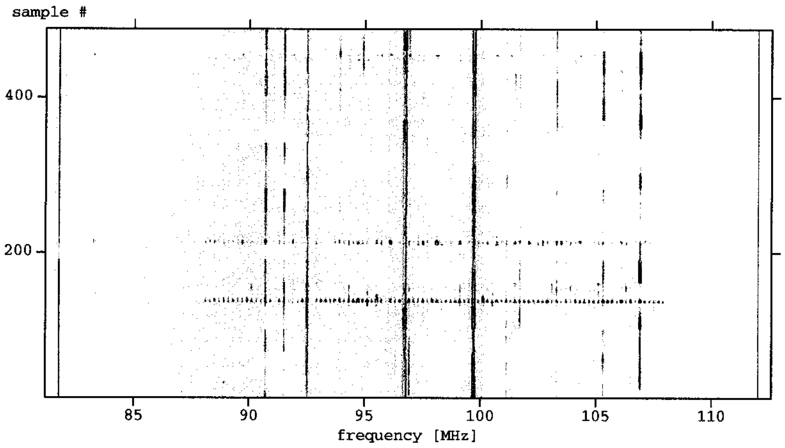

Figure 1.6: The time evolution of spectra showing meteor forward scattering at multiple frequencies. There are 500 spectra sampled over the total collection time of 4.5 minutes. The color defines the intensity at the given frequency. Data was obtained in June 2006 at the Algonquin Radio Observatory.

## 1.4 Choosing the Observing Location

Noise at radio frequencies originates on the ground, in the atmosphere, or in objects on the celestial sphere. Terrestrially produced noise can be roughly divided into two categories: the noise due to the ground or other obstructions within the antenna beam, and man-made noise. Depending on the antenna directivity, the main fraction of the received signal comes from the area where the main lobe is pointing. There is also a contribution due to the side and back lobes which depends not only on the antenna's parameters but also on factors such as the antenna's elevation, ground composition and the ground structure. Man-made noise includes commercial transmissions, as well as unintended radiation from electrical equipment including power transmission lines. Atmospheric noise can roughly be explained by the emission from atmospheric gases due to different atmospheric processes such as lightning. Last but not least is the noise coming from celestial radio sources. It grows exponentially toward lower frequencies.

Man-made interference can be the source of signal masking and contamination of astronomical signals. The radio spectrum is divided into bands designated for different

| Frequency (MHz) | Description |
|---|---|
| 0.030 - 0.535 | maritime and aeronautical communications and navigation, international fixed public band |
| 0.535 - 1.705 | standard AM band broadcasting |
| 1.705 - 30 | amateur radio, LORAN, government radio communications, international shortwave broadcasting, fixed and mobile communications,<br>radio navigation, industrial, scientific and medical equipment |
| 30 - 50 | government and non-government communications, fixed and mobile |
| 50 - 54 | amateur radio |
| 54 - 72 | television channels 2 to 4 |
| 72 - 76 | government and non-government services, fixed and mobile |
| 76 - 88 | television channels 5 and 6 |
| 88 - 108 | FM radio |
| 108 - 137 | aeronautical navigation |
| 137 - 174 | government and non-government communications, fixed and mobile, amateur |
| 174 - 216 | television channels 7 to 13 |
| 216 - 470 | amateur radio, government and non-government communications, fixed and mobile,<br>air traffic radio navigation |
| 470 - 608 | television channels 14 to 36 |
| 608 - 614 | radio astronomy, mobile |
| 614 - 806 | television channels 38 to 69 |
| 806 - 3,000 | aeronautical radio navigation, amateur radio, government and non-government communications, fixed and mobile, television broadcasting,<br>digital audio broadcasting |
| 3,000 - 30,000 | government and non-government communications, fixed and mobile, amateur, radio navigation,<br>direct-to-home satellite broadcasting |
| 30,000 - 300,000 | experimental, government, amateur, fixed |

Table 1.1: Canadian spectra allocation: radio bands from 30 kHz to 300 GHz.

purposes. Canadian radio band allocations are presented in Table 1.1. Radio signals of astronomical origin are far weaker than the signals used by terrestrial communication systems. Interference can result in "bad data" and often cause a completely wrong scientific interpretation. Fig. 1.7 shows a signal leaking from one FM band into the surrounding radio frequency (RF) bands.

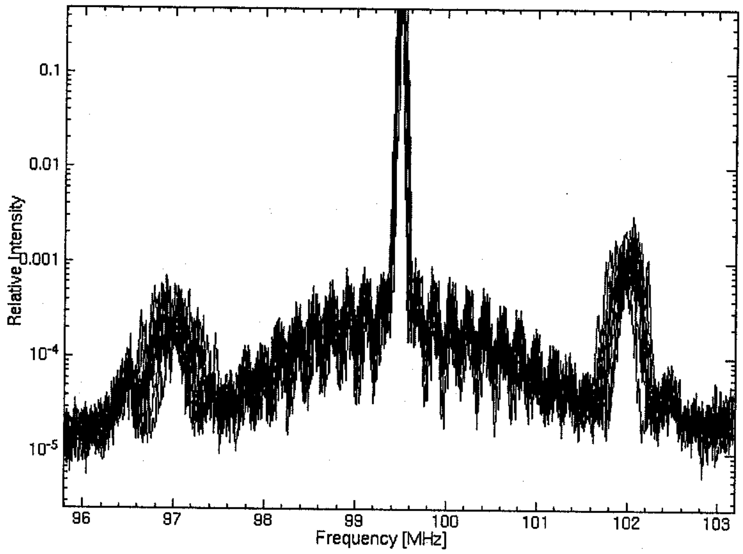

Figure 1.7: An example of RF interference: the FM transmitter at Bracebridge owned by the Haliburton Broadcasting Group Inc, emitting an FM signal at 99.5 MHz, pollutes the surrounding spectra from 96.5 MHz to 102.5 MHz. All 10 measurements taken during the summer of 2004 are plotted.

For the purpose of meteor observation we use FM commercial transmitters as a source for forward-scattering. FM stands for "Frequency Modulated". Frequency modulation is a type of angle-modulated signal where the information is transmitted by changing the frequency of the signal. If the information to be transmitted is in the form $x(t)$, limited in magnitude as $|x(t)| \leq 1$, the FM modulation is defined by using a carrier of the form $A\cos(2\pi f_C t)$:

$$FM(t) = A\cos\left(2\pi \int_0^t f(\tau)d\tau\right) = A\cos\left[2\pi \int_0^t (f_C + \Delta f \; x(\tau))\, d\tau\right],$$

where $f_C$ is the carrier frequency, $A$ is the amplitude, $f(\tau)$ is the frequency of the oscillator and $\Delta f$ is the maximal frequency shift with respect to the carrier frequency. In North America, the FM radio band goes from 87.9 MHz up to 107.9 MHz. In order to resolve two FM signals arriving at two successive frequencies, the frequencies have to be 200 kHz apart. Knowing that the total FM bandwidth is 20 MHz, and that the stations must be 200 kHz apart, there cannot be more than 100 stations visible in the whole FM band.

Worldwide, there are very few exceptions to the FM spectrum as defined in North America. Japan is using a completely different FM radio band from 76-90 MHz, with a band separation of 100 kHz. Some Eastern European countries are still using OIRT (Organisation Internationale de Radiodiffusion et de Télévision), at frequencies of 65.9-74.0 MHz separated by 30 kHz. An example of an OIRT FM transmitter is Radio Kultura in Minsk, Belarus, transmitting at 71.9 MHz. Presently, OIRT broadcasters are vanishing in favor of the standard FM.

The maximal range of an FM signal depends on the curvature of the Earth, the terrain configuration and the positions of the receiver and transmitter. The ionosphere, under normal conditions, does not influence the propagation of FM waves. One should keep in mind that signals can be reflected from mountains and buildings. To calculate the maximal line-of-sight distance one can "hear" an FM station, one can use a 2D approach. Let us assume that the Earth has a perfect spherical shape on a 2D image defined by a

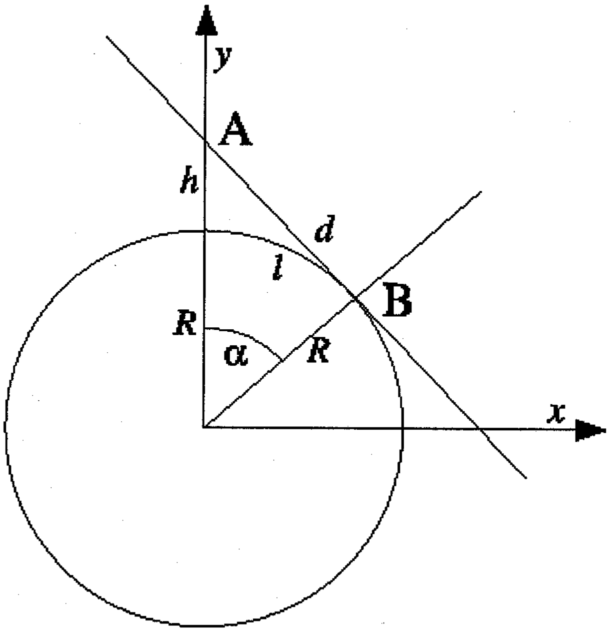

Figure 1.8: Maximal line-of-sight distance from the transmitter.

circle with equation

$$x^2 + y^2 = R^2 \tag{1.6}$$

where $R = 6.38 \times 10^6$ m is the Earth's radius, and $x$ and $y$ define the surface of the Earth. We set a coordinate system in such a way that the top of the transmitter is on the $y$-axis and the coordinate center is at the center of the Earth (Fig. 1.8) The maximum line-of-sight distance $d$ of a receiver (point B) at zero altitude, from the transmitter (point A) at an altitude $h$, is defined by the line tangential to the circle, defined by equation (1.6) passing through A. The slope $a$ of the tangent line ($y = ax + b$) is

$$a = \frac{dy}{dx} = \frac{-x_B}{y_B} = \frac{x_B}{\mp\sqrt{R^2 - x_B^2}},$$

where $x_B$ and $y_B$ are the coordinates of point B.

The second condition is that the point A($x_A = 0$, $y_A$) lies on the tangent $y_A = ax_A + b$. Thus $b = y_A$ (see Fig. 1.8). The point B($x_B$, $y_B$) is also on the tangent $y_B = ax_B + y_A$ resulting in

$$y_B = \frac{x_B}{\mp\sqrt{R^2 - x_B^2}} x_B + y_A.$$

After substituting $y_B = \pm\sqrt{R^2 - x_B^2}$ the previous equation becomes

$$R^2 - x_B^2 = \mp x_B^2 \pm y_A \sqrt{R^2 - x_B^2}.$$

Assuming that the solution is in the 1st quadrant

$$x_B = \frac{R}{R+h}\sqrt{h^2 + 2Rh},$$

$$y_B = \frac{R^2}{R+h}.$$

Once the position of point B is known, it becomes straightforward to determine the angle $\alpha$ and the corresponding arc $l$:

$$l = R\alpha = R \arctan \frac{\sqrt{h^2 + 2Rh}}{R}. \tag{1.7}$$

The maximal arc distance a receiver (at sea level) can receive a line-of-sight signal from a transmitter at an altitude $h$ (from sea level) is given by expression (1.7).

The famous CN Tower is often credited as the tallest building in the world. Located in Toronto, Canada, and completed in 1976, the tower is 553 meters high (including antennas). Using equation (1.7), the distance one can receive a signal emitted from the CN Tower is found to be about 85 km.

The maximum distance of the transmitter for forward-scattering observations depends on the height of the scattering point. For a meteor height of 160 km, the maximum distance between a transmitter and a receiver is about 2800 km.

### 1.4.1 Broadcasting in North America

A database with all FM, AM and TV broadcasting information for all of Canada and border regions of the USA is available on the Canadian Government, Industry Canada, Spectrum Management and Telecommunication website [130]. The USA equivalent of the Canadian broadcast database system is FMQ FM Radio Database Query, operated by the Audio Division of the Media Bureau, USA federal government [140].

Both databases were used to create a full North American map of FM transmitters. In total there are 38313 FM transmitters. The map is plotted in Fig. 1.9. The histograms of horizontal and vertical power emitted are shown in Fig. 1.10 and the distribution of the frequencies in Fig. 1.11.

It is not easy to find a radio quiet area to perform radio astronomical observations. Rapid industrial growth requires constant development of new telecommunication services. The government controlled radio spectrum is fully allocated up to almost 300 GHz with very few windows available for astronomical observations. As shown in Fig. 1.9, North America is almost completely covered with FM radio waves. Only inaccessible regions such as the northern parts of Canada are radio quiet. Hard terrain, polar climate, lack of roads and living facilities makes potential observations from these areas expensive. An example of a suitable place for observation of the 21 cm reionization signal is the northern part of Baffin Island, Nunavut.

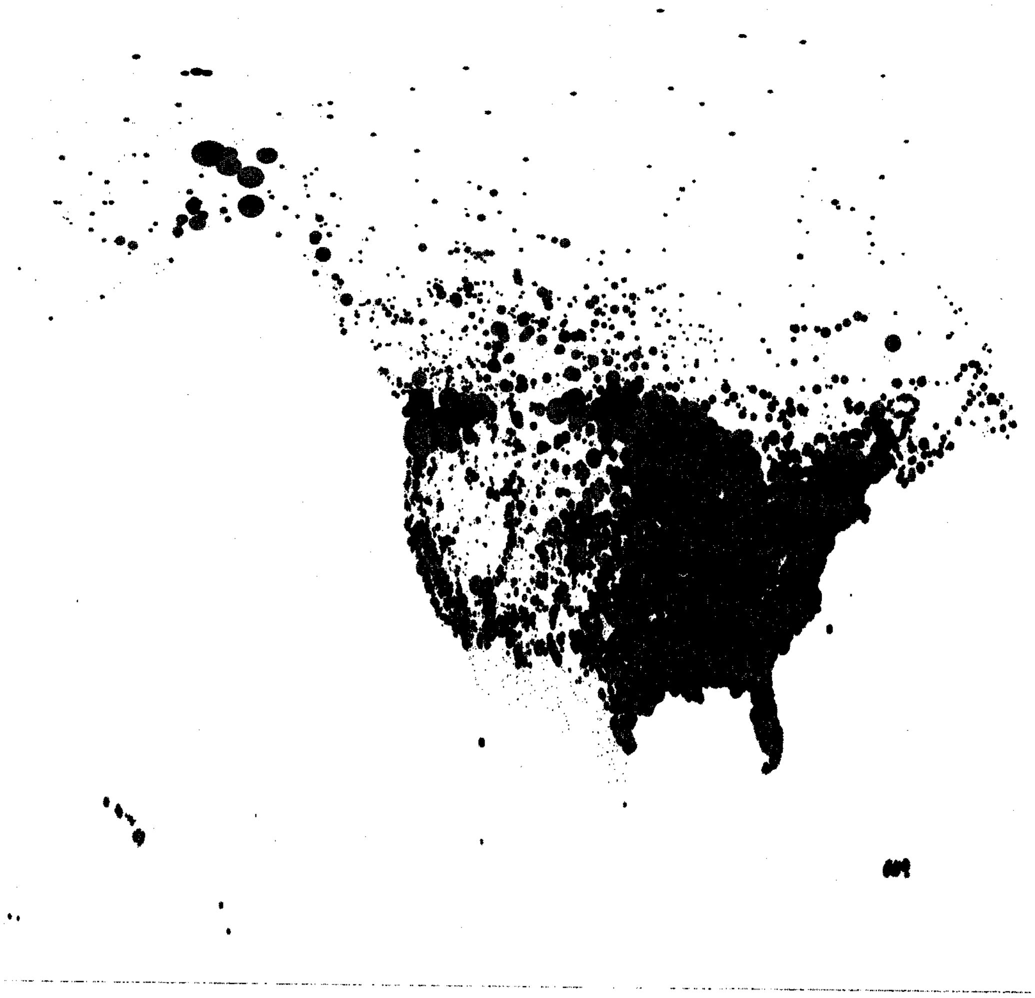

Figure 1.9: North American FM coverage

Observations of meteor scattering do not need a perfectly radio silent location. Algonquin Park, located in the Canadian province of Ontario offers 7,725 square kilometers of forests, lakes, and rivers isolated from modern life. In the heart of the park is the Algonquin Radio Observatory. It is a relatively quiet observational place with road access and electric power. During 2005 and 2006 I performed a set of observations from the Algonquin Radio Observatory (see Chapter 4).

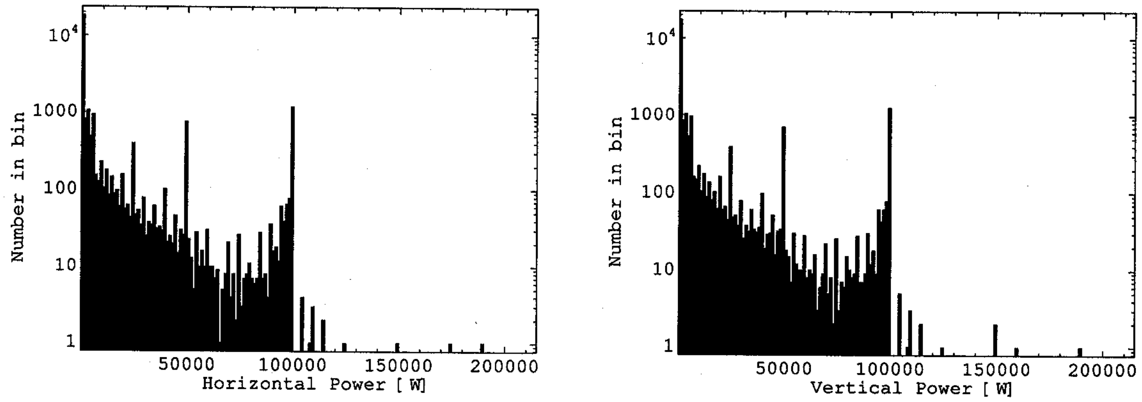

Figure 1.10: Histogram of horizontal (left) and vertical (right) power for all North American FM transmitters.

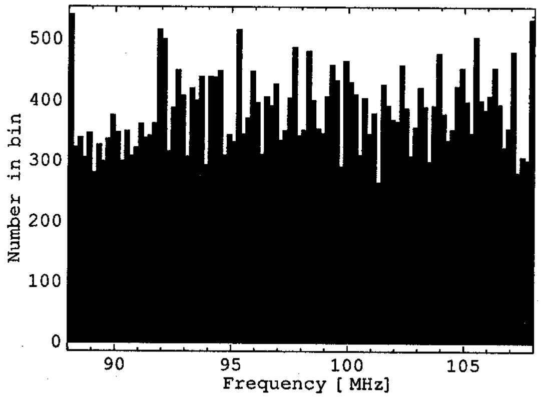

Figure 1.11: Distribution of the frequency bands for all North American FM transmitters.

## 1.5 Other Applications

On July 30, 2004 at 14:22 local time a solar burst was recorded at multiple frequencies. The solar activity was observed from the roof of the University of Toronto Physics Department building from Jul 20 to Aug 10, 2004. A log-periodic antenna was attached to two 20 dB amplifiers, a bandpass filter, a 500 MHz A/DC and a computer. In Fig. 1.12 the signal intensity at 47 MHz is shown for July 30, 2004 from 14:03 until 19:36 local time. The first peak is in excellent agreement with the U.S. Dept. of Commerce, NOAA, Space Environment Center solar event list [94]. The remaining peaks are periodic and are most likely oscillations inside the ionosphere.

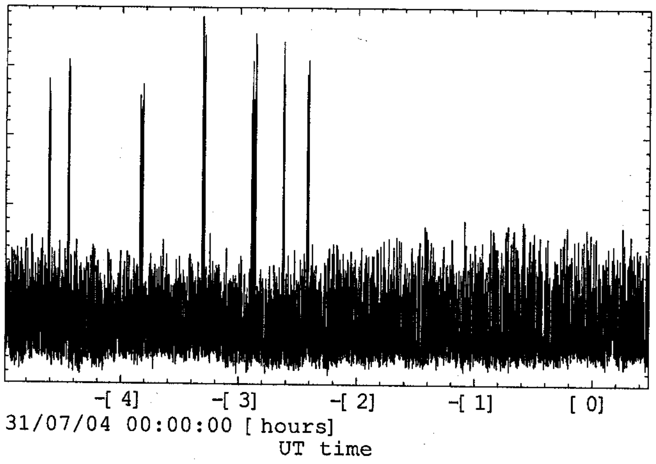

Figure 1.12: Solar Burst observed on July 30, 2006, Department of Physics, UofT: UT time vs intensity in arbitrary units at 47 MHz.

# Chapter 2

# The Instrument

The need for better resolution, larger collecting area, and higher sensitivity in different radio bands has led to the development of a new generation of radio telescopes. Previous designs, such as the Arecibo radio telescope, are based on the use of mixers and other analog elements (see Fig. 2.1). These older telescopes are convenient for narrow band observations. We designed a completely digital solution for wide band scanning of frequencies up to 250 MHz, in short, a digital spectrometer. Its is essentially a system composed of an antenna, an amplifier, an A/D converter and a computer.

An introduction to the theory behind two arm conical spiral antennas (2ACSA) will be given in section 2.1. 2ACSAs have uniform performance characteristics over a wide range of frequencies. The construction of a 2ACSA is a complex and high cost process, so we have considered different approximations in order to obtain a design with frequency independent beam patterns in addition to structural simplicity.

The setup must include filters and amplifiers used to isolate and amplify the needed portion of the spectra. In the case of TREX, a 50-200 MHz band pass filter is used as an anti-aliasing filter to limit the bandwith of the signal.

The amount of data collected per second exceeds the transfer rate of all commercially available A/D converters, which are typically capable of transfering only a few MB/sec,

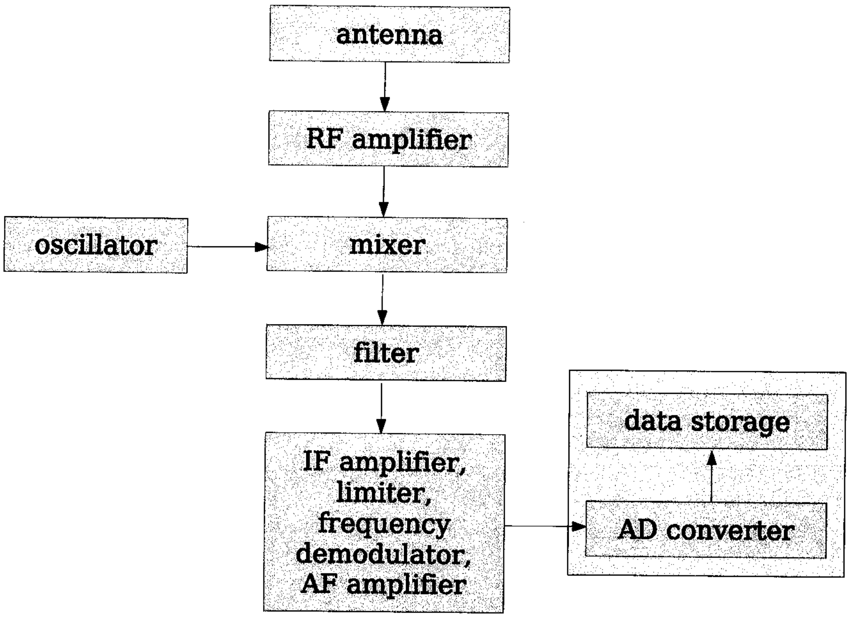

Figure 2.1: Radio Receiver schematics. The old approach.

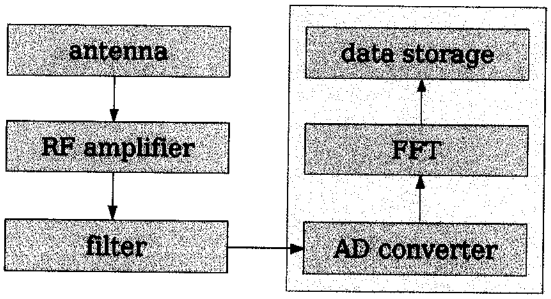

Figure 2.2: TREX schematics.

leading to very inefficient data acquisition. In section 2.2 it will be shown that in order to obtain spectra up to 250 MHz the data sampling has to be done using a 500 MHz or faster A/D converter. An ongoing project to develop a faster A/D converter and acquisition system using 64 bit PCI-X is underway at the Physics Electronics Resource Centre at the University of Toronto. Such a design will permit the streaming of all data to computer memory in real time.

After the raw data are received in the main memory, a fast Fourier transform (FFT) needs to be performed to obtain the power spectrum. FFT calculation is a very computationally intense task. $N$-point FFT uses $\frac{1}{2}N\log_2 N$ operations. Two well known fast FFT packages are FFTW (Fastest Fourier Transform in the West) and Intel's IPP (Integrated Performance Primitives). These algorithms are optimized for working with floating-point numbers.

I have developed an FFT algorithm using integer, rather than floating-point arithmetics, to additionally speed up the calculations. As will be shown in 2.3.1, Intel's processor streaming SIMD (Single Instruction Multiple Data) extensions were used to speed up the FFT algorithm by adapting it to specific hardware; in this case, a Pentium 4.

## 2.1 Rectangular Approximation of Two Arm Conical Spiral Antenna

The theoretical basis for the 2ACSA was given in the 1950s. In 1957, Rumsey [114] suggested two necessary conditions for constructing a frequency-independent antenna: the angle principle and the truncation principle. The angle principle claims that the performance of an antenna defined entirely by angles will be frequency independent. Such a principle does not set any constraints on the size of the antenna, so in general it implies an infinite geometry and at the same time an infinite frequency range. For practical usage, the truncation principle states that the antenna must have an active region of finite size. An active region could be defined as the part of the antenna that contributes to absorbing radiation at a given frequency. By changing the frequency, the active region also changes. If the antenna dimensions are expressed in terms of the wavelength, all proportions must stay the same.

In the case of the conical spiral antenna, the active region at a given wavelength $\lambda$ occurs when $\frac{2\pi\rho}{\lambda} \approx 1$, where $\rho$ is the radius of the antenna region. The active region changes from the small end to the large end as the wavelength changes from the minimal

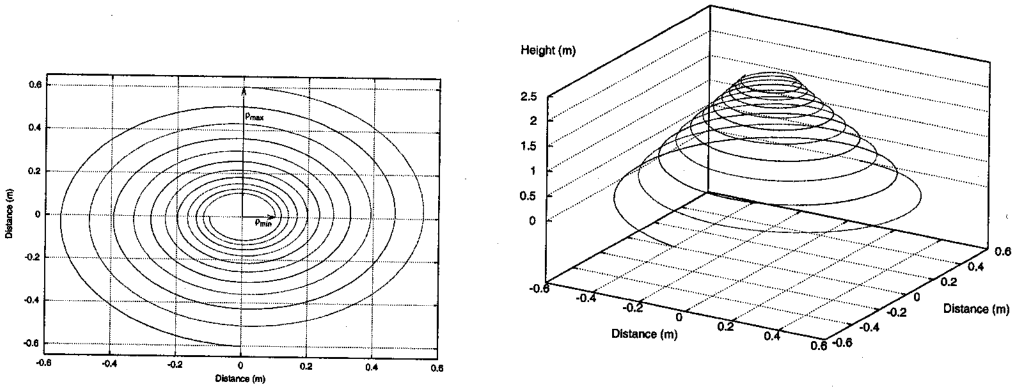

Figure 2.3: The top and side views of 2ACSA. Parameters used are $\rho_{min} = 0.1$ m, $\rho_{max} = 0.6$ m and $h = 2.5$ m.

to the maximal value. Fig. 2.3 shows 2ACSA with $\rho_{min} = 0.1$m and $\rho_{max} = 0.6$m.

For measurements requiring a high precision antenna beam pattern, the symmetry of the antenna should be preserved. A signal from the antenna passes through a number of components, called antenna feed, before reaching an amplifier. There are significant problems with designing a feeding system due to the fact that the feeding starts from the smaller end of the antenna (the top of the antenna). A submarine antenna system proposed by Dyson, 1959 [23] and later by Wills, 1985 [151], has the feeding coaxial cable carried along the antenna arm. To preserve symmetry, an unused (dummy) coaxial line is carried along the other antenna's arm. This technique reduces the unbalanced mode on the line significantly.

In 1967, Yeh and Mei numerically solved the electromagnetic antenna equations for the thin-wire model in which the antenna's arms are modeled with a wire of constant radius [156]. The radius must be much smaller than the wavelength. However, according to Rumsey's first principle, all antenna parameters must be defined by angles, and obviously, the thin wire model is not completely frequency independent. A better model includes arms expanded in width: the thinnest at the cone apex and thickest at the base of cone. In this work we will use the thin wire approximation.

In the thin-wire approximation, the conical spiral antenna is designed by winding two or more wires around the surface of a truncated cone. Two angles define such an antenna: the half angle of the cone $\theta$ (between the symmetry axis and the side of the cone) and the wrap angle $\alpha$. For $\theta = 90°$ the antenna becomes a pure 2-dimensional spiral. The wrap angle is the angle between the spiral arm and the radial line from the apex of the cone. The smaller and the larger ends of the cone are defined with the diameters $d_{min}$ and $d_{max}$.

The 2-dimensional mathematical equation of the logarithmic spiral is

$$\rho = ae^{b|\phi|}, \tag{2.1}$$

where the radius $\rho$ and the angle $\phi$ are the standard cylindrical coordinates, while $a$ and $b$ are constants. $\phi$ can take values from 0 to $\infty$. Using this equation, the conical spiral antenna arm is defined with

$$r_1(\phi) = r_d e^{b|\phi|}, \tag{2.2}$$

where $r_1$ is the radial distance from the cone apex to a point on the conical surface. The constant $b$ can be expressed in terms of the antenna angles $\theta$ and $\alpha$ as

$$b = \frac{\sin\theta}{\tan\alpha}.$$

The value of $r_d$ can be calculated from the boundary conditions by putting $\phi = 0$ into equation (2.2) to give

$$r_d = \frac{d_{min}}{2\sin\theta}.$$

A two arm CSA will have two symmetric arms with respect to the $z$-axis. The second arm can be obtained by rotating the first arm by the angle $\pi$, while keeping $z$ constant. For the second arm, the radial distance from the cone apex $r_2$ is

$$r_2(\phi) = r_d e^{b(|\phi|-\pi)}, \quad |\phi| \geq \pi. \tag{2.3}$$

### 2.1.1 Modeling Rectangular 2ACSA

I have developed a generic algorithm for designing a rectangular approximation of a conical spiral antenna. I used equations (2.1-2.3) to find a set of points defined with an increment $\Delta\phi$ of the angle $\phi$. $\Delta\phi$ is chosen in such a way that $\frac{2\pi}{\Delta\phi}$ is an integer, so that the number of antenna sides for a single antenna stays fixed. In the general case, the offset should be set accordingly to the number of sides as $\frac{2\pi}{N_{sides}}$. Each two successive points of the same arm are connected linearly taking into account the limitations of the analysis software. In the simplest possible model, the angle $\phi$ takes values of $2k\pi$, $\frac{1}{3}\pi + 2k\pi$ and $\frac{2}{3}\pi + 2k\pi$, where $k$ is a non-negative integer. The structure obtained has the symmetric shape of the Star of David when seen from the top. By taking values $k\pi$ and $\frac{k}{2}\pi$ for $\phi$, a rectangular structure is defined, as shown in Fig. 2.4.

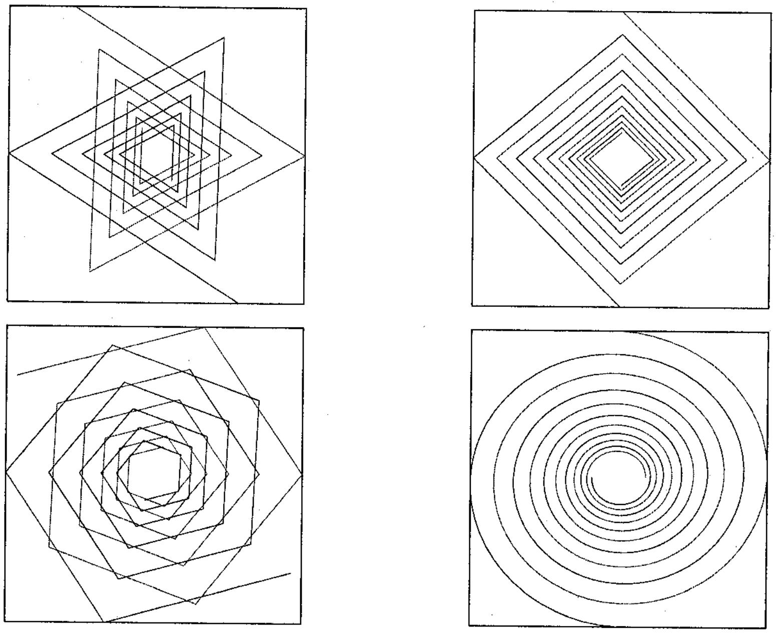

Figure 2.4: Top view of the four different approximations of 2ACSA with $\Delta\phi = \frac{2\pi}{3}$ (top left), $\frac{\pi}{2}$ (top right), $\frac{2\pi}{5}$ (bottom left) and $\frac{\pi}{30}$ (bottom right). The other parameters are set as in Table 2.1.

I have written an algorithm to find the antenna having the most symmetric beam pattern with the smallest possible back and side lobes. The dimension of the antenna should be on the order of a few meters. The required specifications are given in Table 2.1. The inner and outer radius set the constraints on the active regions of the antenna for the required minimal and maximal frequencies. The cone angle $\theta$ depends on the height and the base of the antenna.

| **Symbol** | **Value** | **Info** |
|---|---|---|
| $h$ | $\sim 3$ m | Total cone height |
| $\rho_{min}$ | $\sim 0.1$ m | Inner radius |
| $\rho_{max}$ | $> 0.6$ m | Outer radius |
| $f_{min}$ | 70 MHz | Minimal frequency |
| $f_{max}$ | 250 MHz | Maximal frequency |
| $\theta$ | $\arctan \frac{\rho_{max}}{h}$ | Cone angle |
| $\alpha$ | $\sim 1.3$ rad | Wrapping angle |
| $\Delta l$ | 0.25 m | The largest distance between antenna points |
| $\Delta\phi$ | $\frac{2\pi}{3}, \frac{\pi}{2}, \frac{2\pi}{5}, \frac{\pi}{30}$ | Determines the shape of the antenna |
| $r_{wire}$ | 0.001 m | Radius of the wire |
| $c$ | 50 MS/m | Conductivity of the copper wire |

Table 2.1: The parameters used for testing 2ACSA.

The antenna beam pattern $P_f(\alpha, \delta)$ represents the response of the antenna at the given frequency as a function of direction, described by the angles $\alpha$ and $\delta$ of an equatorial coordinate system. In short, the beam pattern defines the region of the sky where the antenna emits or receives radiation. The normalized power pattern is defined as

$$P_{f,n}(\alpha, \delta) = \frac{1}{P_{f,max}} P_f(\alpha, \delta), \tag{2.4}$$

where $P_{f,max}$ is the maximal response.

The main beam or main lobe of an antenna is defined as the lobe with the largest maximum. Other lobes are called minor, or side and back lobes. The power received from the main lobe $P_M$, can be obtained by integration over the main lobe solid angle

$$P_M = \iint\limits_{\substack{main\\lobe}} P_{f,n}(\alpha, \delta) d\Omega, \tag{2.5}$$

where $d\Omega = \sin\delta d\alpha d\delta$.

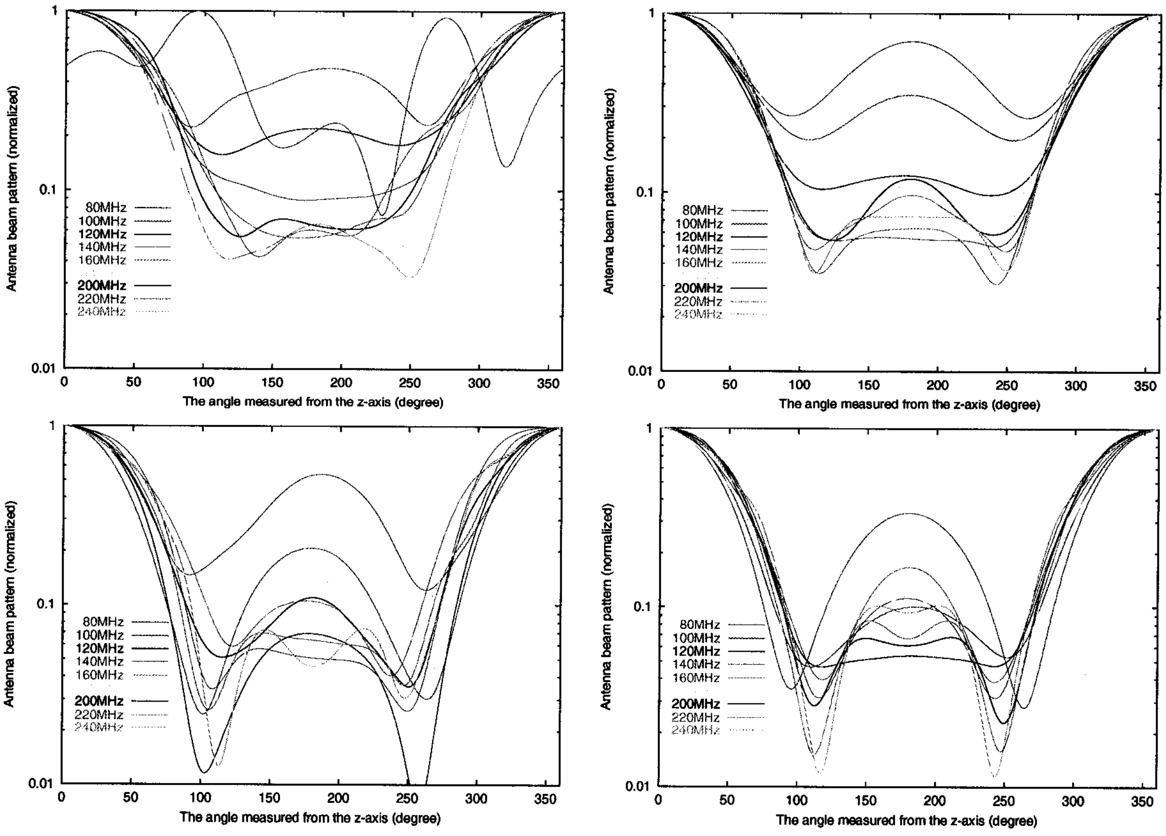

Figure 2.5: Antenna beam patterns for the 2ACSAs in Fig. 2.4 with the parameters as given in Table 2.1 with $\theta = 0$ ($h = 0$).

The radiation from a conical spiral antenna on the $z$-axis is maximal in the direction defined by the smaller end of the cone. In this direction the electric field is mostly circularly polarized.

The antenna characteristics were studied for different frequencies using the open source "Antenna Scatters Analysis Program (ASAP)" written by Jerry Wayne McCormack [73], as well as with the commercial software EZNEC [131]. The limitations of both packages are that the wire radius is supposed to be less than 0.01 m with the longest segment less than 0.25 m and the shortest segment less then 30 wire diameters.

The antenna beam patterns are plotted for a range of frequencies of interest for each of the structures given in Fig. 2.4. In the simplest scenario, where the height is set to be zero, the normalized antenna beam patterns are shown in Fig. 2.5. Clearly, in the case of the antenna shaped like the Star of David $(\Delta\phi = \frac{2\pi}{3})$, the beams are not very symmetric. All four antennas have big back lobes compared to the main ones, especially at lower frequencies. It is interesting to notice that the square approximation with $\Delta\phi = \frac{2\pi}{4}$ has very symmetric beams similar to the spiral case simulated with $\Delta\phi = \frac{2\pi}{30}$. The frequency dependence of the beam patterns is not obvious from these graphs.

The simulation shows that the antenna characteristics can be improved by changing the cone angle $\theta$. In figures 2.6 and 2.7, the normalized antenna beam patterns are plotted for the same set of four antennas but with $\theta = 30°$ and $\theta = 45°$, respectively.

Looking at the plots given in Fig. 2.5, 2.6 and 2.7, it can be seen that a suitably tuned rectangular 2ACSA with $\Delta\phi = \frac{2\pi}{4}$ has the potential to approximate a two arm conical spiral antenna well enough for the high accuracy observations in the needed frequency band.

By changing the number of wire wraps (the wrapping angle $\alpha$), the bandwidth properties of the rectangular 2ACSA can be improved. In the previously plotted cases with $\alpha = 1.3$ rad, the total length of the wire was $\sim 4.7$ meters. By changing the wrapping angle to $\alpha = 1.4$ rad and keeping all other parameters as in Table 2.1, the total length of used wire becomes $\sim 7.5$ meters. In the case of the wrapping angle $\alpha = 1.5$ rad, the length becomes $\sim 18$ meters. The beam patterns are shown in Fig. 2.8, and the antenna posessing a wrapping angle of 1.5 rad is plotted in Fig. 2.9.

I have also investigated the influence of adding more arms. In Fig. 2.10, a rectangular antenna with four arms is shown, along with its corresponding antenna beam pattern.

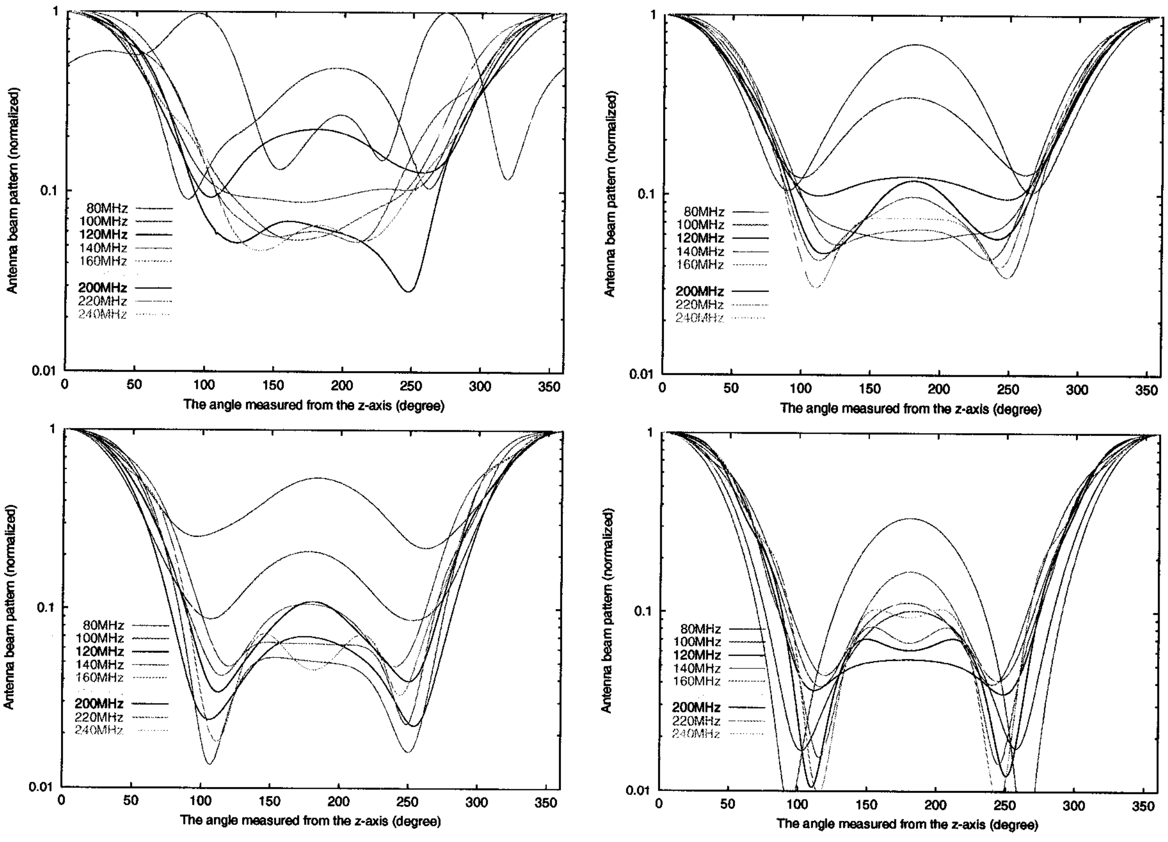

Figure 2.6: Antenna beam patterns for the 2ACSAs from Fig. 2.4 with the parameters as given in Table 2.1 and $\theta = 30°$.

Comparing to the equivalent two-arm case, we see that there is an additional breaking of symmetry.

The antenna side and back lobes can also be influenced by construction errors. If the building precision is ±1 cm, the resulting antenna and antenna beam patterns will look as shown in Fig. 2.11.

We ran the generic algorithm to test beam patterns for a set of antennas with different parameters in a given range. After comparing different antennas, we chose a rectangular approximation of the 2ACSA with a height of 3 m, $\alpha = 1.5$ rad, $\Delta\phi = 90°$. The antenna has a pyramidal structure defined by four rods fixed at the top and at the bottom. The rods have to be built from a hard dielectric material. A copper wire is used to form the two antenna arms wrapped around the four rods. The mechanical properties and final

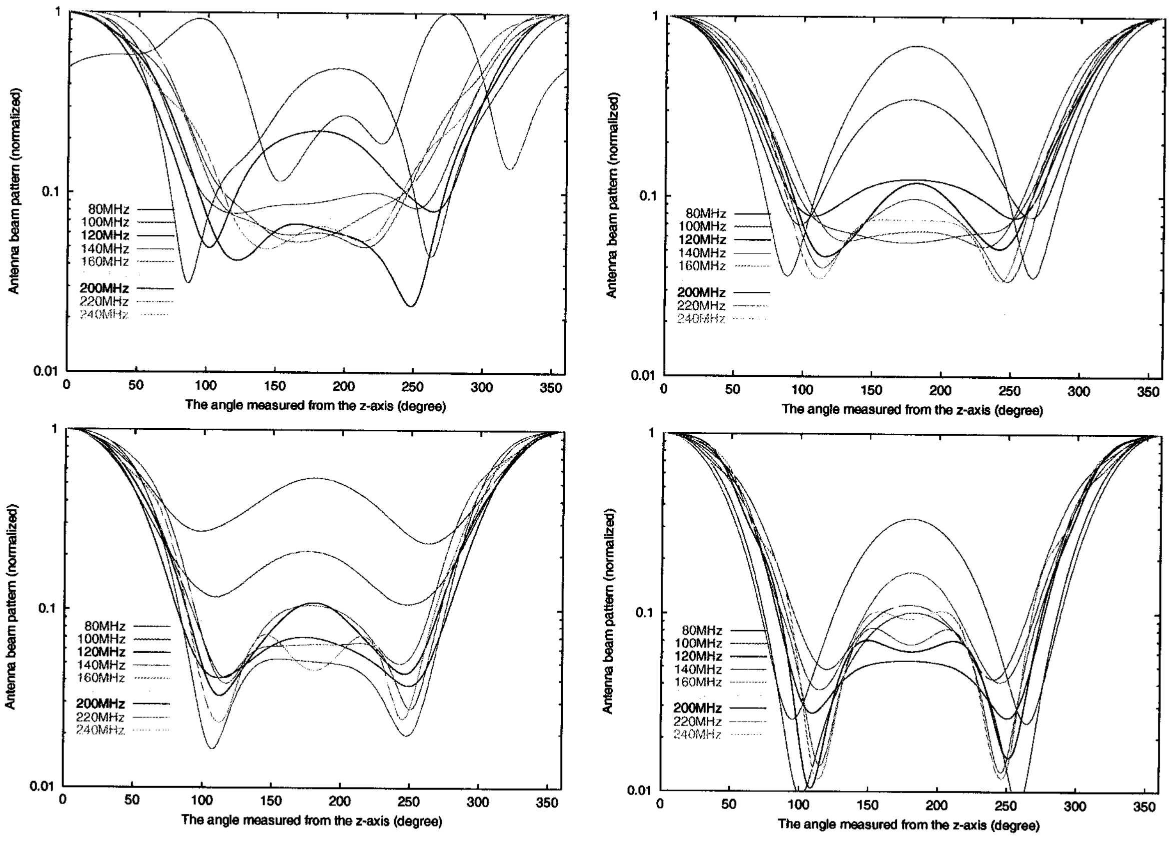

Figure 2.7: Antenna beam patterns for the 2ACSAs from Fig. 2.4 with the parameters as given in Table 2.1 and $\theta = 45°$.

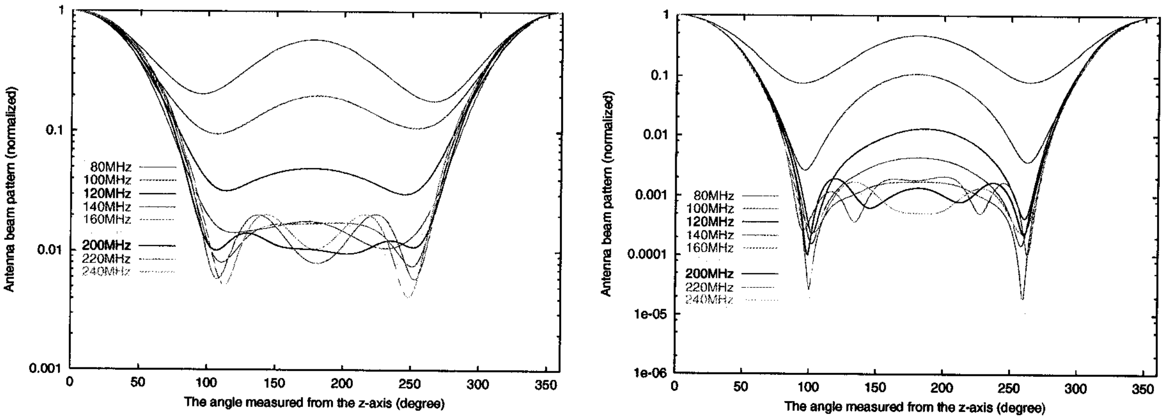

Figure 2.8: The antenna beam patterns for the 2ACSA from Fig. 2.4 with the parameters as given in Table 2.1. Both plots are done for $\phi = 90$ degrees. Left $\alpha = 1.4$ rad, right $\alpha = 1.5$ rad.

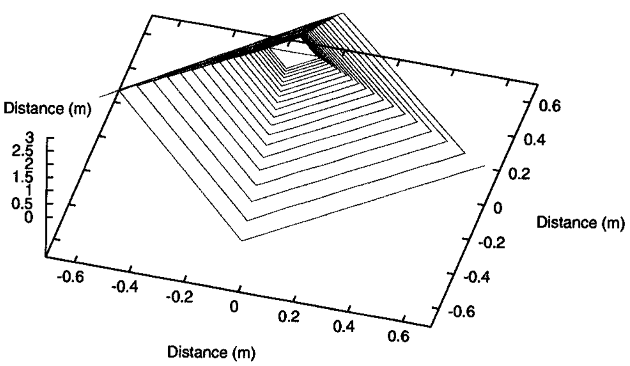

Figure 2.9: The antenna with paremeters as in Fig. 2.8 right.

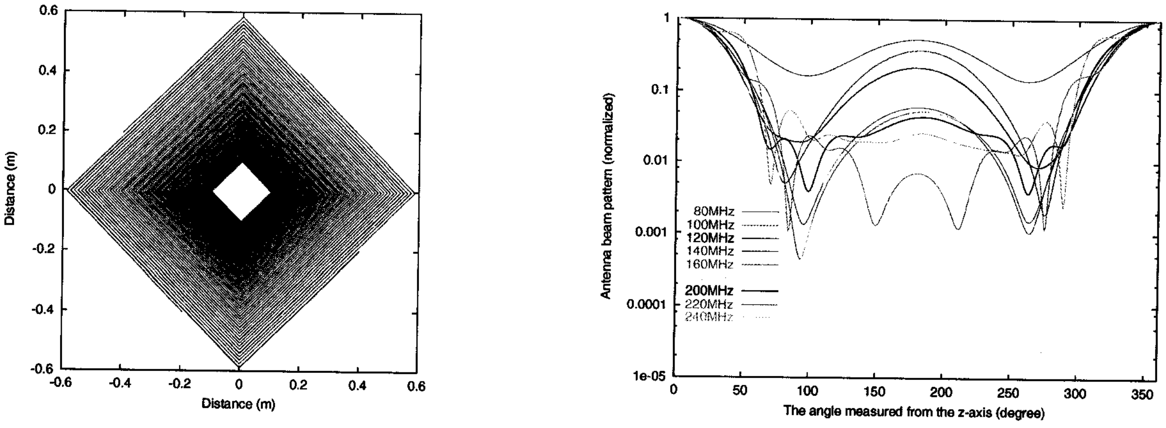

Figure 2.10: Left: top view of four arm CSA with the parameters as given in Table 2.1, $\alpha = 1.5$ rad and $\Delta\phi = \frac{2\pi}{4}$. Right: the normalized antenna beam patterns for the 4ACSA.

design are given below.

### Mechanical Properties of the Rectangular 2ACSA

The skeleton of the antenna should be built from a dielectric material with excellent mechanical properties. The antenna should have a light weight mounting, in order to be easily transported. The chosen material should have appropriate mechanical properties such that the structure does not get deformed with time due to the influence of atmo-

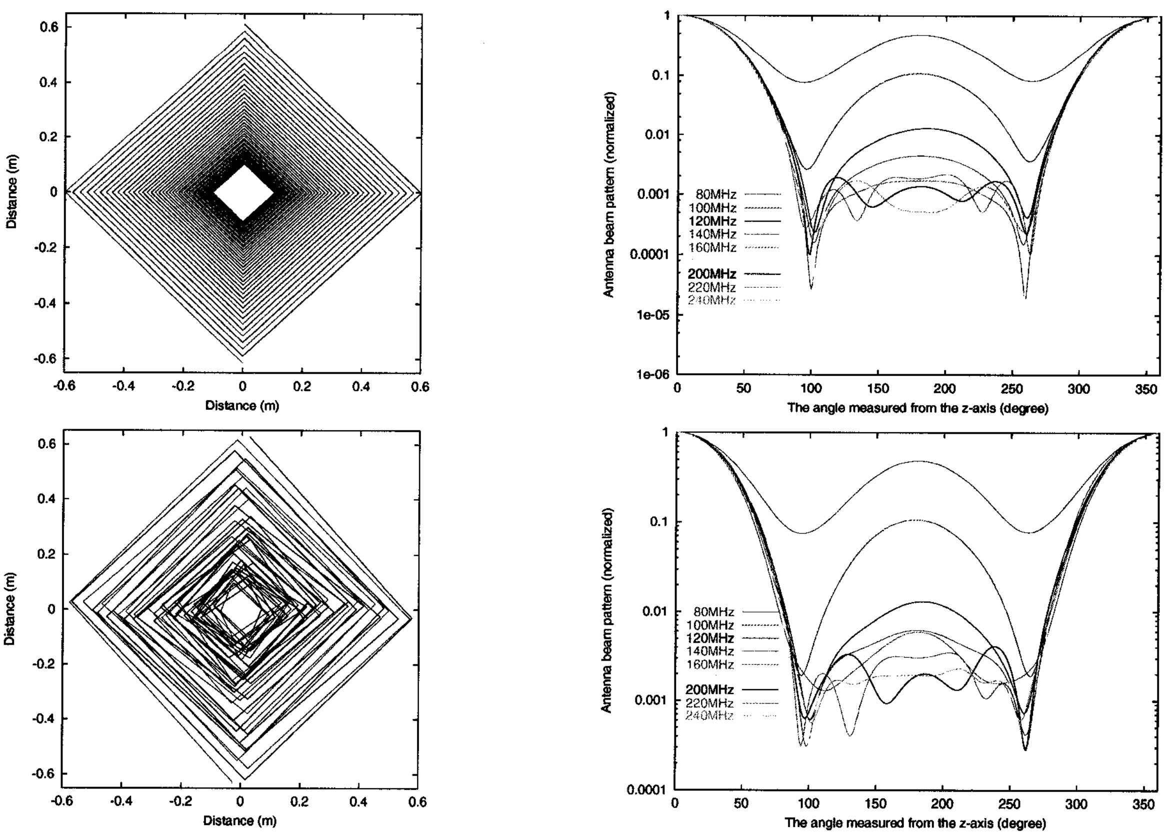

Figure 2.11: Top: 2ACSA and the normalized beam patterns. $\alpha = 1.5$ and the other parameters as in Table 2.1. Bottom: 2ACSA with the same parameters and ±1 cm construction tolerance.

spheric conditions. The wire tension also plays an important role in possible mechanical deformations. The structure needs to be stiff enough to minimize deformations. Lastly, as shown in subsection 1.2.2, antennas used for observing the 21 cm reionization line require a construction precision better than 1 mm. Fortunately, the precision achieved in the Department of Physics Machine Shop, University of Toronto, where our antenna was constructed, is high enough to satisfy this requirement.

The most important mechanical properties of any material are its resistance to bending, the ability to sustain a tensile load, and the expansion coefficients. Yield strength is a value found experimentally through testing indicating the amount of resistance to permanent deformation (bending). If a material is stressed below its yield strength, it will return to the original state after the stress stops. If a material is stressed beyond its yield strength, it will not return to the previous state when the stress is removed. The higher the yield strength, the more resistance to bending a material exhibits. Tensile strength defines when the tested material will fail under a tensile load (being pulled from each end of the material). Linear thermal expansion is a ratio of the change in the linear dimension to the original dimension for a unit change of temperature.

In engineering, stress is defined as force per unit area. If the stress stretches the material, it is called tensile stress, if it compresses the material, it is known as a compressive stress, and if it shears the material, we call it a shearing stress. The tensile and compressive stresses $\sigma$ are simply calculated from the force $F$ acting on the material with a cross-section $A$, such that $\sigma = \frac{F}{A}$. In the case of a circular cross-section, the tensile/compressive stress is

$$\sigma = \pm \frac{F}{r^2 \pi}.$$

The stress equation due to bending is given by

$$\sigma = \pm \frac{M}{Z} = \pm \frac{My}{I}, \tag{2.6}$$

where $M$ is the bending moment (force times distance), $Z$ is the section modulus (distance from the axis up to the distance of the object's furthest point), $y$ is the perpendicular distance from an axis through the center of gravity of the cross-sectional area to the stressed fiber and $I$ is the moment of inertia, which, for a full cylinder is $I = \frac{\pi d^4}{64}$.

The electrical properties of the material are defined by the dielectric constant or permittivity. It is a dimensionless constant that indicates how easily a material can become polarized. The constant is the ratio of the permittivity of the material in normal ambient conditions to the permittivity of a vacuum. Changes in temperature, moisture levels, electrical frequency and part thickness may affect the dielectric constant.

An excellent choice for the frame material for the antenna is fiberglass, also known as G10 or GFEC. The most common application of G10 is in the production of printed circuit boards. The main advantages of G10 are stiffness, strength, toughness (resistant against severe impacts), good density and excellent dielectric properties. On the other hand, G10 is UV-sensitive, expensive, and hard to cut, requiring power tools and special cutting-equipment. Dust produced while cutting G10 is very toxic and carcinogenic. The properties of G10 are summarized in Table 2.2.

| | |
|---|---|
| **Density** | 1790 kg/m$^3$ |
| **Specific Gravity** | 1.82 |
| **Coefficient of Thermal Expansion** | $0.9\times10^{-5}$ m/m/C° |
| **Tensile Strength** | 45 MPa |
| **Yield Strength** | 22 MPa |

Table 2.2: Properties of G10.

We can estimate the minimal diameter of the antenna side rods made of G10 as follows. Consider a rod of length $L$ and diameter $d$, supported at both ends. A force $F_x$ is applied to both ends in such a way that it tends to compress/stretch the rod. A force $F_y$ acts on the center of the rod, pushing it toward the ground (opposite from the support points). The maximal nominal tensile ($\sigma_a$) and compressive ($\sigma_b$) stresses are the combination of the bending and the tensile stresses given by

$$\sigma_a = -\frac{4}{d^2\pi}\left(\frac{2LF_y}{d} + F_x\right) \tag{2.7}$$

$$\sigma_b = \frac{4}{d^2\pi}\left(\frac{2LF_y}{d} - F_x\right) \tag{2.8}$$

Maximum nominal shear stress can be calculated from

$$\tau_a = \frac{1}{2}\sigma_a$$

$$\tau_b = \frac{1}{2}\sigma_b$$

For our purpose, the force $F_x$ can be ignored, so the nominal shearing stress is

$$\tau = \pm\frac{4}{\pi}\frac{LF_y}{d^3},$$

or by solving for $d$,

$$d = \left(\frac{4}{\pi}\frac{F_y L}{\tau}\right)^{1/3}.$$

Knowing that the yield strength of fiberglass is $\sim$ 20 MPa, and assuming that all pressure (in the form of $F_y$) applied to our rod of length $L = 3$ m is concentrated in the center, such that $F_y = 10^4$ N, one can calculate the minimal diameter to be $d \approx 8$ cm. The obtained diameter is overestimated, since the force $F_y$ is overestimated and not concentrated at a single point. By adding additional supporting rods, the shear stress can be further suppressed.

The compression due to antenna weight is negligible. Keeping in mind that the density of G10 is 1790 kg/m$^3$, and if each antenna side has a diameter of 8 cm and is 10 m long, the total mass is only

$$m = \rho \left(\frac{d}{2}\right)^2 \pi L \approx 90kg.$$

A 900 N weight causes pressure of $P = \frac{weight}{area} \approx 18$ kPa on the rod's cross-section, which is negligible compared to tensile strength of G10 (45 MPa). The same conclusion can also be obtained from equations (2.7) or (2.8). In the case of a real antenna, the mass of G10 is defined by the height of the antenna, plus the mass of thin wire. An additional complication is the fact that the rod is not vertical to the ground, but rather at some angle. However, even by including all "worst case" parameters, it can be concluded that tensile deformation will not play a critical role in the design. For a pipe with exterior and interior diameters, $d_2$ and $d_1$, respectively, the equations (2.7) and (2.8) become

$$\sigma = \pm\frac{F_x}{A} \mp \frac{My}{I} = \pm\frac{4}{\pi}\frac{F_x}{(d_2 - d_1)^2} \mp \frac{32}{\pi}\frac{F_y L d_2}{d_2^4 - d_1^4}.$$

Despite the significant change in tensile strength for the case of the pipe due to the fact that the cross-section of the pipe is smaller than in the case of the rod, this term can be neglected.

The simplest design would be 4 rods of appropriate lengths connected at the top of the structure (see Fig. 2.12). Each rod is composed of 3 smaller parts. Having multiple rods per antenna side would allow simpler machining (as an example, the limit on length of equipment available at the Machine Shop, Department of Physics, University of Toronto is only 1.5 m), as well as easy transportation once the antenna is disassembled.

A wire is wrapped around the antenna structure through holes in each rod. In Table 2.3 the distance from the base of the rod to the holes is given for the first arm. The wrapping starts from the top of the 1st rod. The second antenna arm is wrapped in the same way as the first arm but starting from rod 3.

| **Rod 1** (m) | **Rod 2** (m) | **Rod 3** (m) | **Rod 4** (m) |
|---|---|---|---|
| 2.785241 | 2.777342 | 2.769234 | 2.760913 |
| 2.752372 | 2.743607 | 2.734610 | 2.725377 |
| 2.715901 | 2.706175 | 2.696193 | 2.685948 |
| 2.675433 | 2.664641 | 2.653565 | 2.642198 |
| 2.630531 | 2.618556 | 2.606266 | 2.593653 |
| 2.580708 | 2.567421 | 2.553785 | 2.539789 |
| 2.525425 | 2.510682 | 2.495552 | 2.480022 |
| 2.464084 | 2.447726 | 2.430937 | 2.413706 |
| 2.396021 | 2.377871 | 2.359242 | 2.340123 |
| 2.320500 | 2.300361 | 2.279691 | 2.258476 |
| 2.236703 | 2.214357 | 2.191422 | 2.167882 |
| 2.143723 | 2.118928 | 2.093480 | 2.067361 |
| 2.040555 | 2.013042 | 1.984805 | 1.955824 |
| 1.926080 | 1.895553 | 1.864222 | 1.832065 |
| 1.799062 | 1.765189 | 1.730424 | 1.694744 |
| 1.658124 | 1.620539 | 1.581965 | 1.542375 |
| 1.501742 | 1.460038 | 1.417237 | 1.373308 |
| 1.328222 | 1.281949 | 1.234458 | 1.185715 |
| 1.135689 | 1.084345 | 1.031649 | 0.977565 |
| 0.922056 | 0.865086 | 0.806616 | 0.746605 |
| 0.685014 | 0.621801 | 0.556923 | 0.490336 |
| 0.421995 | 0.351855 | 0.279867 | 0.205984 |
| 0.130155 | 0.052328 | | |
| **Rod 3** (m) | **Rod 4** (m) | **Rod 1** (m) | **Rod 2** (m) |

Table 2.3: Antenna 1: The position of holes for the first antenna arm. The wrapping starts from rod 1. The second arm is symmetrically wrapped starting from rod 3.

The 21 cm Reionization EXperiment needs two identical but rescaled antennas. The second should be exactly 5% smaller than the first. Both antennas should be built from

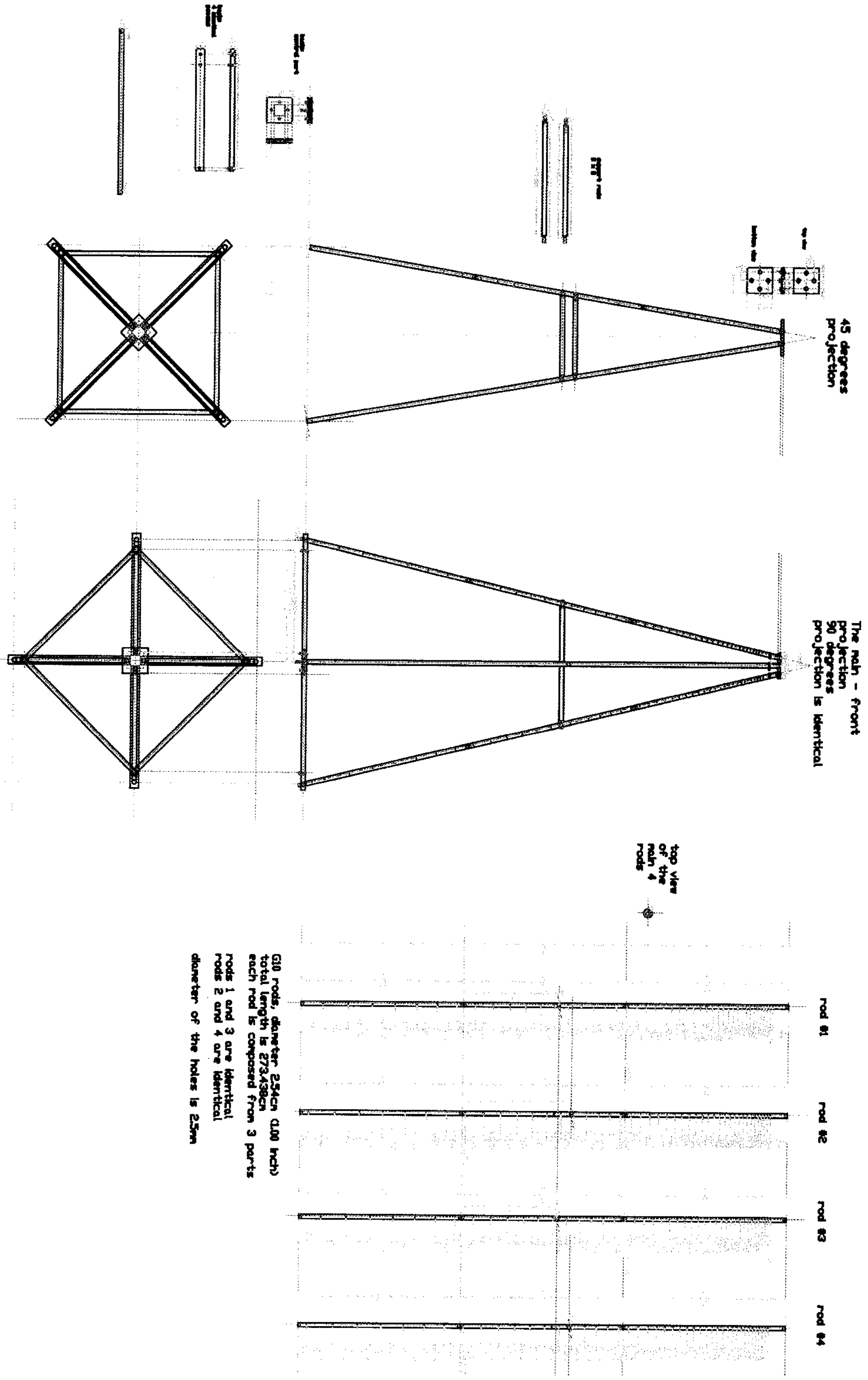

Figure 2.12: TREX schematics

the same material according to the schematics given in Fig. 2.12. The bigger antenna has a total wire length of 19.69 m, while the smaller should have 18.7 m. In reality, the length of wire depends heavily on how the the wrapping is performed.

The antenna (see Fig. 2.13) performed exceptionally well during the severe summer thunderstorm on July 17, 2006 in Algonquin Park. Despite strong winds of up to 130km/h the antenna was not damaged.

Figure 2.13: TREX antenna at the Algonquin Radio Observatory, July 2006.

## 2.2 From Antenna to Computer: Cables, Filters, Amplifiers and A/DC

Radio waves captured by the antenna are converted to electric current. The detected signal has to pass through a set of filters and amplifiers before reaching an A/D converter where conversion into digital form occurs. Finally, a spectrum is generated and the data are recorded.

In order to achieve the maximum power transfer and the minimum signal reflection at the destination, the source impedance must be equal to the load impedance. Two very common coaxial cables have an impedance of 50 Ω and 75 Ω. 50 Ω coaxial cables are commonly used with radio transmitters, radio receivers, laboratory equipment and for ethernet networks. 75 Ω coaxial cable is mostly used in video applications, CATV networks, TV antenna wiring and telecommunication applications.

For an ordinary coaxial cable used at a reasonable frequency, the characteristic impedance depends on the dimensions of the inner and outer conductors, and on the characteristics of the dielectric material between the inner and outer conductors. The length of the coaxial cable does not influence the line's impedance. In order for a cable's characteristic impedance to make a difference in the way the signal passes through it, the cable must be longer than the particular wavelength.

Mismatched transmission lines create a reflected wave of opposite polarity. Such a wave has a delay time defined by the length of the line and the speed of the wave propagation (the usual speed of propagation inside a coax line is about $\frac{2}{3}c$.) The reflected wave distorts the outbound waves and can be reflected again and again. Multiple reflections create confusion and interference with the true signal.

An impedance matching system is required if there is a need to connect two cables with different impedances. A well designed matching system can successfully prevent signal reflections at the cable connection point. The simplest matching system is a transformer with the proper impedance transfer ratio defined by

$$\frac{Z_A}{N_A^2} = \frac{Z_B}{N_B^2}, \tag{2.9}$$

where $Z_A$ and $Z_B$ are the input and the output impedance, respectively. $N_A$ and $N_B$ are the number of turns on the input and the output coil, respectively.

An analog/digital converter maps a continuous signal into a stream of $n$-bit samples. By increasing the sampling rate, one can capture faster fluctuations of the signal. The

$n$-bit quantization carries an error which can be reduced by choosing an appropriate $n$. The whole process of obtaining a sampled signal $x_{sampled}(t)$ every $T_s$ seconds can be described as

$$x_{sampled}(t) = x(t)p(t) = x(t) \sum_{m=-\infty}^{\infty} \delta(t - mT_s), \tag{2.10}$$

where $x(t)$ represents a continuous-time signal at time $t$ and $m$ is the integer representing the number of samples. $p(t)$ is known as a periodic impulse train function, or the sampling function. A frequency spectrum $X_{sampled}$ of the sampled data set is obtained after taking the Fourier transform

$$X_{sampled}(f) = FT[x(t)p(t)] = X(f) * P(f) = X(f) * \sum_{k=-\infty}^{\infty} \delta(f - kf_s).$$

The operator $FT[]$ denotes the Fourier transform, $k$ is an integer, $f$ stands for frequency and the sampling frequency is $f_s = \frac{1}{T_s}$. The Fourier transform of multiplication of two time domain functions is equal to the convolution of their frequency spectra. The convolution of a signal spectrum $X(f)$ with each $\delta(f - kf_s)$, shifts $X(f)$ and centers it on $kf_s$. The resulting spectrum $X_{sampled}(f)$ is a periodic repetition of the original signal spectrum $X(f)$ centered on $0$, $\pm f_s$, $\pm 2f_s$, ...

Using the above consideration, the so-called sampling theorem can be derived: the sampling frequency has to be at least two times higher than the frequency of the wanted signal. If the sampling frequency is not high enough, the adjacent parts of the spectrum overlap, and it is not possible to remove the overlapping. Such a distortion of the obtained spectrum is called aliasing. The minimum sampling rate $f_s = 2f_{max}$ is called the Nyquist rate. One half of the Nyquist rate $\frac{f_s}{2}$ is the Nyquist frequency.

The second important condition included in the sampling theorem is that the signal must be band limited over some frequency interval $f_{min} \leq f \leq f_{max}$. Low pass or anti-aliasing filtering should be applied before sampling. To make sure that the output of the anti-aliasing prefilter is band limited to the maximal frequency $f_{max}$, the cutoff frequency of an anti-aliasing prefilter must be, at most, equal to the Nyquist frequency ($f_{max} \leq \frac{f_s}{2}$).

The digitized data are transferred to computer memory via a Peripheral Component Interconnect (PCI) bus. It is a vendor and platform independent bus created to have high performance for modern (at least 32 bit, $\sim 1$ GHz CPU) computer systems, for the first time seen in 1995, with the first Intel Pentium CPU chip sets. Technically speaking, PCI is a 5 V, 33 MHz, 32-bit bus with a basic data transfer rate of 133 MB/s (megabytes). However, the basic design can be modified to include a 64-bit bus extension (basic data transfer rate of 256 MB/s), 66 MHz extension (doubles the basic data transfer rate), 3.3 V operation (different physical connector), and a small PCI connector for laptops and other space-limited embedded systems. Most of the modern design optimizations are included in PCI design: multiprocessor support, multiple bus mastering support, burst transfers, interrupt sparing, write posting and processor bridging. Each PCI Slot consists of a multiplexed address and data bus, four interrupt lines, +5 V, +3.3 V +12 V and -12 V power supply lines, card presence sensing, test and control lines.

With an 8 bit 500 MHz AD converter, the total amount of data generated in one second is 500 MB, which is about four times more than a standard PCI bus can transfer. Such a system can work with, at most, 25% efficiency. In reality, due to various factors such as the time needed for collecting data and generating the spectrum, the true efficiency is about 5%.

The data transfer between the AD converter and the computer processor can be sped up by using a faster bus such as PCI-X, or PCI-express. The standard PCI is 32-bit wide working at 33 MHz with a peak theoretical bandwidth of 133 MB/s, while PCI-X is 64-bit wide, working at 33/66/133 MHz and capable of transferring up to 1 GB/s, and the latest PCI-express bus is able to transfer 5 GB/s. Despite the availability of the buses capable of sustaining the needed transfer rates, at the time of writing there are still no commercially available A/D cards with the power to stream all the data to the processor. A faster data acquisition system is currently being built at the Physics Electronics Resource Centre at the University of Toronto. A 64-bit PCI-X bus can be used to transfer the data to computer memory in real time.

## 2.3 Spectrum Reconstruction

After the data are received in the main memory, the power spectrum has to be calculated by performing a Fourier transform. The discrete Fourier transform of a periodic vector function $\mathbf{x}(nT)$ is

$$\mathbf{X}(f) = \sum_{n=-\infty}^{\infty} \mathbf{x}(nT) e^{-2\pi j f n T}. \tag{2.11}$$

One of the simplest FFT algorithms, a Cooley-Turkey method will be described below. Adapting equation (2.11), an $N$-point discrete Fourier transform $X(k)$ of the $N$-elements sequence $x(n)$, $n$ =0, 1, .., $N-1$ can be written as

$$X(k) = \sum_{n=0}^{N-1} W_N^{kn} x(n), \quad k = 0,\ 1, ..\ N-1,$$

where the matrix elements $W_N^{kn}$ are defined as

$$W_N^{kn} = e^{-2\pi j kn/N} = e^{-j\omega_k n}.$$

The above equation can be rewritten in such a way that the even and the odd terms are grouped separately

$$X(k) = \sum_{n=0}^{N/2-1} W_N^{k(2n)} x(2n) + \sum_{n=0}^{N/2-1} W_N^{k(2n+1)} x(2n+1). \tag{2.12}$$

By defining two subsequences of length $N/2$:

$$g(n) = x(2n),$$

$$\text{and} \quad h(n) = x(2n+1), \quad n = 0,\ 1, ..\ \frac{N}{2} - 1$$

with their respective $N/2$-point FTs

$$G(k) = \sum_{n=0}^{\frac{N}{2}-1} W_{\frac{N}{2}}^{kn} g(n), \tag{2.13}$$

$$\text{and} \ H(k) = \sum_{n=0}^{\frac{N}{2}-1} W_{\frac{N}{2}}^{kn} h(n). \tag{2.14}$$

The most important property of factor $W_{\frac{N}{2}}$ is

$$W_{\frac{N}{2}} = e^{-2\pi j/\frac{n}{2}} = e^{-4\pi j/N} = W_N^2,$$

which finally gives us

$$\begin{aligned} W_N^{k(2n)} &= \left(W_N^2\right)^{kn} = W_{\frac{N}{2}}^{kn} \\ W_N^{k(2n+1)} &= W_N^k W_{\frac{N}{2}}^{kn}. \end{aligned}$$

Equation (2.12) can now be written as

$$X(k) = \sum_{n=0}^{\frac{N}{2}-1} W_{N/2}^{kn} g(n) + W_N^k \sum_{n=0}^{\frac{N}{2}-1} W_{N/2}^{kn} h(n),$$

or in a simpler form using (2.13) and (2.14):

$$X(k) = G(k) + W_N^k H(k). \tag{2.15}$$

Hence, $X(k)$ can be constructed from the two $\frac{N}{2}$-point FTs $G(k)$ and $H(k)$.

The total number of operations needed for performing an $N$-point FT is $N^2$. After splitting the initial number of points into the two subsets of the same length (see eq. 2.15), the number of operations consists of all multiplications needed to perform two $\frac{N}{2}$-point FTs and $\frac{N}{2}$-multiplications with factors $W_N^k$. If $N$ is sufficiently large, the number of multiplications is

$$2\left(\frac{N}{2}\right)^2 + \frac{N}{2} = \frac{N^2}{2} + \frac{N}{2} \approx \frac{N^2}{2}.$$

By continuing to split into smaller and smaller subsets, the total computing cost will be $\frac{N^2}{2^m} + \frac{N}{2}m$. Only the second term is important because $\frac{N^2}{2^m} \longrightarrow 0$, for large $m$. In the final limit, the total cost of an $N$-point FFT is $\frac{1}{2}N\log_2 N$.

The frequency resolution of the obtained spectrum must be high enough so that the individual sources can be recognized. As a reference, the different FM stations must be at least 200kHz apart.

Since Intel's SIMD2 technology permits parallelization of mathematical operations, FFT code can be additionally sped up by parallelizing more FFTs. An initial $N$-point sequence $x(n)$ can be split into $l$ subsequences. The size of the computer registers defines $l$, which should be a power of 2, such that we can fit the data with the same index in each subset into the same register. In the end, the result can be converted to one unique FFT by using (2.15).

### 2.3.1 An Even Faster FFT Code

I have developed an FFT code for 16 bit integers, which at the time of writing performed faster than any other known algorithm. The code uses the ability of Intel's processor to perform multiple mathematical operations at the cost of a single instruction. In this subsection it will be explained how such an algorithm works, and what the calculation constraints are.

Intel's new microprocessors such as Pentium 4 and Itanium have implemented a set of instructions for calculations with multiple data in a single instruction - SIMD processing [48]. Primarily designed for speeding up multimedia applications, these instructions can be used for speeding up almost any programming task. The implementation is done through the extensions to previously defined instructions. From a programmer's point of view, the benefits of SIMD can be implemented using the inlined assembly code, or more simply, by using Intel's C++ API extension sets, better known as intrinsics. Intrinsics are the special coding extensions that allow for the use of C function call syntax and C variables instead of hardware registers. Use of the intrinsics frees programmers from having to program in assembly language and manage the registers manually. Compiler optimization is automated so that the instructions are scheduled to maximize the running speed.

SIMD extensions use eight 128-bit registers capable of processing the data elements in parallel. Since each of the registers can store more than one data element, the processor can operate with multiple data elements simultaneously. The algorithm written uses SIMD2 extensively with 16-bit data elements (short integers). Each 128-bit SIMD register

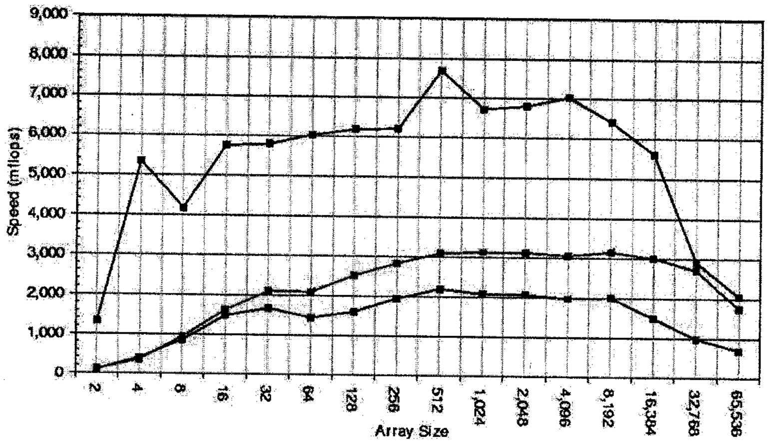

Figure 2.14: Speed comparison of SIMD2 optimized FFT code (top) with the FFTW algorithm working with 32-bit floating point data (middle) and 64-bit double floating point data (bottom). The tests were performed on a 2.4 GHz Intel Xeon machine by Ana Lubuchenko.

can hold and simultaneously operate with eight 16-bit integer values. Thus, we are computing eight FFTs simultaneously by packing eight 16-bit data elements into one 128-bit SIMD type. This means that our algorithm performs eight FFTs at the cost of one. We have tested the FFT performance of this new algorithm and compared the results with the FFTW code working with 64-bit data and 32-bit data. The results are presented in figure 2.14.

Our algorithm shows a faster execution time by roughly a factor of two. The drop in speed at the array size of $2^{14}$ is due to the processor cache memory. FFTW is also affected by cache limitations, but with larger array sizes. We are initially using eight 16-bit data arrays compared to only one 32- or 64-bit data array. One might expect a greater difference in the execution speed, knowing that 8 FFTs are being executed at the cost of one in the SIMD2 code. However, FFTW also uses SIMD technology to reduce the execution time by parallelizing groups of instructions if possible. For example, if there are two consecutive additions they are done in parallel. Such an optimization is limited by compiler/programmer ability to transfer the linear code into parallel. A good example of the instructions which cannot be done in parallel is

$$x = 3 + 5;$$

$$y = x + 3,$$

because the input of the second equation depends on the result of the first one.

There are two limitations to our code. The first one is data overflow caused by the 2-byte data size limitation. If the result of any operation is longer than 2 bytes, overflow will be generated. There is no cure for this, since overflow testing would slow down the algorithm by a factor of $\sim 10$. The second one is due to arithmetic data shifting. Since division in the set of short numbers is not hardware defined, one has to use data shifting to perform this operation. To divide a binary number by 2, it is enough to arithmetically shift the binary number one place to the right. The shifting also carries the sign, so that for example, $1/2 \Rightarrow 0$, but $-1/2 \Rightarrow -1$, which causes an error in the FFT result. However, despite the loss in the resulting precision, this algorithm can still be used to detect individual spectral lines as indicated below.

The two 16-bit sets in Fig. 2.15 show a "ghost" line at 155.9 MHz. The origin of this "ghost" line is data overflow. At frequencies of about 70-80 MHz in the bottom spectrum there are also ghost lines originating from the division error discussed above. Despite these two types of errors, the spectra calculated using our algorithm can still be used for scientific data analysis. These errors are "constant" in time if the spectra do not change. In the case of spectral lines caused by meteor forward-scattering, the error is negligible.

## 2.4 Data Format

The observed data are saved using the Flexible Image Transport System (FITS) file format [47]. Each file has a size of about 10 MB. The header of the FITS file is in ASCII format and stores information about the place of the observations, instrument specification, universal time and information describing the binary part of the file. The

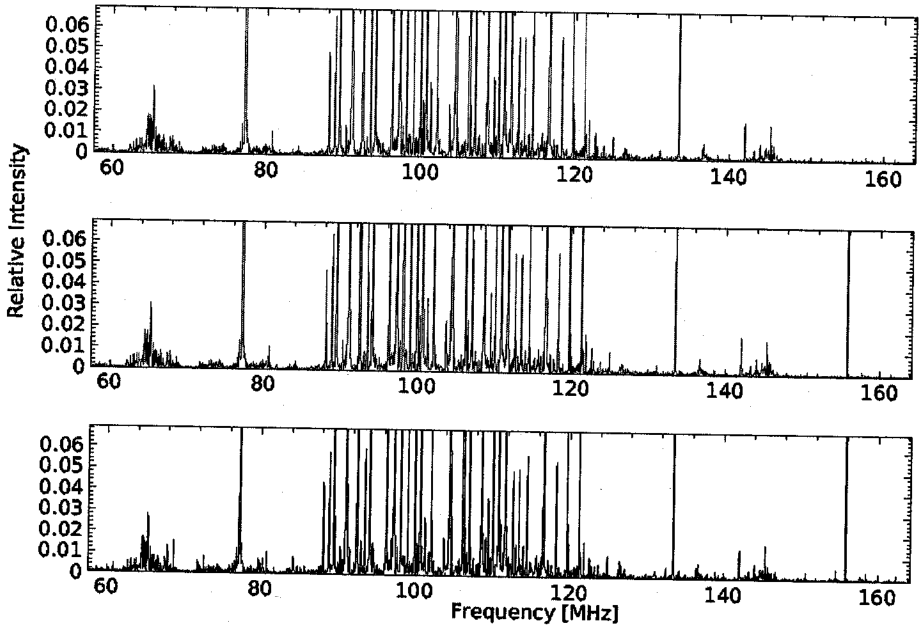

Figure 2.15: Comparison of spectra calculated from the same dataset using different data types: 32-bit floating point (top), 16-bit integer (middle) and 16-bit integer using SIMD2 instructions (bottom). For the two bottom spectra, the FFT is done with 16-bit precision and the final power spectra are calculated as 32-bit integers. Data was obtained using a rectangular approximation of the two arm conical spiral antenna at the Department of Physics, University of Toronto on July 28th, 2004.

main part of the fits file is an $N_x \times N_y$ matrix where each row carries the time information (first 8 bytes) and the spectrum remaining ($N_x - 8$ bytes).

# Chapter 3

# Meteor Forward Scattering

## 3.1 Basics of Meteor Observations

A meteoroid entering the atmosphere forms an ionized column of air capable of reflecting radio waves. At altitudes of 70-140 km, the meteoroid collides with air molecules and the impact energy is transformed into heat, evaporating atoms from the meteoroid. These free atoms also collide with air molecules, producing an optical phenomenon called a meteor, and ionizing the surrounding media. Thus, an ionized region around the path of the meteoroid is formed.

Depending on the relative amount of free electrons in a meteor trail, there are two distinct regimes defining the properties of electromagnetic wave propagation. In an underdense trail, the density of free electrons is smaller than the critical density, making the trail transparent to incident radiation. In the overdense regime, the core of the trail behaves as a metallic cylinder, and incident radiation is scattered off.

In this work we focus on radio observations of meteors. For an overview of other observational techniques, the reader can see the standard meteor textbooks [59] and [74]. In this section, the forward-scattering observation method will be discussed in detail. We first summarize the basic physical properties of meteoroids and the ionosphere. In addition, the ablation of meteoroids as well as the creation and the disappearance of ionized trails are explained. An elegant proof that an ionized trail is in the plasma state leads toward a simple division into underdense and overdense trails. The principles of the forward scattering method for observing meteoroids will be explained. A typical forward scattering system, composed of a transmitter, an ionized trail with a scattering point, and a receiver, has a complex geometry. In the case of coherent scattering, the transmitter and receiver must be at the focal points of an ellipsoid. The line describing the path of the meteoroid is a tangent to the surface of the ellipsoid. A polished mathematical solution using this ellipsoid to geometrically establish the elements of the forward scattering is used to define meteor footprints. Finally, a method to estimate the kinetic parameters of a meteoroid using forward scattering at multiple frequencies is presented.

### 3.1.1 Properties of Meteoroids

Average meteoroids are usually composed of iron, carbon or silicate rocks. Traces of the alkali metals sodium and potassium, as well as of the alkaline earth metals magnesium and calcium, were observed in the spectra of fireballs [6] and smaller meteoroids using airplane or rocket-borne ion mass spectrometers [35], [118]. Since these metals are easily ionized due to a low ionization energy of $\sim 5$ eV they might be the primary source of free electrons. Alkali metals have one electron in the outer shell that is easily given off. Compared to the ionization energy of iron, which is 7.87 eV, the energy needed to ionize potassium is roughly two times smaller (4.34 eV). Even a relatively small percentage of alkaline and alkaline earth metals can create a huge amount of free electrons compared to the contribution of other elements. It is interesting to mention that potassium is rarely detected in spectrographic observations of the visual part of the spectrum because the most intense potassium line, at 766.49 nm, is in the infrared. The mass density of meteoroids depends on their composition and is of the order $10^3$ kg/m$^3$.

The size of detected meteoroids spans more than 9 orders of magnitude, from small dust particles with a diameter of less then a micrometer ($10^{-6}$ m), to over 10 kilometers ($10^4$ m). Depending on composition and size, masses of meteoroids vary from $10^{-16}$ kg to $10^6$ kg. If a meteoric particle is very small ($\lesssim 10^{-6}$ m), atmospheric drag might slow it down quickly enough to prevent ablation. Particles with masses as low as $10^{-16}$ kg have been detected by space probes [38]. Radar observations detected particles with sizes of $\sim 10^{-6}$ m and masses from $10^{-10}$ kg and up [51]. Meteors observed visually, with a TV camera or with a telescope, usually have diameters larger than $10^{-4}$ m. Meteoroids of centimeter size cause fireballs - spectacular meteors, with apparent magnitudes of less than $-4$, which makes them brighter than Venus. The impact of an asteroid approximately $10^4$ m in size most likely caused the extinction of the dinosaurs 65 million years ago. The impact place is marked by a 180 km crater near Progresso in the Yucatan Peninsula, Mexico. The crater is called Chicxulub, which in Mayan roughly translates as "tail of the devil". It is believed that such impacts happen about once every 100 million years.

| | | | |
|---|---|---|---|
| diameter | $d$ | $10^{-6} - 10^4$ | m |
| mass | $m$ | $10^{-10} - 10^6$ | kg |
| orbital velocity | $v_g$ | $(1-8) \times 10^4$ | m/s |
| number density of free electrons | $n_e$ | $10^{11} - 10^{20}$ | $\mathrm{m}^{-3}$ |
| number density of air particles | $n_n$ | $10^{17} - 10^{22}$ | $\mathrm{m}^{-3}$ |
| linear density of free electrons | $\alpha$ | $10^{11} - 10^{20}$ | $\mathrm{m}^{-1}$ |
| initial radius of trail | $r_0$ | $10^{-1} - 10$ | m |
| length of trail | $l_t$ | $(1-4) \times 10^4$ | m |
| ablation temperature | $T$ | $2000 - 4000$ | K |
| ablation heights | $h$ | $(7-14) \times 10^4$ | m |
| ambipolar diffusion coefficient | $D_\alpha$ | $0.1 - 1000$ | $\mathrm{m}^2/\mathrm{s}$ |
| atmospheric temperature at ablation heights | $T_a$ | $200 - 500$ | K |
| Langmuir frequency | $\omega_p$ | $10^6 - 10^{12}$ | Hz |

Table 3.1: The parameters used for describing meteoroids and meteor trails with the typical range important for radio observations.

The atmosphere of the Earth is bombarded daily by hundreds of millions of meteoroids. The smaller the masses and sizes of meteoroids entering the atmosphere, the higher their abundance. Larger bodies hit the atmosphere less frequently. Over a thousand fireballs occur in the Earth's atmosphere every day. The geocentric velocities of meteoroids are of the order of the Earth's orbital velocity around the Sun $\sim 3 \times 10^4$ m/s, typically from 10 km/s to 70 km/s. Three different methods for the total mass flux of meteoroids entering the Earth's atmosphere have been reviewed in [147]. The estimates of the total daily mass flux are up to $10^7$ kg, as estimated by Allen and van de Hulst in the late 1940's [74]. This number is confirmed using different techniques [13], [146].

Meteoroids entering the Earth's atmosphere lose their initial velocity due to impacts with atmospheric particles. When the meteoroid diameter is around one meter, the meteoroid does not have enough time to lose all its mass. During the fireball stage, atmospheric friction slows down the meteoroid to a speed of about 3 km/s. In the final stage of the flight, the velocity is low and the meteor fades into the so-called "dark flight" stage. If the meteoroid reaches the surface of the Earth, it is called a meteorite. Depending on its size, a meteorite can create a crater.

A portion of detected meteoroids originate from outside the Solar system. Studies of orbits detected by space dust detectors on Ulysses and Galileo estimated the mass distribution of interstellar dust grains in the solar system. The flux of extrasolar meteoroids with masses larger than $10^{-14}$ kg is estimated at $10^{-6}$ $\mathrm{m}^{-2}\mathrm{s}^{-1}$ [64]. Ground radar observations have also reported meteoroids of extrasolar origin [77], [3].

### 3.1.2 Meteor Showers and Sporadics

The hourly rate of meteors at certain periods of the year increases dramatically. These time periods, known as meteor showers, occur when the Earth passes through a higher concentration of space particles. If the particles/meteoroids are orbiting the Sun following similar orbits they are called streams of meteoroids.

Looking from the surface of the Earth, it seems as if all members of a particular stream enter the atmosphere from the same point on the celestial sphere called a radiant.

All members of a stream follow parallel paths, and to an observer it looks as if the lines meet at a single point since parallel lines appear to meet at infinity. Since the radiant has an almost fixed position on the sky, it is common practice to name showers after the constellation the radiant is positioned in. The most famous meteor showers are the Perseids active in early August, the April Lyrids and the Leonids in November. As the Earth revolves around the Sun, the radiant drifts slowly over the sky. Most of the orbits in planetary systems do not change their orbital plane, so the Earth encounters the same meteoroid stream every year over the same time period.

Comparison of meteoroid orbits showed that most of the streams are following the orbits of certain comets. The current theory is that comets leave debris behind, which in time spreads over the cometary orbit. For example, the Perseid meteor stream is related to comet 1862 III, while the Leonids originated from comet Tempel-Tuttle. Halley's comet is the mother of the Orionid shower, active in October.

Meteoroids with random orbits are called sporadics. The general opinion is that sporadics are either of the same origin as stream members but are gravitationally perturbed, or that they have a collisional origin.

Statistically, there are daily and seasonal variations in the number of detected sporadics. The distribution of the sporadics is not uniform over the sky as initially assumed. There are four apparent directions where sporadics are most likely to be detected: the Sun, anti-sun, apex and toroidal direction. The activity and the structure over a period of 10 years of the first two sporadic regions is given in [108], and the activity of all four regions over a period of 3 years in [10].

### 3.1.3 Ablation and Deceleration

Dimensions of typical radio meteoroids are much smaller than the mean free path of air particles and there is no hydrodynamic flow around the meteoroid. The mean free path of the air particles at these heights is about 0.1 m, with kinetic energies of about 8 eV per nucleon.

Collisions with air particles produce impact energy which is transformed into heat and eventually makes the meteoroid's atoms evaporate. At a height of $\sim 100$ km above ground, the meteoroid's surface reaches a temperature of about 2000 K. The atoms from the surface of the meteoroid start to evaporate. This stage of a meteor's life, when the melting surface gradually disappears due to evaporation, is known as the ablation phase.

The free atoms evaporated from the meteoroid quickly collide with air particles creating a meteor. The impact energy is converted into heat and ionization energy. In addition to the meteor phenomenon, an ionized trail is formed. Both the meteor and the ionized trail are cylindrically symmetrical due to their formation along the path of the meteoroid.

Small meteoric particles, with diameters $\lesssim 10^{-6}$ m have thermal energy emission of the order of the energy gained through collisions with air. Such particles might slow down fast enough before ablation can occur and stay unchanged in the atmosphere, or eventually reach the ground. Realistic atmospheric models have been used in the past to numerically solve the differential equations of meteor ablation. Simulations confirmed that the ablation strongly depends on the initial geocentric velocity of the meteoroid [93].

During flight time $dt$, a meteoric body with velocity $v$ collides with air particles with total mass $dm_a$ equal to

$$dm_a = A_M \rho_a v dt,$$

where $A_M$ is the effective cross-section of the meteoroid and $\rho_a$ is the density of the air at a given height. Only a portion of the kinetic energy (equal to $1/2 dm_a v^2$) of the air flow is transformed into heat. The measure of the energy transfer is the heat-transfer coefficient $\Lambda$, which always has to be less than 1. Usually it is considered to be between 10% and 60% [74]. After the meteoroid reaches the melting temperature, it starts to lose mass by evaporation. The mass loss rate is

$$\frac{dm}{dt} = -\Lambda \frac{1}{2Q} A_M \rho_a v^3. \tag{3.1}$$

The latent heat of vaporization $Q$ includes the energy needed to heat the body up to its melting point, as well as the energy needed for evaporation. In the physical models of ablation, the latent heat used is $Q \sim 10^6$ Jkg$^{-1}$ [93].

The deceleration of the meteoric body is described by the momentum equation

$$m\frac{d\mathbf{v}}{dt} = m\mathbf{g}_h - \Gamma A_M \rho_a v^2,$$

where $m$ and $\mathbf{v}$ are the mass and the velocity vector of the meteoroid, respectively, $\mathbf{g}_h$ is the gravitational acceleration at the given height and $\Gamma$ is the drag constant which takes values between 0.5 and 1. In meteor literature, the shape factor $A$ is defined from the mid-sectional area of the meteoroid $A_M$ as

$$A = A_M \left(\frac{m}{\rho}\right)^{2/3}, \tag{3.2}$$

where $\rho$ is the density of the meteoroid. In the case of a cubically shaped object, the shape factor is $A = 1$, while for a spherical object $A = 1.21$.

### 3.1.4 Creation of Ionized Trails

The creation of the ionized trail can be described by the ionization equation defining the number of electrons formed due to ablation of the meteoroid as

$$\alpha = -\frac{\beta}{m_m v}\frac{dm}{dt}. \tag{3.3}$$

The electron line density $\alpha$ is the number of electrons per unit length of the ionized trail. It is considered to be one of the most important features of the trail. $m_m$ is the average mass of meteoric atoms or molecules, $v$ is the meteoroid's velocity, and $\beta$ is the number of free electrons in a single vaporized meteoroid atom, also known as the ionization coefficient. $\beta$ depends exponentially on the meteoroid's velocity. $\frac{dm}{dt}$ is the amount of the meteoroid's mass evaporated per time interval. Physically, this equation shows the number of free electrons produced along the path of the meteoroid due to rapid mass loss. Using (3.1), a more common form of the ionization equation is

$$\alpha = \frac{\Lambda\beta}{2Qm_m} A_M \rho_a v^2. \tag{3.4}$$

Taking the time derivative of the ionization equation, the maximal line density along the trail can be estimated to be [83]

$$\alpha_{max} = \frac{3}{4}\frac{\beta m}{m_m H},$$

where $H$ is the distance over which the atmospheric pressure decreases by a factor of $e$, also known as the scale height. It can be expressed using Boltzman's constant $k$, temperature $T$, average mass of the air molecules $m_a$ and gravitational acceleration $g$ as:

$$H = \frac{kT}{m_a g}.$$

An ionized column reflects radio waves as dictated by the laws of optics. The incident angle of a radio wave must be equal to the reflected angle. A direct implication of the specular reflection is that only a limited part of the reflecting surface, in our case the meteor line/cylinder, is responsible for the reflection of the given radio wave. One can draw an analogy with observing a light bulb in a mirror: the bulb can be seen in only one particular area of the mirror. For the trail to be observable, there must be significant ionization in the reflection region.

The maximal intensity of the reflected signal is obtained in the case of coherent scattering: the transmitter, the trail and the receiver are aligned in such a way that the transmitter and the receiver are the foci of an ellipsoid, while the meteor trail is the tangent to this ellipsoid. In most cases the trail can be approximated as a straight line of typical length $10-40$ km [28], but for meteors with a long duration ($\sim 10$ s) the trail becomes deformed due to the influence of winds.

As the trail is formed, parts of the trail with positive and negative interference create constructive and destructive Fresnel zones, respectively. Reflected signals scattered off different parts of the trail travel different distances, resulting in a phase difference. As the trail expands, the destructive interference from the front and back leads to an exponential decay of the reflected signal. A typical first Fresnel zone has a length on the order of a kilometer, while the whole trail can be up to 40 km long.

The number density of free electrons $n_e$, for most of the radar observed meteors takes values from $10^{11}$ m$^{-3}$ to $10^{20}$ m$^{-3}$ [132]. To relate the number density $n_e$ with the linear density $\alpha$ of free electrons, an initial radius $r_0$ of the trail's cross-section has to be known. Equation (3.11) can be used to estimate this. The linear density $\alpha$ is defined inside the ionized trail, thus

$$n_e = \frac{\alpha}{\pi r_0^2}. \tag{3.5}$$

### 3.1.5 Atmospheric Models

In the simplest atmospheric models, the density of the atmosphere depends only on the height $h$. Let us assume that the atmosphere is described by an ideal gas

$$p = \frac{\rho_a}{m_a} kT, \tag{3.6}$$

where $p$ is the pressure, $\frac{\rho_a}{m_a} = n = \frac{N}{V}$ is the concentration or number density of $N$ air particles inside a volume $V$ with the density $\rho_a$ and particle mass $m_a$, $T$ is the temperature of the atmospheric gas, and $k$ is Boltzman constant. The change in the hydrostatic pressure with height can be written according to Pascal's law

$$dp = \rho_a g dh.$$

Substituting $\rho_a$ from the last expression into the ideal gas law (3.6),

$$\frac{dp}{p} = \frac{m_a g}{kT} dh,$$

and after integration, the barometric formula is

$$p_h = P_0 e^{-\frac{m_a g h}{kT}}, \tag{3.7}$$

where $P_0$ is the ground pressure at $h = 0$. A similar expression can be written for the atmospheric density at height $h$,

$$\rho_a(h) = \rho_a(h = 0) e^{-\frac{h}{H}}, \tag{3.8}$$

where, for convenience, the scale height is introduced. These two approximative expressions agree very well with the true measured pressure and density above ground up to a height of 140 km.

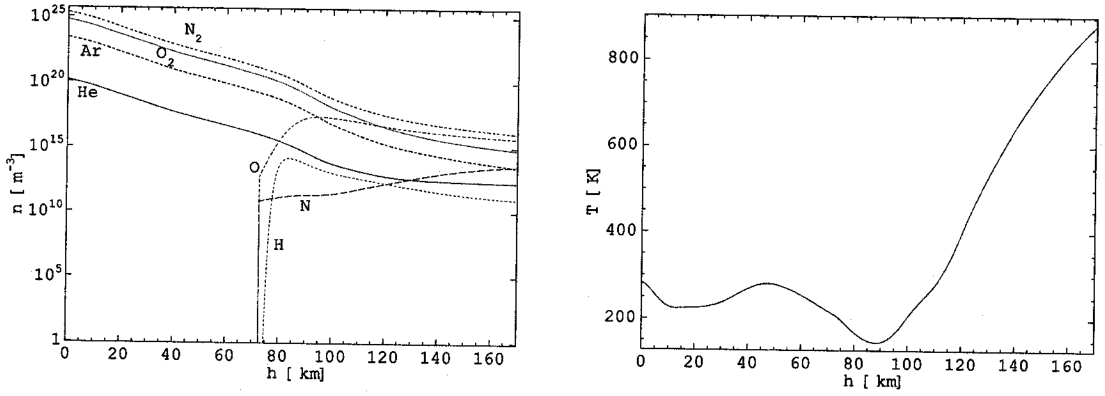

Figure 3.1: Height above ground dependence of the average number densities for 7 different atmospheric gases (left). Change of the average temperature of the air with height (right). NRLMSISE-00 model applied over Algonquin Park, Ontario, Canada.

There are better and more realistic models of the Earth's atmosphere. One of the most used empirical models updated with satellite data is the US Naval Research Laboratory model NRLMSISE-00 [107]. Plots of the temperature and number density of different atmospheric components as a function of height above the Earth's surface are given in Fig. 3.1.

### 3.1.6 Ionosphere

The upper part of the atmosphere where solar radiation ionizes a significant portion of neutral atoms and molecules is called the ionosphere. At altitudes where the density of the atmospheric media is sufficiently low, collisions among atmospheric particles are rare, implying slow ionization recombination. Above 60 km altitude, a permanent ionization of the atmosphere defines the Earth's ionosphere. Understanding the ionosphere is very important because of its effects on the propagation of radio waves. In literature, the ionosphere is usually divided into layers. Peaks in a typical electron-density versus height plot, such as the one in Fig. 3.2, are given names D, E, F, and are said to correspond to different ionospheric layers [115]. This naming system was introduced by Sir Edward Appleton in the 1920s, who named the "Electric" layer, or E layer. In reality, the ionospheric layers are not well defined, and are composed of regions with lower or higher electron densities.

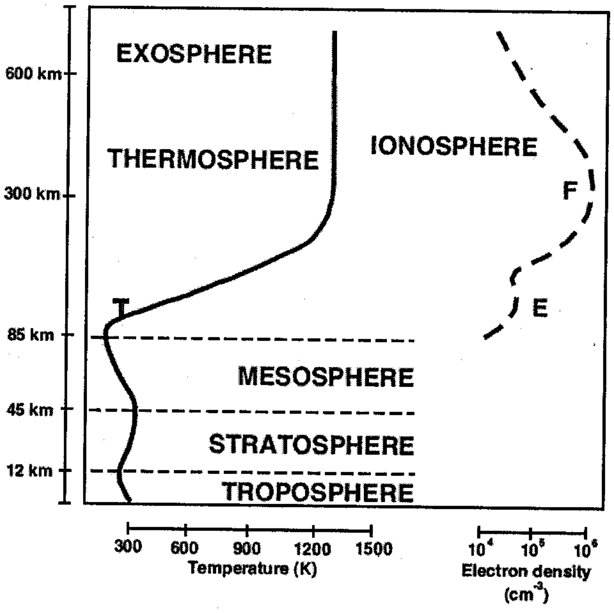

Figure 3.2: A typical temperature/electron-density vs height plot defining the atmospheric layers.

At altitudes of 50-90 km, hydrogen Lyman $\alpha$ ($\lambda$ = 121.5 nm) and hard X rays

($\lambda < 1$ nm) create the D layer, with a maximum ionization level of $10^{10}$ electrons per m$^3$. Recombination is sufficiently high at these altitudes, so the D layer exists only during daytime, and absorbs frequencies below 10 MHz. This is the reason why AM broadcasting at frequencies of 0.5-2 MHz disappears over the horizon during the daytime.

At altitudes of 90-120 km, the E layer is formed with a maximal ionization of about $10^{11}$ electrons per m$^3$. Soft X and far ultraviolet rays in the frequency range of $\lambda \sim 1-10$ nm are the primary sources of ionization for this layer. The E layer reflects frequencies of up to 10 MHz, and partially absorbs frequencies larger than 10 MHz. Sometimes a so called sporadic E layer can be formed with an ionization level high enough to allow reflection of frequencies of up to 100 MHz. The sporadic E layer is not a layer in the real sense of the word, but rather an isolated region with higher ionization. The ionization caused by meteors is also a form of a sporadic E layer.

Ultraviolet radiation ($\lambda \sim 10-100$ nm) is responsible for the creation of the F layers (F1, F2, ...) at altitudes of 120-400 km. The electron density of the F layers reaches $10^{12}$ electrons per m$^3$. Day-night variations of the ion number density are big (a factor of 10), with a maximal level of ionization during the daytime. F layers are responsible for reflecting frequencies of up to 50 MHz.

### 3.1.7 Disintegration of Meteor Trails

The trail's charged particles start disintegrating in the surrounding medium immediately after the trail is formed. Diffusion is the primary process responsible for the disintegration. Recombination, electron attachment to neutral molecules and atoms, and turbulent diffusion have also been studied as additional mechanisms limiting the duration of the trail. The usual approximation is to consider a cylindrically symmetric trail with the maximal electron density at its centre. A good overview of the disintegrating processes is given in the standard meteor textbook written by Bronshten [9].

If the disintegration is due to diffusion only, the electron concentration at the center of the trail $n_e(r = 0)$ at a time $t$ can be written as

$$n_e(r = 0) = \frac{\alpha}{4\pi D_\alpha t + \pi r_0^2} \tag{3.9}$$

Assuming cylindrical symmetry of the trail, the diffusion time depends only on the initial radius of the trail $r_0$ and the diffusion coefficient $D_\alpha$. The electron concentration at a distance $r$ from the center of the trail ($n_e(r)$) can be approximated by a Gaussian function [95]

$$n_e(r) = \frac{\alpha}{\pi r(t)^2} \exp\left[-\frac{r^2}{r(t)^2}\right], \tag{3.10}$$

where $\alpha$ is the electron line density. The radius $r$ changes with time $t$ as

$$r(t) = \sqrt{r_0^2 + 4D_\alpha t}.$$

The initial radius $r_0$ can range from 10 cm to 10 m and it can be estimated according to the work of Bronshten [9] by

$$r_0 \approx 2.58 \times 10^{10} \frac{v^{0.8}}{n}, \tag{3.11}$$

where $v$ is the velocity of the meteoroid in units of km/s, $n$ is the air-molecule number density in $\mathrm{cm}^{-3}$, and $r_0$ is given in meters. A similar result is given by Manning, 1958 [70]. In some works, such as [49], an empirical relation between $r_0$ given in meters and the meteor height given in kilometers, $r_0 = 0.035h - 3.45$, is used. Another empirical relation for $r_0$ given in meters is

$$r_0 = 1.65\sqrt{\frac{v}{40}}e^{\frac{h-95}{2H}},$$

where the velocity $v$ is given in km/s and the height $h$ is in km [133]. Observational data show indications that $r_0 \sim v^{0.8}$ [9], but the subject is still open.

The ambipolar diffusion coefficient $D_a$ determines the speed of the diffusion of the charged particles from the trail. In a first approximation, it can be calculated as [37]

$$D_a = \frac{7m_a}{8\rho_a \sigma}\sqrt{\frac{kT}{\pi \mu_m}}. \tag{3.12}$$

While many of the quantities in the above equation are constant, the most important is the dependence on the air density $\rho_a$ (see Fig. 3.1). The empirical expression [133] for $D_a$ given in $\mathrm{m}^2/\mathrm{s}$ is

$$D_a = 13.2e^{\frac{h-95}{H}}. \tag{3.13}$$

In a more detailed model, the ionized trail is assumed to have three components: electrons, positive ions, and neutral particles. The ambipolar diffusion is then a function of the ion diffusion $D_i$ [78]

$$D_a = D_i\left(1 + \frac{T_e}{T_i}\right),$$

where $T_e$ and $T_i$ are the temperatures of the electrons and ions, respectively. Furthermore, it can be assumed that $D_a = 2D_i$, since the electrons and ions reach thermal equilibrium $T_e = T_i$ with the neutral gas through collisions. The ion contribution is defined by the Einstein equation

$$D_i = \frac{k}{e}\frac{T_n^2}{273\mathrm{K}}\frac{1.013 \times 10^5\mathrm{Pa}}{p_n}K_0,$$

where $T_n$ and $p_n$ are the temperature and the pressure of the neutral gas, and $K_0 = 2.5 \times 10^{-4}\ \mathrm{m}^2\mathrm{s}^{-1}\mathrm{V}^{-1}$ is a constant estimated for the case when the only neutral component is $N_2$ and ions are a mixture of Fe(+) and Mg(+) [44], [53]. Using the data of over 6000 meteors, Verniani, 1973 estimated $D_a = 10^{0.086\,\mathrm{m}^{-1}h-7.23}\ \mathrm{m}^2/\mathrm{s}$ [145]. In the work by Thomas et al. 1988, for the U.S. Standard Atmosphere, the diffusion coefficient in the altitude range 80-125 km is approximated as $D_a = 10^{0.0758\mathrm{m}^{-1}h-6.51}\mathrm{m}^2/\mathrm{s}$ [136].

The effect of the magnetic field of the Earth on the effective diffusion coefficient of a meteor trail has been discussed in [111]. The ambipolar diffusion tensor is given for arbitrary orientations of the magnetic field. It was found that the diffusion of the plasma inside a meteor trail in a direction orthogonal to the magnetic field is much smaller than previously thought (see the estimates in the paragraph above). Robson derived the effective diffusion coefficient as

$$D_\alpha = D_{||}\sin^2\mu\sin^2\theta + D_\perp(1 - \sin^2\mu\sin^2\theta), \tag{3.14}$$

where $D_{||}$ and $D_{\perp}$ are the ambipolar diffusion coefficients parallel and perpendicular to the magnetic field, $\theta$ is the angle the field makes with the trail and $\mu$ is the angle between the wave vector and the normal to the plane of the trail and the field.

The parallel component $D_{||}$ is used as the effective coefficient when the effects of the magnetic field can be ignored. For nitrogen alkali ions, $D_{||} \approx 1.4 \times 10^{-5}\,\frac{\mathrm{m^2Pa}}{\mathrm{sK^2}}\frac{T^2}{p}$, where $T$ is the ambient temperature and $p$ is the gas pressure. Equation (3.12) can also be used to estimate the parallel component. The normal component is given as

$$D_{\perp} = \frac{D_{||}}{1 + \frac{\omega_{ge}\omega_{gi}}{f_e f_i}}, \tag{3.15}$$

where $\omega_{ge} = \frac{eB}{m_e}$ and $\omega_{gi} = \frac{eB}{m_i}$ are the gyromagnetic frequencies and $f_e$ and $f_i$ are the collision frequencies of the electrons and the ions. A height variation of the parallel and orthogonal components is given in Fig. 1. of [25]. The important implication of the influence of the Earth's magnetic field on the diffusion coefficient for higher altitude is in the extended duration of the echoes. For the height range of $70 - 120$ km the effective ambipolar diffusion coefficient typically takes values in the range $0.1 - 1000\ \mathrm{m^2/s}$ .

Fireballs splitting into a number of smaller fragments were directly observed using a photographing technique. In the general case, there are two main theoretical approaches to the theory of fragmentation [1]. Quasi-continuous fragmentation is a process when a meteoroid slowly loses individual smaller parts causing additional ablation. Gross fragmentation occurs when the body splits into smaller bodies of approximately the same size which may fragment again and again. Atmospheric fragmentation and comparison with the photographic observations are discussed by Ceplecha et al, 1993 [14]. In their work, a single body theory of a meteoroid entering the atmosphere is extended by sudden gross fragmentation. One of their main conclusions is that the ablation coefficients are lower by a factor of two than previously thought.

When the meteoroid body splits into a number of fragments, there are small differences in the velocities of individual fragments. Therefore, the fragments are separated along the meteoroids trajectory. Orthogonal fragmentation, i.e. when fragments split in the directions orthogonal to the trajectory, requires a mechanism accountable for the extra momentum, such as the rotation of the meteoric body. A simple 10 particle fragmentation model with separations along the trajectory, has shown that Fresnel oscillations are substantially reduced [26]. If the fragments were separated by more then 200 m, the oscillations are almost completely attenuated. The effects of fragmentation on different types of radar echoes recorded at Buckland Park, near Adelaide, South Australia, have been summarized in [26].

### 3.1.8 Underdense and Overdense Trails

More than half a century ago, it was noted that radio echoes can be roughly divided into two groups, depending on the electron line density of meteor trails [58]. If the linear density of free electrons is smaller than a critical value of the order of $10^{14}$ $\mathrm{m}^{-1}$, a radio wave propagates through the meteor without being attenuated. Each individual free electron scatters the incident electromagnetic wave and the result is the sum of all individual contributions in the shape of an underdense trail. When the electron line density of a trail is much higher than the critical line density, the central part of the trail behaves as a perfect conductor. The initial wave is scattered off the surface of the core, which is approximated as a metal cylinder [152]. Such trails are called overdense. These two different classes of meteor trails are shown in Fig. 3.3. We will show that the gas in meteoric trails is in a plasma state. We will also give a more detailed approach toward defining underdense and overdense trails by including the collisions in a three component plasma.

A typical underdense trail has a fast amplitude rise $\sim 0.1$ s and a slow exponential decay $\sim 1$ s due to the diffusion of the trail with an imprinted Fresnel diffraction pattern. Fresnel patterns can be smoothed out due to fragmentation of a meteoroid [26], see Fig. 3.3.

Radar observations of overdense echoes show that, as in the underdense case, initially,

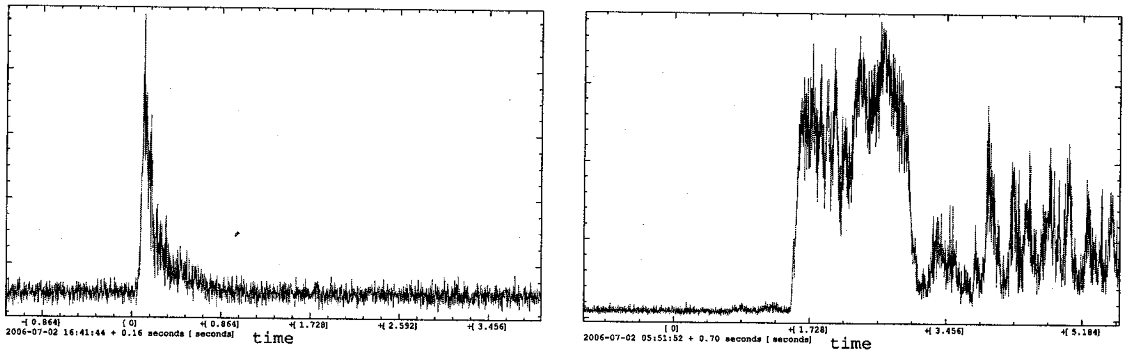

Figure 3.3: Underdense (left) and overdense (right) meteor trails with signs of fragmentation recorded during the observation run in Algonquin Park, Ontario, Canada, June 2006. The underdense trail is detected at a frequency of 88.9 MHz and the overdense trail at 101.3 MHz. Along the $y$-axis, intensity is given in arbitrary units.

the amplitude rises quickly, as fast as 0.1 s. Thereafter, the amplitude remains constant for a certain period of time before the metal cylinder approximation stops being valid. When the concentration of free electrons drops below the critical value, the trail becomes underdense and decays as an ordinary underdense trail. The effects of fragmentation can cause quite interesting effects as shown in Fig. 3.3. An excellent reference for studying various types of radar echoes is a Ph. D. dissertation by Daniel Badger, 2002 [1].

McKinley (1961), defined the critical electron line density using the condition that the dielectric constant $\kappa$ of the electron gas inside the trail's core is zero [74]. This constant is given by

$$\kappa = 1 - \frac{n_e \lambda^2}{\pi} r_e, \tag{3.16}$$

where $n_e$ is the number density of free electrons, $r_e = 2.8 \times 10^{-15}$ m is the classical electron radius, and $\lambda$ is the wavelength of the incoming radio wave. He obtained a value of $2.4 \times 10^{14}$ electrons/m.

As the region with high electron density expands, the concentration of free electrons outside the core drops and the dielectric constant becomes positive, limiting the metallic cylinder approximation. When electron line densities have moderate values, neither the overdense nor underdense, approximations hold.

An ionized meteor trail behaves as a plasma. To show that the macroscopic neutrality required of a plasma holds, we will estimate the Debye radius $r_D$ and compare it with the characteristic dimension of the trail $r_0$. The Debye sphere must be smaller than the volume of the ionized trail in order for the trail to be neutral. If we can assume that free electrons and ions are the only two charged components present inside the trail, the Debye radius is

$$\frac{1}{r_D^2} = \sum_{i=1}^{2} \frac{e_i n_i}{\epsilon_0 k T_i}, \tag{3.17}$$

where the summation is over the particle types (in our case electrons and ions) $e_i$, $n_i$, $T_i$ are the charge, the number density and the temperature of the components, respectively, and $k = 1.3806503 \times 10^{-23}$ J/K is Boltzmann's constant.

Assuming that the gas is isothermal, $T_1 = T_2 = T_e$, and that the number densities are the same, $n_1 = n_2 = n_e$, since free electrons were initially bound to the positive ions, it follows that

$$r_D = \sqrt{\frac{\epsilon_0 k T_e}{2 e n_e}}. \tag{3.18}$$

A more correct expression would include neutral air particles as well. Knowing that the ablation temperature is on the order of $10^4$ K, and assuming the lower limit for the number density of detected radio trails to be $10^{11}$ m$^{-3}$, we estimate $r_D \approx 0.01$ m. Comparing with the minimal value for $r_0$ of 0.1 m, we see that the neutrality condition is fulfilled.

The next condition for a plasma is that the plasma oscillations cannot be dampened via the influence of particle collisions. The plasma oscillation frequency must be higher than the collisional frequency. Since the electrons move faster than the ions, they provide the main contribution to the plasma frequency. If the electrons in the plasma are offset from their equilibrium position, they execute simple harmonic motion. The equation of motion for the electrons gives the characteristic angular frequency of oscillation:

$$\omega_p = \sqrt{\frac{n_e e^2}{\epsilon_0 m_e}}. \tag{3.19}$$

The plasma or Langmuir frequency is one of the most important collective characteristics of the plasma.

Roughly, there are three types of particles defining the behavior of the ionized trails as far as collisions are concerned: free electrons, ions and neutrals. The collision frequency $f_c$ of free electrons thus has a contribution from electron-electron $f_{ee}$, electron-ion $f_{ei}$ and electron-neutral $f_{en}$ collisions:

$$f_c = f_{ee} + f_{ei} + f_{en}. \tag{3.20}$$

The collisional frequency due to electron-electron and electron-ion impacts can be calculated as [78], [109]

$$f_{ee} + f_{ei} = \frac{4}{3}\sqrt{\frac{2\pi}{m_e}}\left(\frac{ee_i}{4\pi\epsilon_0}\right)^2 \frac{n_e}{(kT_e)^{3/2}} L_{ei}, \tag{3.21}$$

where $e_i$ is charge of the ions. For an isothermal plasma, $L_{ei}$ is the electron-ion collision constant defined by

$$L_{ei} = \ln\left[\frac{12\pi\epsilon_0}{ee_i^2}\sqrt{\frac{\epsilon_0}{n_i}}\,(kT)^{3/2}\right] \tag{3.22}$$

Collisions between charged and neutral particles are usually modelled using the rigid sphere approximation. The collision cross section $\sigma_{en}$ between these two types of particles does not depend on the relative velocity. Following [78], we set $\sigma_{en} = 10^{-19}$ m$^2$. Assuming that the relative velocity is equal to the thermal velocity of free electrons, the collisional frequency $f_{en}$ is

$$f_{en} = n_n \sigma_{en} v_e, \tag{3.23}$$

where $n_n$ is the concentration of neutral particles and $v_e = \sqrt{\frac{kT_e}{m_e}}$ is the thermal velocity of the electron gas. Collisions with neutrals are of great importance in the physics of meteor trails when the concentration of free electrons is less than $10^9$ m$^{-3}$. In Fig. 3.4, the electron-neutral collision frequency is compared to the collisional frequency due to electron-electron and electron-ion impacts. For such low values, the trail can not be treated as a plasma; however, the reader should note that most radars are not capable of detecting trails with such low values of $n_e$.

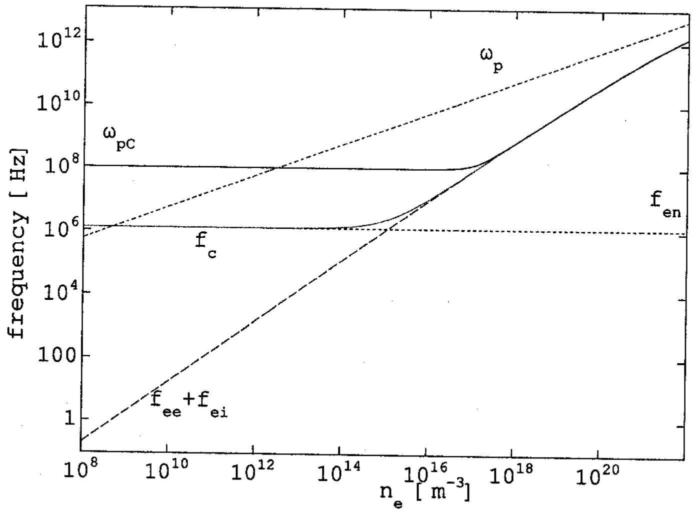

Figure 3.4: The plasma frequency $\omega_p$, the collision frequencies $f_{ee} + f_{ei}$, $f_{en}$, $f_c$, and the critical plasma frequency $\omega_{pC}$, versus the mean electron density $n_e$ . The three component plasma is considered to be isothermal with $T_e = 1000$ K, and isotropic with the same number density of free electrons and positive ions $n_e$. The critical plasma frequency is plotted for the case when the incident wave has a frequency of 100 MHz.

A comparison of the collision frequency with the Langmuir frequency for the range of the electron mean number densities is given for a temperature of $T_e = 10^4$ K (Fig. 3.4). From the plot, it can be seen that for low number densities of free electrons up to $n_e \sim 10^{14}$ m$^{-3}$, a dominant contribution to the collisional frequency of free electrons is due to impacts with neutral particles. For this range, $f_c$ is constant and on the order of $10^6$ Hz. For higher values of free electron number densities, electron-electron and electron-ion collisions become dominant. The collisional frequency might go over $10^{10}$ Hz depending on the electron number density.

The Langmuir frequency is given in the same plot. We can clearly see that the

Langmuir frequency is higher than the collisional frequency in the interval important for the radio scattering of meteor trails, $10^9 - 10^{22}$ m$^{-3}$. Thus, the second condition for the plasma state is also satisfied so the ionized gas in meteor trails can be treated as a plasma.

A dispersion equation for wave propagation in plasma should be derived to clearly see what happens when an incident wave scatters off the meteoric plasma. With minor changes, we will follow the approach taken in Foschini, 1999 [32].

Let us start with the perturbation equations for the four Maxwell equations

$$\nabla \cdot \mathbf{E}' = \frac{\rho'_{el}}{\epsilon_0} \tag{3.24}$$

$$\nabla \times \mathbf{E}' = -\frac{\partial \mathbf{B}'}{\partial t} \tag{3.25}$$

$$\nabla \cdot \mathbf{B}' = 0 \tag{3.26}$$

$$\nabla \times \mathbf{B}' = \mu_0 \mathbf{j}' + \epsilon_0 \mu_0 \frac{\partial \mathbf{E}'}{\partial t} \tag{3.27}$$

together with a generalized version of Ohm's law

$$\mathbf{j} = \sigma \left(\mathbf{E} + \mathbf{v} \times \mathbf{B}\right) + \rho_{el}\mathbf{v}. \tag{3.28}$$

$\mathbf{E}'$ and $\mathbf{B}'$ are the perturbations of the electric field intensity $\mathbf{E}$ and the magnetic induction $\mathbf{B}$ vectors, respectively. $\epsilon_0 = 8.8541878176 \times 10^{-12}$ C$^2$/Jm is the permittivity of free space, and $\mu_0 = 4\pi \times 10^{-7}$ N/A$^2$ is the magnetic permeability of a vacuum. These two constants define the speed of light in a vacuum as $c^2 = \frac{1}{\epsilon_0 \mu_0}$. $\sigma$ is the electrical conductivity and $\rho_{el}$ is the charge density. Plasma is macroscopically neutral, so the charge density can be assumed to be $\rho_{el} = 0$. For the sake of simplicity, we will assume a cold plasma model by neglecting density perturbations. In a more detailed magneto-hydrodynamic approach used when considering longitudinal modes of the wave propagation, the density perturbations should not be neglected. The electric conductivity, in the case of a meteoric plasma, depends on the number density of free electrons $n_e$, and on the mean collision frequency $f_c$. It is given by

$$\sigma = \frac{n_e e^2}{m_e(f_c - i\omega)}. \tag{3.29}$$

The magnetic field important for the the generalized version of Ohm's law is the Earth's geomagnetic field. However, it can be neglected because the electron gyro frequency $\omega_g = \frac{eB}{m_e}$ [100] is much smaller than the frequency of the incident radio wave [32]. Taking into account all of the above approximations, the perturbation of the vector $\mathbf{j}$ is

$$\mathbf{j}' = \sigma \mathbf{E}' \tag{3.30}$$

If a transmitter emits continuous waves, the electric field vector varies periodically with time as

$$\mathbf{E}' = \mathbf{E_0}' e^{i(\mathbf{kr} - \omega t)}. \tag{3.31}$$

By applying $\nabla\times$ to (3.25) and (3.27), and using the vector identity

$$\nabla \times (\nabla \times \mathbf{A}) = \nabla(\nabla \cdot \mathbf{A}) - (\nabla\nabla) \cdot \mathbf{A} \tag{3.32}$$

it follows that

$$\nabla^2 \mathbf{E}' + (i\sigma\epsilon_0\mu_0 + \omega^2\epsilon_0\mu_0)\mathbf{E}' = 0; \tag{3.33}$$

$$\nabla^2 \mathbf{B}' + (\sigma\mu_0 - i\omega\epsilon_0\mu_0)\mathbf{E}' = 0; \tag{3.34}$$

In Foschini, 1999 [32] the last equation is incorrectly derived, most likely a typo. Fortunately, it was not used later in the text. The solutions for these two equations are the nonuniform harmonic plane waves with a complex wave vector. Substituting (3.31) in (3.33), the dispersion equation can be obtained

$$k^2 = \omega^2 \mu_0 \epsilon_0 + i\omega\mu_0\sigma. \tag{3.35}$$

Replacing $\sigma$ with expression (3.29), the equation becomes

$$k^2 = \frac{\omega^2}{c^2}\left[1 - \frac{\left(\frac{\omega_p}{\omega}\right)^2}{1 + \left(\frac{f_c}{\omega}\right)^2} + i\left[\frac{\left(\frac{\omega_p}{\omega}\right)^2 \frac{f_c}{\omega}}{1 + \left(\frac{f_c}{\omega}\right)^2}\right]\right]. \tag{3.36}$$

In the case when the frequency of the incident wave is much higher than the collisional frequency, this equation simplifies to

$$k^2 = \frac{\omega^2}{c^2}\left[1 - \left(\frac{\omega_p}{\omega}\right)^2\right]. \tag{3.37}$$

When an incident wave has a frequency $\omega \sim 100$ MHz, the validity of this equation is limited to trails with $n_e < 10^{17}$ m$^{-3}$ (see Fig. 3.4). If $n_e$ has a higher value, the collisional frequency has to be taken into account, as discussed a few paragraphs below.

There are two recognizable classes of meteors based on the comparison of the Langmuir frequency to the frequency of the incoming radio beam. For the case when the incident wave frequency is higher then the Langmuir frequency, the wave vector is composed only of a real part, and the wave propagates without being attenuated (underdense). If the frequency of the incident wave is lower than the plasma frequency, the wave vector has only an imaginary part and the incident wave is completely reflected (overdense). The free electrons have enough time to rearrange themselves to shield the interior from the incident electromagnetic field.

A more detailed approach, valid for the complete range of free electron number densities is to include the collision frequency. The critical plasma frequency $\omega_{pC}$ is introduced to distinguish between the underdense and overdense trails. It depends only on the mean collision and the incident wave frequency.

$$\omega_{pC}^2 = \omega^2 + f_c^2. \tag{3.38}$$

Knowing $\omega_{pC}$ (see Fig. 3.4), the critical number density of electrons ranges from $10^{12}$ m$^{-3}$ for $\omega \sim 40$ MHz, to more than $10^{14}$ m$^{-3}$ for $\omega > 100$ MHz.

As waves pass through an ionized gas, and especially a plasma, the plane of polarization changes. The effect is known as Faraday rotation. In a magnetic medium, a linearly polarized wave is separated into two modes, ordinary and extraordinary waves, with different phase velocities. At every point in the medium, the two modes superpose in a single linear wave, but with the plane of polarization slightly rotated. The smaller the frequency of the incident wave, the smaller the effect of Faraday rotation due to the smaller difference between the phase velocities [78]. Faraday rotation is of great importance for frequencies in the range 15-40 MHz [117].

## 3.2 Radio Observations of Meteor Trails

Depending on the geometry of the propagation line, there are two methods of observing meteor trails. In a radar or a back-scatter system, the transmitter and the receiver are located in the same spot, while in a forward-scattering setup, the transmitter and the receiver are located further away than line-of-sight from each other. As mentioned earlier, coherent scattering is possible only if both stations, the transmitter and receiver, are at the foci of a prolate spheroid (ellipsoid), and a meteor trail is a line tangent to the ellipsoid. In the case of radar observations, the ellipsoid becomes a sphere which makes data analysis much simpler than in the more general case of forward-scattering. In this subsection, the theory behind radar observations is discussed before moving on to the forward-scattering situation.

### 3.2.1 Principles of Radar Reflection: Underdense trails

The theory behind back-scattering is discussed in multiple places in detail (see for example [74]). Here we will follow the approach from [1] to obtain the received power after reflection from an underdense trail. The flux $\Phi_1$ of the incident wave emitted by a transmitter with antenna gain $G_T$ at a distance $d$ from the transmitter is

$$\Phi_1 = \frac{P_T G_T}{4\pi d^2},$$

where $P_T$ is the transmitted power. The scattering cross section $\sigma_e$ of a free electron is

$$\sigma_e = 4\pi r_e^2 \sin^2 \gamma, \tag{3.39}$$

where $r_e$ is the classical electron radius and $\gamma$ is the angle between the electric vector of the incident wave and the line of sight of the receiver. $\gamma = \frac{\pi}{2}$ for the case of back-scattering. The contribution of a single electron to the received signal is

$$\Phi_2 = \frac{P_T G_T}{4\pi d^2}\left(\frac{r_e}{d}\right)^2. \tag{3.40}$$

Assuming that the trail diameter is small compared to the wavelength, all free electrons in a small region of the trail defined by the small line $ds$ along the trail, will scatter in phase producing the maximum possible amplitude of the electric field $E_0$

$$E_0 = \alpha\sqrt{2Z_0\Phi_2}ds,$$

where $Z_0$ is the wave impedance of free space, and $\alpha$ is the line density of free electrons on the trail. If the transmitted wave had a sinusoidal modulation of shape $e^{i\omega t}$, then the returned signal will have its phase shifted by $-2\frac{2\pi}{\lambda}d$. The signal due to the whole trail, $E_R$, is easily obtained after integration along the trail:

$$E_R = \int \alpha\sqrt{2Z_0\Phi_2}e^{i(\omega t - \frac{4\pi}{\lambda}d)}ds.$$

For simplicity, $\alpha$ is assumed to be constant, and only the exponential function stays inside the integral. A common approximation [1] is $d \approx d_0 + \frac{s^2}{2d_0}$ where $s$ is the distance along the trail from the region of the trail defined by $ds$ to the orthogonal point, in radar terminology known as the $t_0$ point. The error introduced with such an approximation is on the order of 0.001% [1]. If the Fresnel length is $x = \frac{2s}{\sqrt{d_0\lambda}}$, the integral is reduced to

$$E_R = \alpha\sqrt{\frac{Z_0\Phi_2 d_0\lambda}{2}}e^{i(\omega t - \frac{4\pi}{\lambda}d_0)}\sqrt{\frac{2}{\pi}}(C_{x_1,x_2} - iS_{x_1,x_2}), \tag{3.41}$$

where integrals $C_{x_1,x_2} = C(x_2) - C(x_1)$ and $S_{x_1,x_2} = S(x_2) - S(x_1)$ are defined by the Fresnel integrals (see Fig. 3.5)

$$C(x) = \int_0^x \cos y^2 dy, \tag{3.42}$$

$$S(x) = \int_0^x \sin y^2 dy. \tag{3.43}$$

The borders $x_1$ and $x_2$ are defined by the length of the trail, from the initial point of the trail (in some works, $x_1 = -\infty$ [152]), through the $t_0$ point up to the last point of the trail.

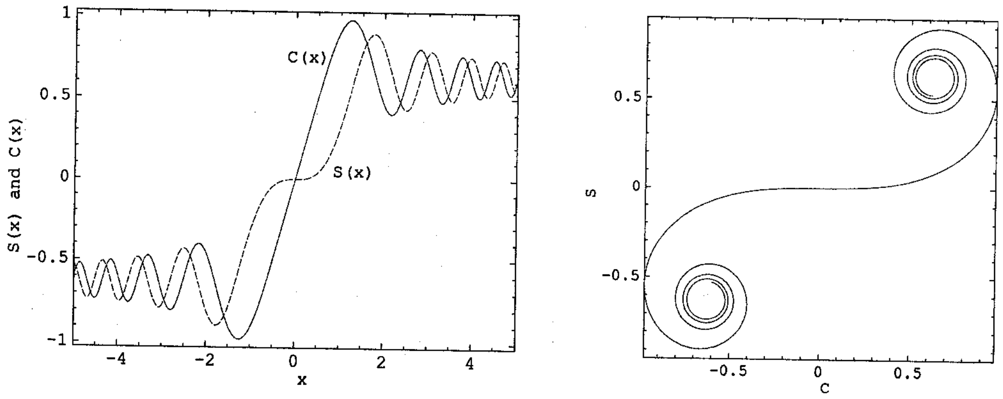

Figure 3.5: Fresnel integrals $C(x)$ and $S(x)$ (left) and the Cornu spiral of Fresnel diffraction $C$ vs $S$ (right). In the right plot $x$ goes from -5 to 5.

The Fresnel integrals can be expanded into a Taylor series as

$$S(x) = \int_0^x \sin y^2 dy = \sum_{n=0}^{\infty} (-1)^n \frac{x^{4n+3}}{(4n+3)(2n+1)!} \tag{3.44}$$

$$C(x) = \int_0^x \cos y^2 dy = \sum_{n=0}^{\infty} (-1)^n \frac{x^{4n+1}}{(4n+1)(2n)!}. \tag{3.45}$$

$$\tag{3.46}$$

The resulting power flux $\Phi_R$ is

$$\Phi_R = \frac{E_R^2}{2Z_0} = \Phi_2 \frac{\alpha^2 d_0 \lambda}{\pi} \left( C_{x_1,x_2}^2 + S_{x_1,x_2}^2 \right),$$

and finally, the received power $P_R$ at the receiver antenna with gain $G_R$ is

$$P_R = P_T G_T G_R \frac{\alpha^2 \lambda^3 r_e^2}{32\pi^3 d_0^3} \left( C_{x_1,x_2}^2 + S_{x_1,x_2}^2 \right). \tag{3.47}$$

The amplitude of the received signal is maximal when the meteoroid reaches the first Fresnel zone. By definition, the first Fresnel zone extends to the point where the distance

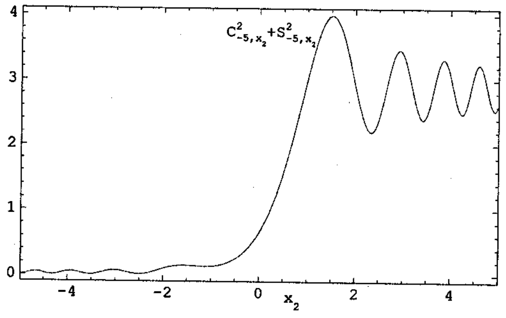

Figure 3.6: Function $C^2_{x1,x2}+S^2_{x1,x2}$ governing the shape of a meteor reflection as a function of $x_2$ for fixed $x_1 = -5$.

from the $t_0$ point is $\lambda/2$, changing the phase of the wave by $\pi$. Using the formalism given above, $x_2 = 1.51$ (see Fig. 3.6). After crossing the first Fresnel zone, the amplitude oscillates with decreasing magnitude and increasing frequency. The time evolution of the received power also strongly depends on the trail disintegration.

### 3.2.2 Principles of Radar Reflection: Overdense Trails

If the electron line density is sufficiently high, above $10^{15}$ m$^{-1}$, the metal cylinder approximation applies. The incident radiation is reflected off the cylindrical trail and no radiation enters inside the highly ionized zone. This is just a rough approximation, since only the central part of the trail can have the overdense character, while all around an underdense shell is formed. In order to have a total reflection, the dimensions of the cylinder have to be bigger than the wavelength of the incident wave.

The overdense region is defined by the critical radius, i.e. the distance from the center of the trail within which the dielectric constant is zero. From equation (3.10) we have

$$r = \sqrt{(r_0^2 + 4D_\alpha t)\ln\frac{\alpha}{n_e\pi(r_0^2 + 4D_\alpha t)^2}}. \tag{3.48}$$

The condition of zero dielectric constant from (3.16) gives

$$\frac{n_e \lambda^2}{\pi} r_e = 1.$$

Combining these two relations, the number density of electrons can be removed and

$$r = \sqrt{(r_0^2 + 4D_\alpha t) \ln \frac{\alpha \lambda^2 r_e}{\pi^2 (r_0^2 + 4D_\alpha t)^2}}.$$

The maximal radius $r_c$ is obtained by taking the time derivative of this equation and looking for a maximum by equating the derivative with zero:

$$r_c = \sqrt{\frac{\alpha \lambda^2 r_e}{\pi^2 e}}. \tag{3.49}$$

The echoing area of the metal cylinder at distance $d$ from the source is $\pi r_c d$. A fraction of the transmitted signal hits the echoing surface and a portion of the reflected signal reaches the receiving antenna with collective area $\frac{G_R \lambda^2}{4\pi}$. The received power $P_R$ in the case of an overdense trail is

$$P_R = \frac{P_T G_T G_R \lambda^3}{64 \pi^3 d^3} \sqrt{\frac{r_e \alpha}{e}}. \tag{3.50}$$

This relation was derived in McKinley, 1961 [74], and slightly revised by Ceplecha et. al. 1998 [15]. The main correction is that the line electron density varies as $\alpha^{0.55}$.

### 3.2.3 Forward-Scattering: Underdense Trails

The scattered signal in the forward scatter observations will be received only from those trails which are tangential to an ellipsoid with foci at a transmitter T and a receiver R. Obviously, radar observation is a special case of forward-scattering, when the ellipsoid has both foci at one point: a sphere.

The first attempts to understand the geometry of the forward scatter system were made in the 1950s. In the cylindrical approximation, the ellipsoid is replaced by a cylinder drawn around the T-R baseline [41]. This approach works well only if the meteor trails are orthogonal to the T-R axis. Hines, 1958 suggested more accurate approach by using elliptical geometry [42]. His method will be discussed below in order to give a simple feel for the shape of a detected raise in amplitude in the case of an underdense meteor. Hines' efforts resulted in the estimation of the total number of observable trails as a function of trail orientation. Due to several approximations used, his work is incomplete in the light of the results presented in this paper.

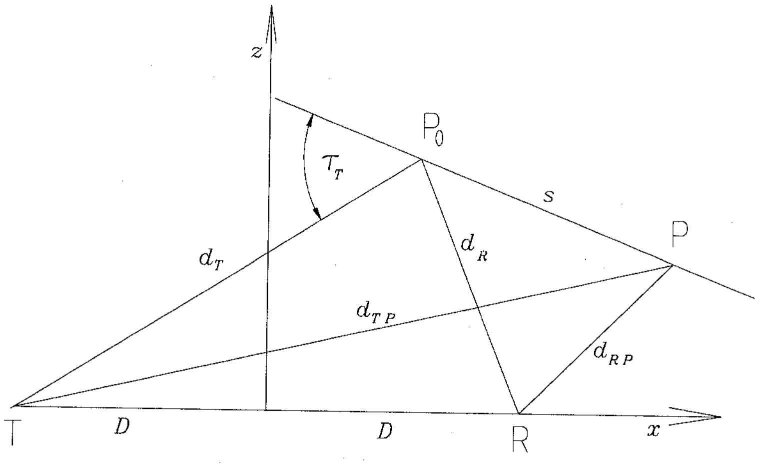

Figure 3.7: Geometric parameters describing meteor forward-scattering: 2D case.

Let $P_0$ be a particular point on a trail with rectangular coordinates $(x_0,\ y_0,\ z_0)$ in a Cartesian coordinate system with the origin at the central point between T and R (see Fig. 3.7 for a 2D projection). A general point P on the linear trail will have coordinates $(x_0+\eta_x s,\ y_0+\eta_y s,\ z_0+\eta_z s)$, where $s$ is the distance $P_0P$. The distance from the transmitter to P is

$$d_{TP} = \sqrt{(x_0+\eta_x s+D)^2+(y_0+\eta_y s)^2+(z_0+\eta_z s)^2}, \tag{3.51}$$

where $D$ is half of the length of the baseline TR. After expanding the Taylor series in $s$, (3.51) can be written in terms of the distance from T to $P_0$ ($d_T$):

$$d_{TP} = d_T\left[1+\frac{s}{d_T}\cos\tau_T+\frac{s^2}{2d_T^2}\sin^2\tau_T+...\right], \tag{3.52}$$

where $d_T = \sqrt{(x_0 + D)^2 + y_0^2 + z_0^2}$. The angle between the trail and the line $TP_0$ is $\tau_T$ defined by

$$\cos \tau_T = \frac{\eta_x(x_0 + D) + \eta_y y_0 + \eta_z z_0}{d_T}. \tag{3.53}$$

Similar expressions can be written for the receiver, with $d_T \longrightarrow d_R$, $d_{TP} \longrightarrow d_{PR}$ and $\tau_T \longrightarrow \tau_R$.

At the point of tangency the distance $d_{TP} + d_{PR}$ must be minimal, thus the derivative $\frac{d}{ds}(d_{TP} + d_{PR}) = 0$. If $s \ll d_T$, $d_R$, after derivation

$$s = -\frac{\cos \tau_T + \cos \tau_R}{\frac{\sin^2 \tau_T}{d_T} + \frac{\sin^2 \tau_R}{d_R}}. \tag{3.54}$$

For the reflection point $s = 0$, it follows that $\cos \tau_T + \cos \tau_R = 0$, or after solving the trigonometric equation, $\tau_T + \tau_R = \pi$.

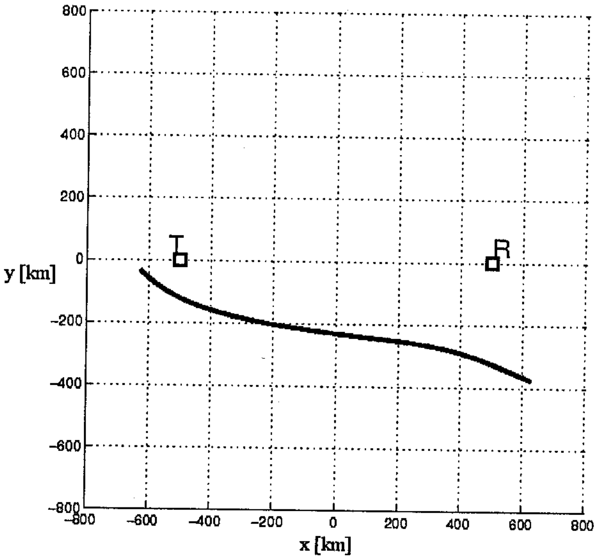

Figure 3.8: $s = 0$ curve for the position of the radiant given in horizontal spherical coordinates with the origin in the center point between the transmitter T and the receiver R (azimuth, zenith angle)=(60°, 30°); TR distance is 1000 km and $h = 100$ km. $x$ and $y$ are given in kilometers and represent the coordinates in the TR plane. Courtesy of Pavol Zigo [158].

The previous set of equations written for TP and PR can be numerically solved for the reflection point ($s = 0$) at height $h$ with the condition $z_0 = \sqrt{(R_E + h)^2 - x_0^2 - y_0^2}$ in order to obtain $y_0$ as a function of $x_0$ for a particular radiant [144], [4], [158]. An example is given in Fig. 3.8. The limitations of the method are quite obvious due to the required approximations. We will return to this problem shortly, when the full solution will be given.

In the first approximation, the Fresnel length is defined by the position of the meteoroid at time $t$

$$x = vt\sqrt{\frac{2(d_T + d_R)(1 - \sin^2\phi\cos^2\beta)}{\lambda d_T d_R}}, \tag{3.55}$$

where $t = 0$ is defined to be the time when the meteoroid reached the $t_0$ point [144], $\beta$ is the angle of the trail relative to the plane formed by $d_T$ and $d_R$, and $\phi$ is the propagation angle.

The meteor forward-scattering process is very complex due to a number of parameters affecting the ionized trail. Underdense trails can be treated using an analogy with backward-scattering. A cylindrical trail, with electron distribution being Gaussian in the radial direction, has an electron density low enough so that the individual electrons behave like Hertzian dipoles. The received power is then

$$P_R = \frac{P_T G_T G_R \lambda^3 r_e^2}{16\pi^3} \frac{\alpha^2 \sin^2\gamma}{d_T d_R (d_T + d_R)(1 - \sin^2\phi\cos^2\beta)} \left(C^2_{x_1,x_2} + S^2_{x_1,x_2}\right), \tag{3.56}$$

where $P_T$ is the transmitter power, $G_T$ and $G_R$ are the gains of the transmitter and the receiver, $d_T$ and $d_R$ are the distances from the transmitter and the receiver to the trail, $l$ is the wavelength, $\alpha$ is the linear electron density and $\sin\gamma$ is the polarization coupling factor. The integrals $C_{x_1,x_2}$ and $S_{x_1,x_2}$ are defined above as the functions of Fresnel integrals. A number of the unknown parameters in equation (3.56) makes it hard to use.

In Fig. 3.9, the time evolution of the received power is shown (top curve). The amplitude has maximal value at the moment when the meteoroid is in the first Fresnel zone. As time passes, the amplitude oscillates around the asymptotic value. Since diffusion is not included, the meteor trail does not decay and the signal lasts forever.

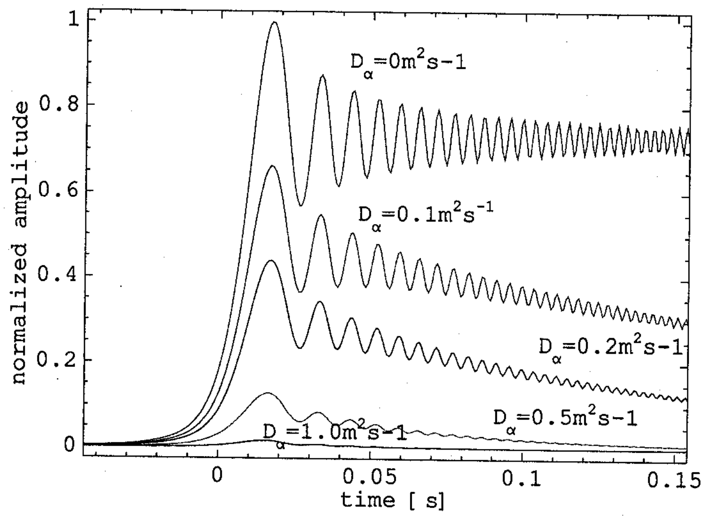

Figure 3.9: Time evolution of amplitudes of the received forward-scattered waves for the different diffusion coefficients $D_\alpha = (0,\ 0.1,\ 0.2,\ 0.5,\ 1.0)$ m$^2$s$^{-1}$. The remaining parameters are $v = 30$ km/s, $\lambda = 1$ m, $\phi = 0$, $\beta = \pi/2$, $d_R = 200$ km and $d_R = 300$ km.

The trail disintegration can be added to the power equation as an exponential diffusion decay

$$P_R(t) = P_R e^{\frac{-32\pi^2 Dt\cos^2\phi}{\lambda^2}} e^{\frac{-8\pi^2 r_0^2\cos^2\phi}{\lambda^2}}. \tag{3.57}$$

The influence of the diffusion on the amplitude of the received signal is also shown in Fig. 3.9. The higher the diffusion coefficient, the faster the trail disintegrates. The disintegration stops when the amplitude hits zero.

Another interesting consequence of equations (3.55) and (3.57) is the influence of the meteoroid velocity on the Fresnel oscillations. The higher the velocity, the faster the meteoroid will reach successive Fresnel points and the oscillations will be faster, while the amplitude will have the same intensity. A plot of amplitudes versus time for different velocities is given in Fig. 3.10. If the amplitude data are sampled fast enough, and if the geometry of the reflection is known, it is possible to determine the meteoroid velocity by fitting the theoretical model to the observed data

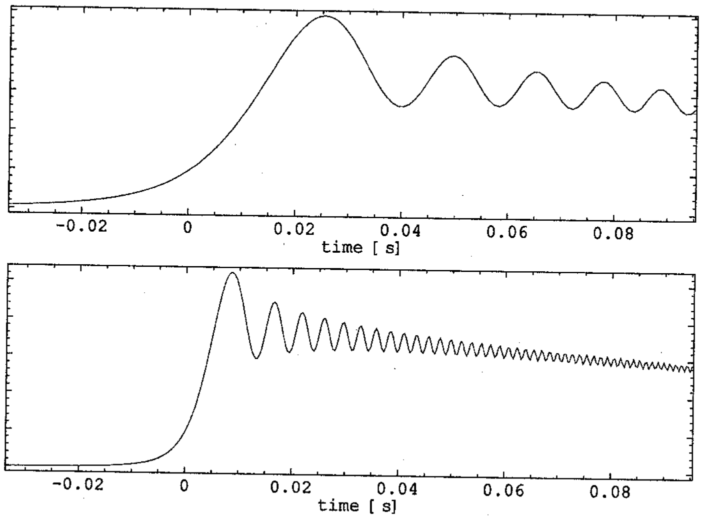

Figure 3.10: Amplitudes of the received forward-scattered waves for two different meteoroid velocities $v = 20$ km/s (top) and $v = 60$ km/s (bottom). $D_\alpha = 0.1$ m$^2$s$^{-1}$. Other parameters are the same as in Fig. 3.9.

### 3.2.4 Forward-Scattering: Overdense Trails

The expression for the power received after the forward scatter reflection off overdense trails is obtained by generalizing the radar case [74]:

$$P_R = \frac{P_T G_T G_R \lambda^3 r_e^{0.5}}{32\pi^3 e^{0.5}} \frac{\alpha^{0.5} \sin^2 \gamma}{d_T d_R (d_T + d_R)(1 - \sin^2 \phi \cos^2 \beta)}. \tag{3.58}$$

The diameter of the cylinder must be bigger than the wavelength of the incident wave. The overdense core is surrounded by an underdense shell which is not taken into account, thus limiting the validity of equation (3.58).

Timewise, there are three regions of overdense reflection. Before the meteoroid reaches the $t_0$ point, the amplitude of the received signal grows in the same way as in the case of the underdense trail. At this stage, the diameter of the cylinder is smaller than the wavelength of the initial wave so the above approximation fails. In the second stage, the overdense trail is formed and the signal behaves according to (3.58). Finally, the diffusion lowers the linear electron density below the critical value, and the trail becomes underdense.

The significant difference between the received signal reflected off the underdense and overdense trails is that overdense trails have a quick rise in amplitude. Following this, the received power is in stagnation for a certain time period which can be on the order of 10 s. In the last stage of the overdense trail's life, the trail exponentially decays in a similar manner to underdense trails.

There were very few attempts to solve the problem of forward-scattering in the general case. In 1990, Jones J. and Jones W. approached the problem of oblique scattering of radio waves from meteor trails by neglecting the collision frequency inside the ionized trails and assuming that the wavelength of the incident wave is much longer than the radius of the trail (long wavelength approximation) [54], [55], [56]. In the case of underdense trails, they managed to confirm equation (3.56). However, for the case of overdense trails, a long wavelength approximation does not hold [55] and a numerical approach was used [56]. The approximation that collisions are neglected is valid only in a certain range of electron number densities (see Fig. 3.4). The lower boundary is constrained due to collisions of free electrons with neutrals, while on the upper end, collisions with ions become an important factor. An elegant proof that meteor trails should be treated like a plasma, as well as a discussion on the importance of the different types of collisions, were given in subsection 3.1.8.

### 3.2.5 Meteor Burst Communication

In the 1950s it was proposed to use meteor forward-scattering as a method for over-the-horizon communication of distances up to 2400 km [29]. Every day, millions of meteoroids enter the atmosphere producing sufficient ionization for scattering radio waves. When a meteor trail is in a "good" position, communication between two stations, located beyond the horizon with respect to each other, becomes possible. The duration of such a link depends on the lifetime of an ionized trail, typically on the order of a fraction of a second.

The principles of meteor burst communication are relatively simple. The first station constantly emits a pooling signal. The second station listens until it receives the pooling signal. Once the signal is received, the station sends an acknowledgment. After the first station receives the answer, it starts streaming data and a link is formed. Each message is split into a set of packets containing a header with the essential link control information (package number, synchronization, station identification and error control) and a portion of the message. The receiving station sets the received packets in a receiving queue until all message packets are received. In the final step, the packets are connected in a single message.

Communication systems designed using meteor scattering are more resistant to interception, detection, and jamming than conventional systems. In the case of nuclear detonation, such systems have a significantly higher reliability than HF and satellite systems [98]. While they would be initially disturbed by a nuclear blast, the recovery time of a meteor burst communication channel would be on the order of minutes. On the other hand, the bandwidth of existant meteor burst communication systems is only a few hundred bits per second, which compared to other common communication systems is very low [116], [117].

The Snow Pack Telemetry System operated by the USA Department of Agriculture is the largest working meteor burst communication system. It spreads over 10 western states and has two master and 500 remote stations positioned in inaccessible terrain. The stations are unmanned and powered using solar collectors. Once a day, each station sends a daily weather report. The system has been active since 1978. Another example is the network of remote weather stations in Alaska, owned by US National Weather.

## 3.3 Geometry of Forward Scattering

In this section, a method for checking whether a given meteor is going to trigger a reflection of a radio wave emitted at a transmitter T, and received at a receiver R, is developed.

As already briefly mentioned, coherent scattering in the general case occurs when a meteor trail is tangent to an ellipsoid with foci at the transmitter ($x_T$, $y_T$, $z_T$) and the receiver.($x_R$, $y_R$, $z_R$). The equation of the ellipsoid in its native coordinates is

$$\frac{x^2}{a^2} + \frac{y^2}{b^2} + \frac{z^2}{c^2} = 1, \tag{3.59}$$

where $a$, $b$ and $c$ are the semi-major axes. Since the ellipsoid has only two foci and the projection of a meteor trail is a line then $c$ must be equal to $b$. The equation of a plane tangent to the ellipsoid can be obtained by taking a derivative of (3.59) at an intersection point ($x_1$, $y_1$, $z_1$):

$$\frac{xx_1}{a^2} + \frac{yy_1}{b^2} + \frac{zz_1}{b^2} = 1. \tag{3.60}$$

### 3.3.1 Forward-Scattering Analysis: Numerical Approach

Let us assume that the transmitter T and the receiver R have known positions. To find whether a meteor trail defined by a point ($x_M$, $y_M$, $z_M$) and a velocity vector ($v_{Mx}$, $v_{My}$, $v_{Mz}$) is indeed tangential to an ellipsoid with foci at T and R, we can check whether equation (3.60) is satisfied to a given precision $\delta$ for any point along the meteor line. Knowing that only a part of the meteoric line at altitudes between 70 and 120 km has a physical meaning, one can numerically loop through this range of altitudes and check whether the condition for a tangent plane is satisfied:

$$\left|\frac{x_M x}{a^2} + \frac{y_M y}{b^2} + \frac{z_M z}{b^2} - 1\right| < \delta. \tag{3.61}$$

The main problems of this method are choosing the parameter $\delta$ and defining the numerical resolution for looping through the meteor line. It is important to notice that if the resolution and the parameter $\delta$ are not matched, the true solution might get skipped. This algorithm is slow and the results are not certain.

A similar approach has been used for calculating probabilities of establishing links for meteor burst communication [117]. Rudie, N. J. in his Ph.D. dissertation derived a vector condition for a line normal to an ellipsoid [113]. At the point of reflection, defined by vectors $\mathbf{R}_T$ and $\mathbf{R}_R$ from the reflection point to the foci in the transmitter and the receiver respectively, the normal $\mathbf{N}$ to the ellipsoid is

$$\mathbf{N} = \frac{1}{2}\left[\frac{\mathbf{R}_T}{|\mathbf{R}_T|} + \frac{\mathbf{R}_R}{|\mathbf{R}_R|}\right] \tag{3.62}$$

This condition can be numerically used to verify whether a given meteoroid will cause a reflection for a specific transmitter and receiver. Rudie's method is very similar to the one given by equation (3.61). The main weakness is that the point of reflection is not known which complicates the calculation, making it strongly dependent on algorithm resolution.

### 3.3.2 Forward-Scattering Analysis: Analytical Solution

Let us define a line in 3D by using two points $\mathrm{M}_1(x_1, y_1, z_1)$ and $\mathrm{M}_2(x_2, y_2, z_2)$ on the line. The line equations are then

$$\frac{x - x_2}{x_1 - x_2} = \frac{y - y_2}{y_1 - y_2} = \frac{z - z_2}{z_1 - z_2}. \tag{3.63}$$

From the basic line equations one can express $y$ and $z$ as functions of $x$ as

$$y = \frac{x - x_2}{x_1 - x_2}(y_1 - y_2) + y_2 \tag{3.64}$$

$$z = \frac{x - x_2}{x_1 - x_2}(z_1 - z_2) + z_2. \tag{3.65}$$

By having an ellipsoid and a line in 3D space there can only be three different cases of spatial ordering:

1) the line does not touch the ellipsoid;

2) the line touches the ellipsoid at only one point (tangent);

3) the line is passing through the ellipsoid (at two points).

To clearly see all three possibilities, we can input (3.64) and (3.65) into the equation of the ellipsoid. The result is a quadratic equation in $x$. Any quadratic equation can have zero, one or two solutions which correspond to the three different cases.

From the formulation of the problem, we are looking for the tangential solution. For a particular line, only one solution of the mentioned quadratic equation can exist. Knowing that the general solution of a quadratic equation $Ax^2+Bx+C=0$ is $x_{1,2} = \frac{-B\pm\sqrt{B^2-4AC}}{2A}$, with $A \neq 0$, the value of the expression under the square root must be equal to zero:

$$
\begin{aligned}
&a^2(x_1-x_2)^2\big((x_1-x_2)^2b^4 + \big((y_1^2-2y_2y_1+y_2^2+(z_1-z_2)^2\big)\\
&a^2 - x_2^2(y_1^2+z_1^2) + 2x_1x_2(y_1y_2+z_1z_2) - x_1^2(y_2^2+z_2^2)\big)b^2 - a^2(y_2z_1-y_1z_2)^2\big) = 0. \quad (3.66)
\end{aligned}
$$

To avoid division with zero we obtain the constraint:

$$\left(y_1^2 - 2y_2y_1 + y_2^2 + (z_1-z_2)^2\right)a^2 + b^2(x_1-x_2)^2 \neq 0.$$

To get the solution for $a$ and $b$ we need one more independent equation connecting $a$ and $b$. We can use the known relation between the focal length and the semi-major axes of an ellipsoid:

$$f^2 = a^2 - b^2. \qquad (3.67)$$

The problem of solving the system of (3.66) and (3.67) can be simplified by noticing that $a$ and $b$ appear in quadratic "portions". It is possible to introduce new variables equal to $a^2$ and $b^2$ to reduce our system to one linear and one quadratic equation. In total there will be two solutions for $a^2$ and two solutions for $b^2$. Since both $a$ and $b$ can take on only positive values there will also only be two solutions for $a$ and two solutions for $b$. After substituting (3.67) into (3.66), the solution for $a^2$ is found to be:

$$a_{1,2}^2 = \frac{A_1+A_2+A_3 \pm \sqrt{\left(B_1+B_2\right)^2 - B_3B_4}}{C_1}, \qquad (3.68)$$

where the variables $A_1$, $A_2$, $A_3$, $B_1$, $B_2$, $B_3$, $B_4$ and $C_1$ are the following polynomials:

$$\begin{aligned}
A_1 &= 2x_1^2f^2 + 2x_2^2f^2 + y_1^2f^2 + y_2^2f^2 + z_1^2f^2 + z_2^2f^2 - 4x_1x_2f^2 \\
A_2 &= -2y_1y_2f^2 - 2z_1z_2 + f^2 + x_2^2y_1^2 + x_1^2y_2^2 + x_2^2z_1^2 + y_2^2z_1^2 \\
A_3 &= x_1^2z_2^2 + y_1^2z_2^2 - 2x_1x_2y_1y_2 - 2x_1x_2z_1z_2 - 2y_1y_2z_1z_2 \\
B_1 &= \left(2x_1^2 - 4x_2x_1 + 2x_2^2 + y_1^2 + y_2^2 + z_1^2 + z_2^2 - 2y_1y_2 - 2z_1z_2\right) \cdot f^2 \\
B_2 &= x_1^2y_2^2 + y_2^2z_1^2 + x_1^2z_2^2 + y_1^2z_2^2 + x_2^2\left(y_1^2 + z_1^2\right) - 2y_1y_2z_1z_2 - 2x_1x_2(y_1y_2 + z_1z_2) \\
B_3 &= 4f^2\left(x_1^2 - 2x_2x_1 + x_2^2 + y_1^2 + y_2^2 + z_1^2 + z_2^2 - 2y_1y_2 - 2z_1z_2\right) \\
B_4 &= \left(y_2^2 + z_2^2\right)x_1^2 - 2x_2(y_1y_2 + z_1z_2)x_1 + f^2(x_1 - x_2)^2 + x_2^2\left(y_1^2 + z_1^2\right) \\
C_1 &= 2\left(x_1^2 - 2x_2x_1 + x_2^2 + y_1^2 + y_2^2 + z_1^2 + z_2^2 - 2y_1y_2 - 2z_1z_2\right)
\end{aligned}$$

Knowing $a$ it is straightforward to calculate $b$ from equation (3.67), and also the point where the center of the scattering occurred. Similar equations can be obtained by expressing $x$ and $z$ in terms of $y$.

There are a few additional constraints on the solution. The point of scattering must be in the line-of-sight with respect to the transmitter and the receiver, otherwise the path is blocked (in this case by the ground) and it can be assumed that the signal will be lost. Also, as mentioned above, one has to isolate the part of the trail where ionization occurred. This method is fast and reliable.

The main problem with the above algorithms is that they assume that the transmitter, the trail and the receiver are known, which in the general case is not true. In practice, the trail has to be determined by using the information that the reflection occurred due to the presence of a meteor trail. For a given transmitter-receiver pair there are multiple possibilities of detecting many different meteors resulting in the same observational data. In section 3.7 we will discuss how this problem can be resolved.

## 3.4 Probability of Detecting Meteors

To estimate probabilities of detecting meteors for a fixed TR pair we modified the analytical algorithm given to determine which possible meteor trails will be detected. The coordinates of the transmitter in geocentric geographic coordinates (longitude, latitude, altitude) are ($\lambda_T$, $\varphi_T$, $h_T$) while the coordinates of the receiver are ($\lambda_R$, $\varphi_R$, $h_R$). For simplicity we assume that both the transmitter and receiver are positioned at sea level, thus we can write $h_T = 0$ and $h_R = 0$. Having one point of the trail $\mathrm{M}_{1i}$ ($\lambda_{M1i}$, $\varphi_{M1i}$, 110 km) and a direction defined by the meteoroid's velocity vector, the trail is completely defined. The coordinate transformations needed to obtain canonical from geocentric coordinates are given in the appendix.

A uniform distribution of meteors over the sky is obtained by using a coordinate grid defined in the geocentric geographic coordinate system. The meteors are defined using two points, the first one at an altitude of 110 km with the coordinates ($\lambda_{M1}$, $\varphi_{M1}$, $h_{M1} = 110$km) and the second at an altitude of 80 km having coordinates ($\lambda_{M2}$, $\varphi_{M2}$, $h_{M2} = 80$ km). We created a rectangular zone in longitude-latitude space around the baseline TR such that longitude goes from $\lambda_{min}$ to $\lambda_{max}$ and latitude from $\varphi_{min}$ to $\varphi_{max}$. For each point $\mathrm{M}_{1i}$ with longitude and latitude in the given intervals, and at an altitude of 110 km $\mathrm{M}_{1i}$ ($\lambda_{M1i}$, $\varphi_{M1i}$, 110 km), it is possible to create a family of meteor lines using uniformly distributed direction vectors. A unity vector in spherical coordinates is defined using azimuthal $\phi$ and polar $\theta$ angles together with the unity radius. The azimuthal angle is in the range $[0,\ 2\pi)$ and the polar angle takes values in the interval $[0,\ \pi]$. Obtaining a set of uniformly distributed unity vectors over the surface of the unity sphere is not trivial. We loop over the polar angle uniformly, while the azimuth angle changes, taking into account the foreshortening due to the polar angle via

$$d\phi = \frac{d\phi_{const}}{\sin\theta}, \tag{3.69}$$

where $d\phi_{const}$ is some constant value representing the minimal increment. Knowing that

$\theta$ takes values from the interval $[0, \pi]$, there are two points where $d\phi$ does not have solutions, namely, where $\theta = 0$ and $\theta = \pi$. Physically, at the "bottom" and the "top" of the sphere the meaning of the azimuthal angle is not defined: there is only one "bottom" point with the polar angle $\theta = 0$. The same applies for the "top" point. Thus, the described algorithm provides the distribution of the points on the sphere such that the surface area between any four closest points is constant. An example of the distribution having 4613 points is given in Fig. 3.11.

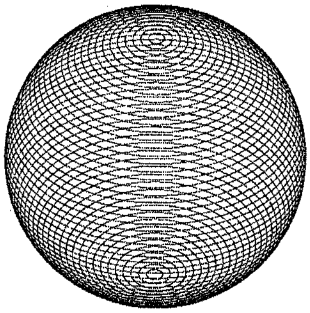

Figure 3.11: A uniform distribution of points over the surface of a sphere. The parameters used are $d\phi_{const} = \pi/30$ and $d\theta = \pi/30$.

Checking if the given meteor produces a forward-scattering reflection at the receiver point is done using equation (3.68). We limited the altitude of the reflection points to a range between 80 km and 110 km. It is important to notice that not all of the generated meteoric lines will intersect the Earth's atmosphere at an 80 km altitude. Only those meteoroids that do are taken into account. An example of meteoric lines entering the Earth's atmosphere at a point 110 km high is shown in Fig. 3.12. The antenna beam patterns are set to be uniform over the whole sky: i.e. the antennas are not directed. The 2ACSA discussed in the previous Chapter has a large main beam covering about 30% of the sky. Typical commercial transmitters are built in such a way as to provide maximal ground coverage, usually having main lobes pointed in the horizontal direction.

The number counts of detected meteors at each point of meteor origin, are shown in Fig. 3.13 (top). The coordinates of the transmitter are (279.66°, 39.30°, 0 km) and of

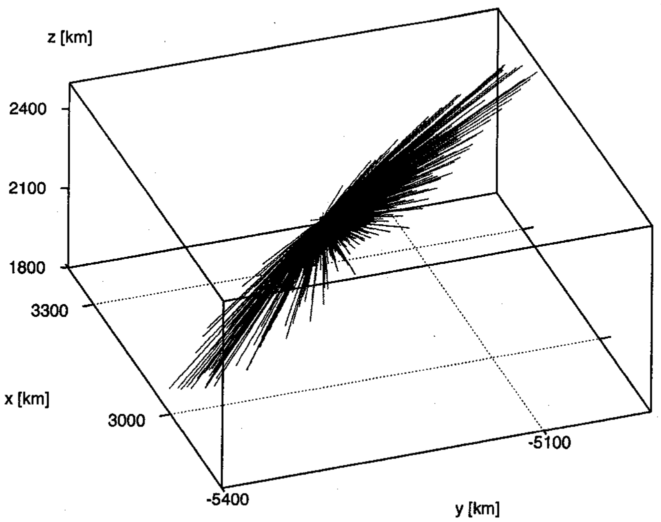

Figure 3.12: A distribution of meteors with the fixed point of entrance in the atmosphere at 110 km altitude. The second point for each meteor is at 80 km altitude. The parameters used are $d\phi_{const} = \pi/30$ and $d\theta = \pi/30$. The center of Earth is at the point (0,0,0).

the receiver (280.64°, 45.82°, 0 km). The distance TR is 729 km. In the plot there are clearly two visible regions with higher number count, located above the transmitter and above the receiver. The reader should note that these two regions are not showing the position of the scattering points, but just the position of the beginning of the trail. A plot containing the reflection points varies with altitude and will be dealt with shortly.

The collected power for the setup described above is shown in Fig. 3.13 (bottom). The power is normalized to the highest value. There is a significant difference in the shapes of the distributions plotted in the two plots in Fig. 3.13, especially above T and R. In these regions, the available configurations have angle $\beta$ close to 90°, minimizing the received power according to equation (3.56).

The higher the grid resolution, the larger number of meteors per grid point. The overall shapes of graphs shown in Fig. 3.13 are not changed much by increasing the simulation's resolution. The plots tend to become more symmetric. For more details see

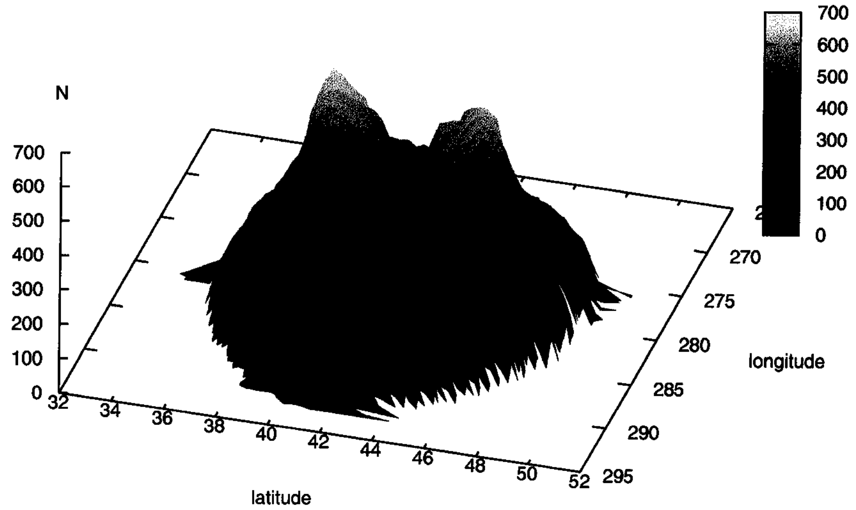

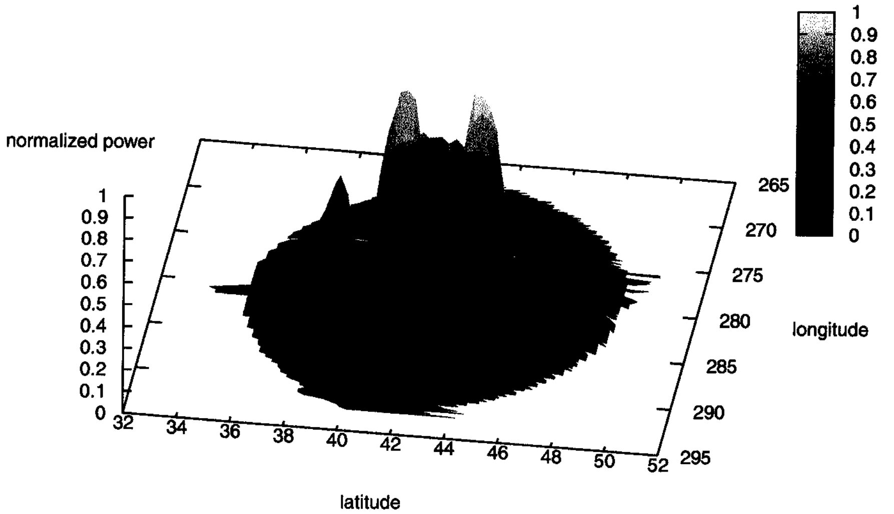

Figure 3.13: Top: a number distribution of the initial meteor points at an altitude of 110 km of the trails causing the forward-scattering reflections. Bottom: a detected power distribution per initial meteor points at an altitude of 110 km. The power is normalized to the highest value. Latitude and longitude are given in degrees. The geographic coordinates of the transmitter are (279.66°, 39.30°, 0.0 km) and of the receiver (280.64°, 45.82°, 0.0 km). The transmitter and the receiver antenna beams are set to be uniformly distributed over the whole sky.

Fig. 3.17. A more detailed computation also results in an increase of the $z$ scale: i.e. the highest peaks become even higher, while the low regions grow more slowly.

A second example is presented for a transmitter and a receiver separated by 395 km. The transmitter has geographic coordinates (275°, 45°, 0 km), while the receiver is located at (280°, 45°, 0 km). The resolution of the simulation is defined by the parameters $d\phi_{const} = \frac{\pi}{20}$, $d\theta = \frac{\pi}{20}$, and the longitude and the latitude increments of the entrance point are 0.1°. The distributions of the initial scattering points at the different altitudes are given in Fig. 3.14. To verify that the simulation resolution does not have

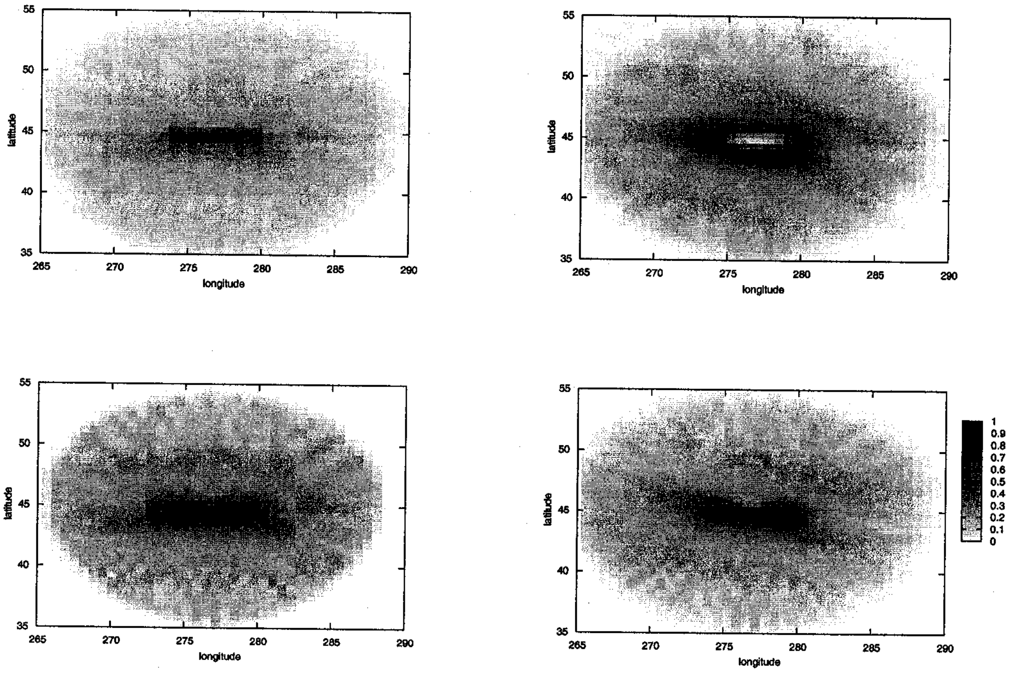

Figure 3.14: The number distribution of the initial meteor points at an altitude of 110 km (top left); the end points of the trails at an altitude of 80 km (top right); the scattering points at 90-95 km altitudes (bottom left); the scattering points at all altitudes (bottom right). The transmitter is set to be at the point with coordinates (275°, 45°, 0 km), and the receiver is at (280°, 45°, 0 km). Distance TR is 395 km. The other parameters used are $d\phi_{const} = \frac{\pi}{20}$ and $d\theta = \frac{\pi}{20}$.

much influence on the overall distribution, the results of the simulation are re-plotted in Fig. 3.15 with the parameters changed to $d\phi_{const} = \frac{\pi}{10}$ and $d\theta = \frac{\pi}{10}$. Similar results

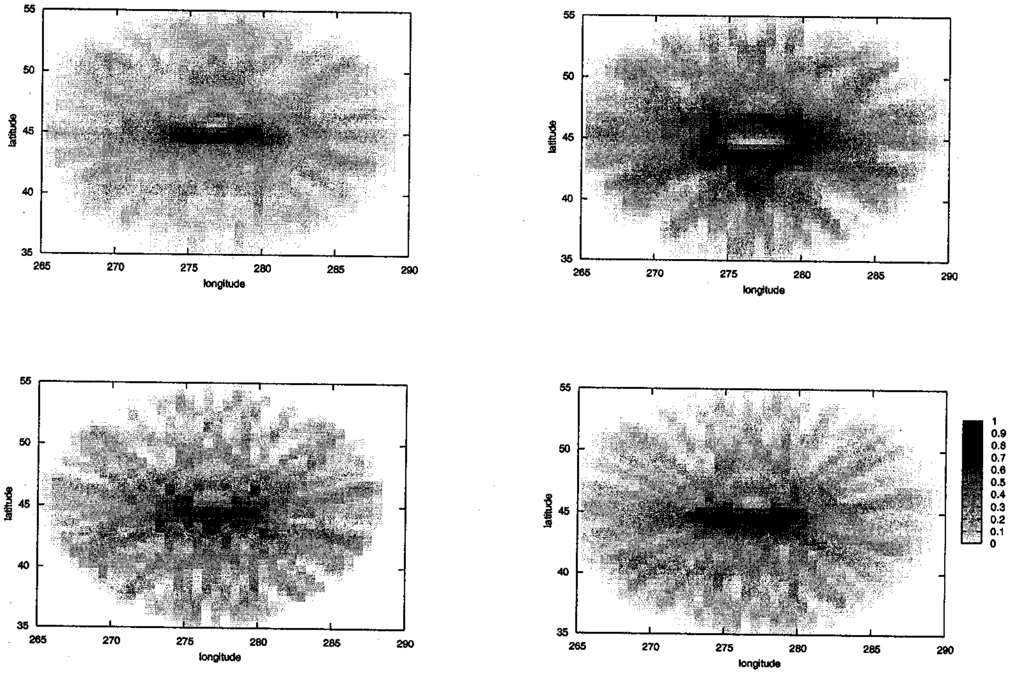

Figure 3.15: The number distribution of the initial meteor point at an altitude of 110 km (top left); the end points of the trails at an altitude of 80 km (top right); the scattering points at 90-95 km altitudes (bottom left); the scattering points at all altitudes (bottom right). The transmitter is set to be at the point with coordinates (275°, 45°, 0 km), and the receiver is at (280°, 45°, 0 km). Distance TR is 395 km. The other parameters used are $d\phi_{const} = \frac{\pi}{10}$ and $d\theta = \frac{\pi}{10}$.

are obtained by setting $d\phi_{const} = \frac{\pi}{75}$ and $d\theta = \frac{\pi}{75}$, and using longitude and latitude increments of 0.2°. A number distribution of detected trails per the initial meteor point at an altitude of 110 km as well as a number distribution for the end point of the trail at an altitude of 80 km are shown in Fig. 3.16.

In Fig. 3.17 the total number densities of forward-scatter echoes summed over all altitudes between 80 and 110 km are plotted for a transmitter-receiver distance of 1000

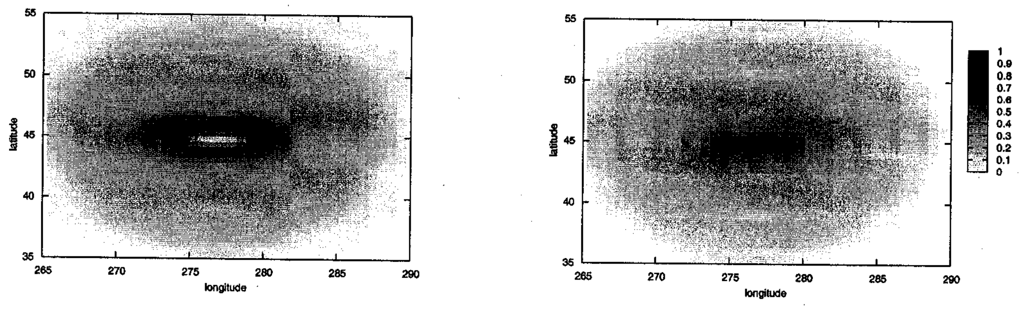

Figure 3.16: The number distribution of the end points of the trails at an altitude of 80 km (left); the scattering points at all altitudes (right). The parameters are $d\phi_{const} = \frac{\pi}{75}$ and $d\theta = \frac{\pi}{75}$. The longitude and the latitude increments are 0.2°.

km. The number of generated meteors per initial trail point was varied by changing the parameters $\phi$ and $\theta$. The results are dependent on the simulation resolution. It is expected that there should be a symmetry of the relative number density with respect to the line TR, as well as a symmetry with respect to the line perpendicularly bisecting TR. By increasing the resolution, the results become more symmetric.

An important conclusion is that the number of possible detections is highest in the localized zone around the baseline TR, excluding the baseline itself. Comparing the results of our simulation with the semi-numeric results presented in McKinley, 1961, [74] there is a small discrepancy. The relative number distributions in the region of the sky above the transmitter and the receiver are of the same order of magnitude as in the regions around the baseline.

The normalized power density of forward-scatter echoes projected onto the surface of the Earth for the 1000 km baseline is given in Fig. 3.18. The highest value of the detected power is clearly visible around the baseline, however there are also two secondary peaks which do not exist in the number density plot given in Fig 3.17.

The typical length of a meteor trail is about 10-40 km. In our simulations we checked how the number and power density plots were affected by increasing the maximal length

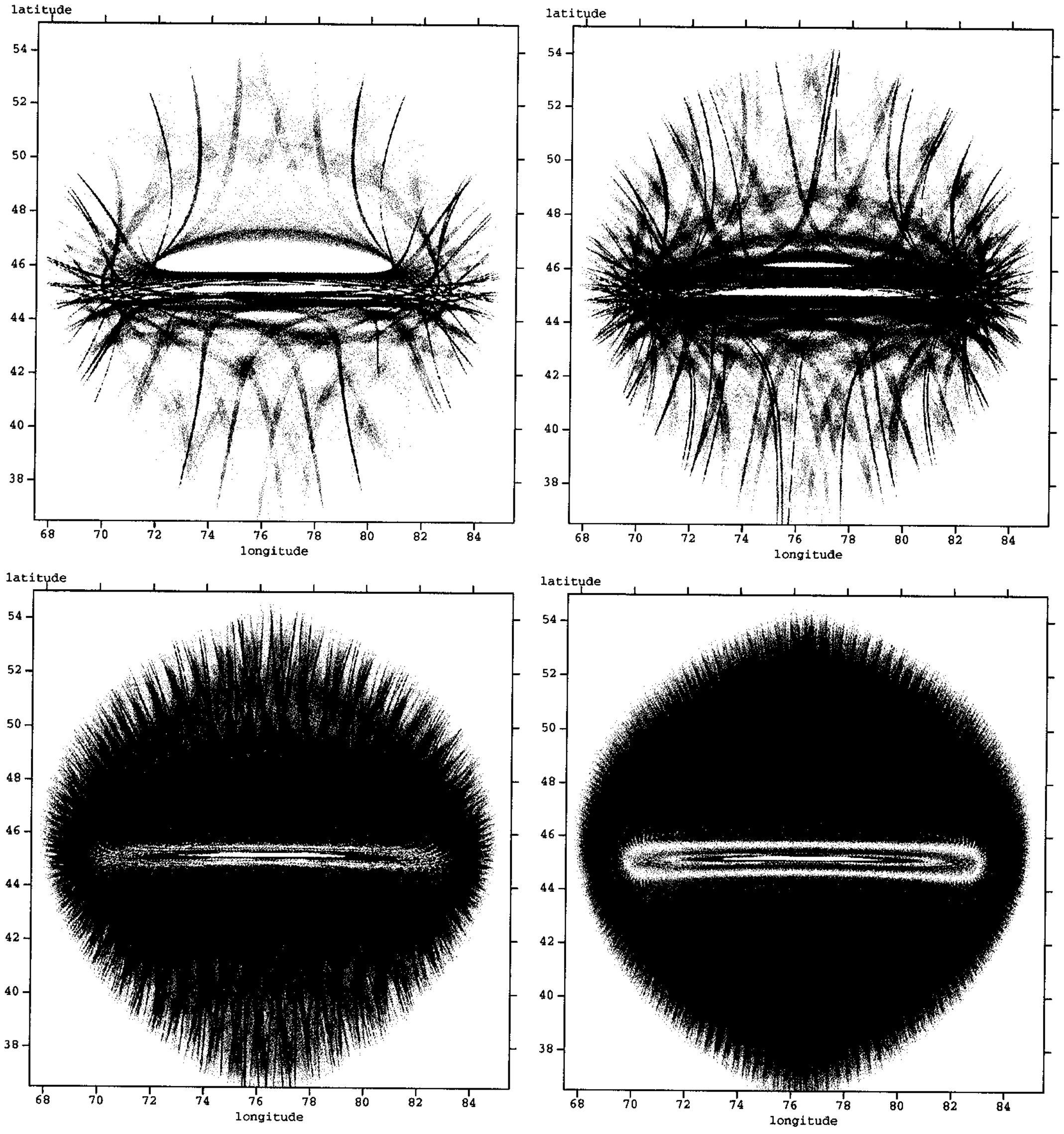

Figure 3.17: The number distribution of forward-scatter echoes. The transmitter has geocentric geographical coordinates (82.74°, 45.0°, 0 km), and the receiver's coordinates are (70.0°, 45.0°, 0 km). The distance TR is 1000 km. The longitude/latitude resolution is 1.2 arc minutes. The parameters $(d\phi_{const}, d\theta)$ are: top left $(\frac{\pi}{10}, \frac{\pi}{10})$; top right $(\frac{\pi}{15}, \frac{\pi}{15})$; bottom left $(\frac{\pi}{35}, \frac{\pi}{35})$; and bottom right $(\frac{\pi}{75}, \frac{\pi}{75})$.

of a trail from 40 km to 100 km, and found no change.

For every transmitter-receiver pair, the number distribution of scattering points for all possible meteors defines a type of instrumental profile of the given forward scattering

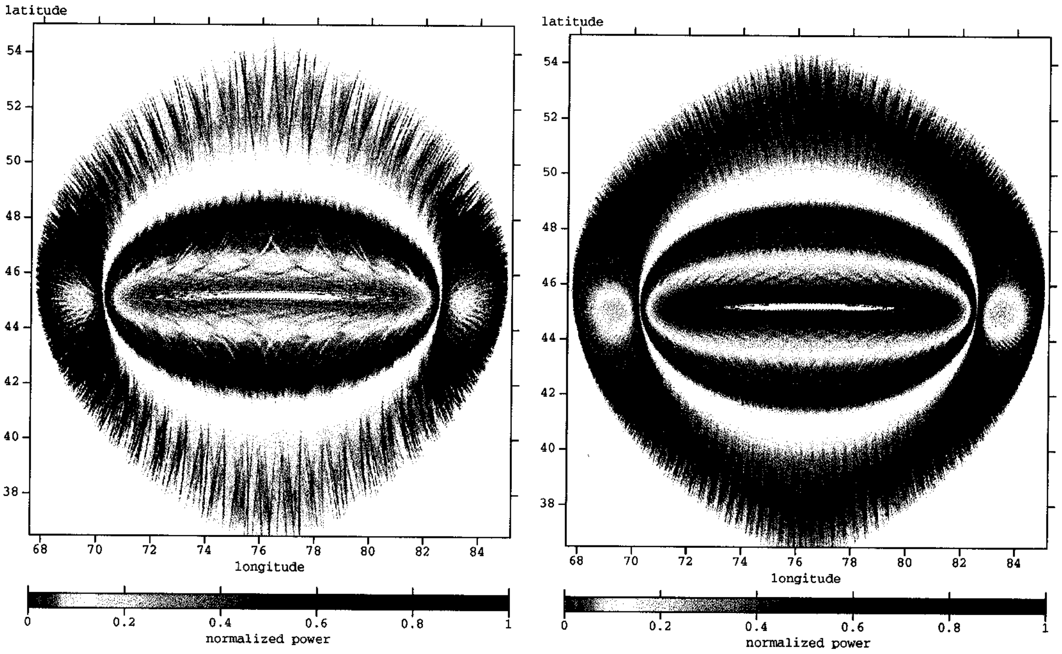

Figure 3.18: The normalized power distribution of the received forward-scatter echoes. All parameters are the same as in Fig. 3.17. Left: $d\phi_{const} = \frac{\pi}{35}$ and $d\theta = \frac{\pi}{35}$. Right: $d\phi_{const} = \frac{\pi}{75}$ and $d\theta = \frac{\pi}{75}$.

setup. The distribution will change depending on the baseline length and the antenna characteristics.

### Meteor Showers: Observable Trails

All meteors caused by a meteor shower appear to be originating from a fixed point on the celestial sphere (radiant). A simple approximative method to predict the scattering points of the observable meteor shower trails at a fixed height, for a fixed transmitter and receiver, is given in [42] and slightly modified in [144]. The theory of this simplified model is explained above, see equations (3.51 - 3.54).

In our simulations, the radiant is defined by setting the first meteor path point, $M_1$, with defined geocentric coordinates far from the Earth, i.e. at height $h_R = 10^{20}$ m. The second point describing the meteor path, $M_2$, is set to be at an altitude of 130 km. We

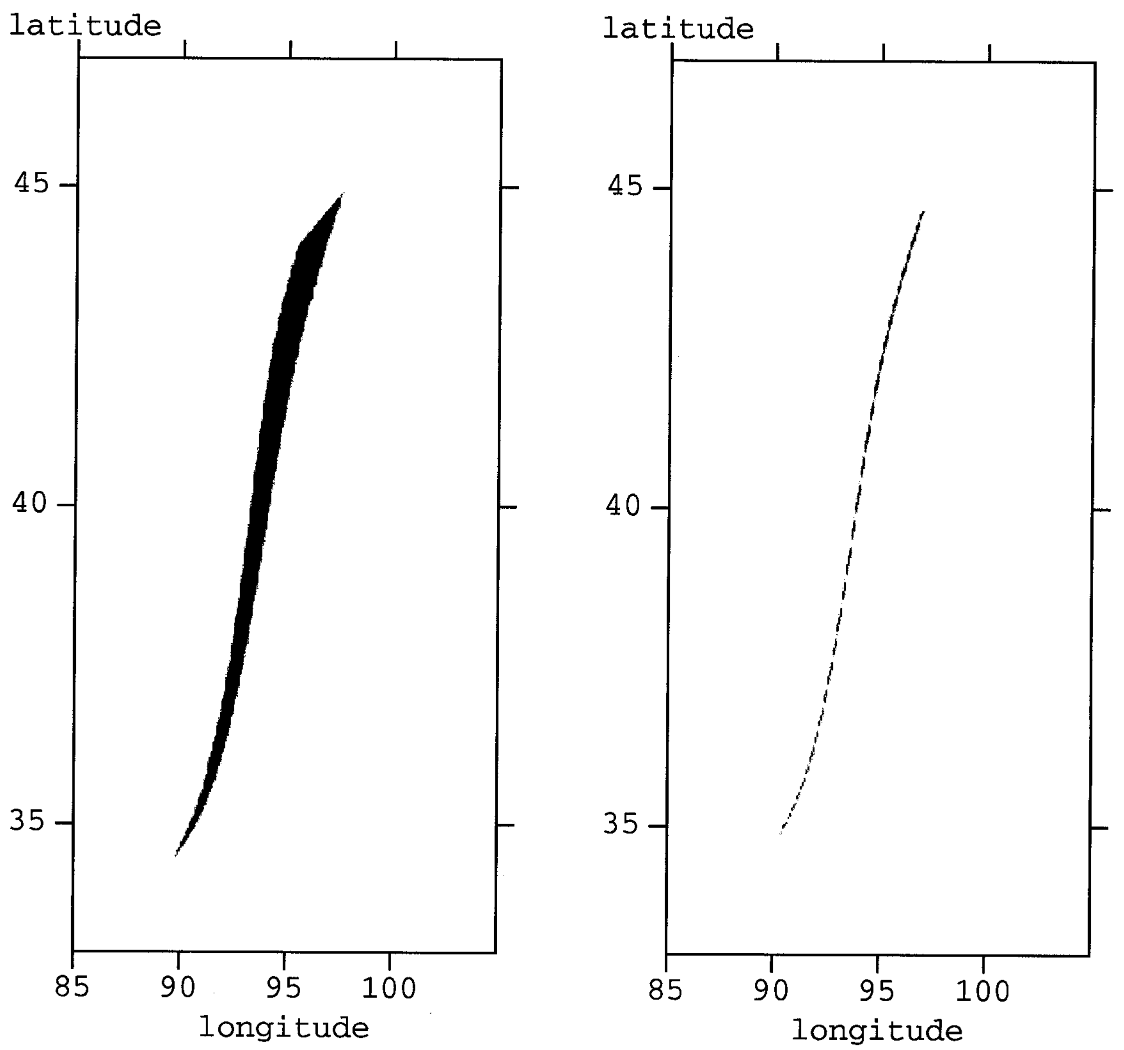

Figure 3.19: The observability function for a meteor shower with radiant at (60°, 30°, $10^{20}$ m). The transmitter coordinates are (90°, 36°, 0 km) and the receiver is located at (90°, 45°, 0 km) with TR distance 1000 km. The maximal length of the trails is 40 km. Left: the distribution of scattering points at all altitudes; Right: at 100 km altitude.

looped through all possible $M_2$ points and checked whether the meteoric line $M_1M_2$ is observable for the given T and R. The baseline T-R is set to be 1000 km in order to campare the results with those presented in [144], and with the observability function shown in Fig. 3.19. The plot on the right side corresponds to the scattering points at 100 km altitude. There is an excellent agreement with Fig. 3.8 and Fig. 6 from Verbeeck, 1996 [144].

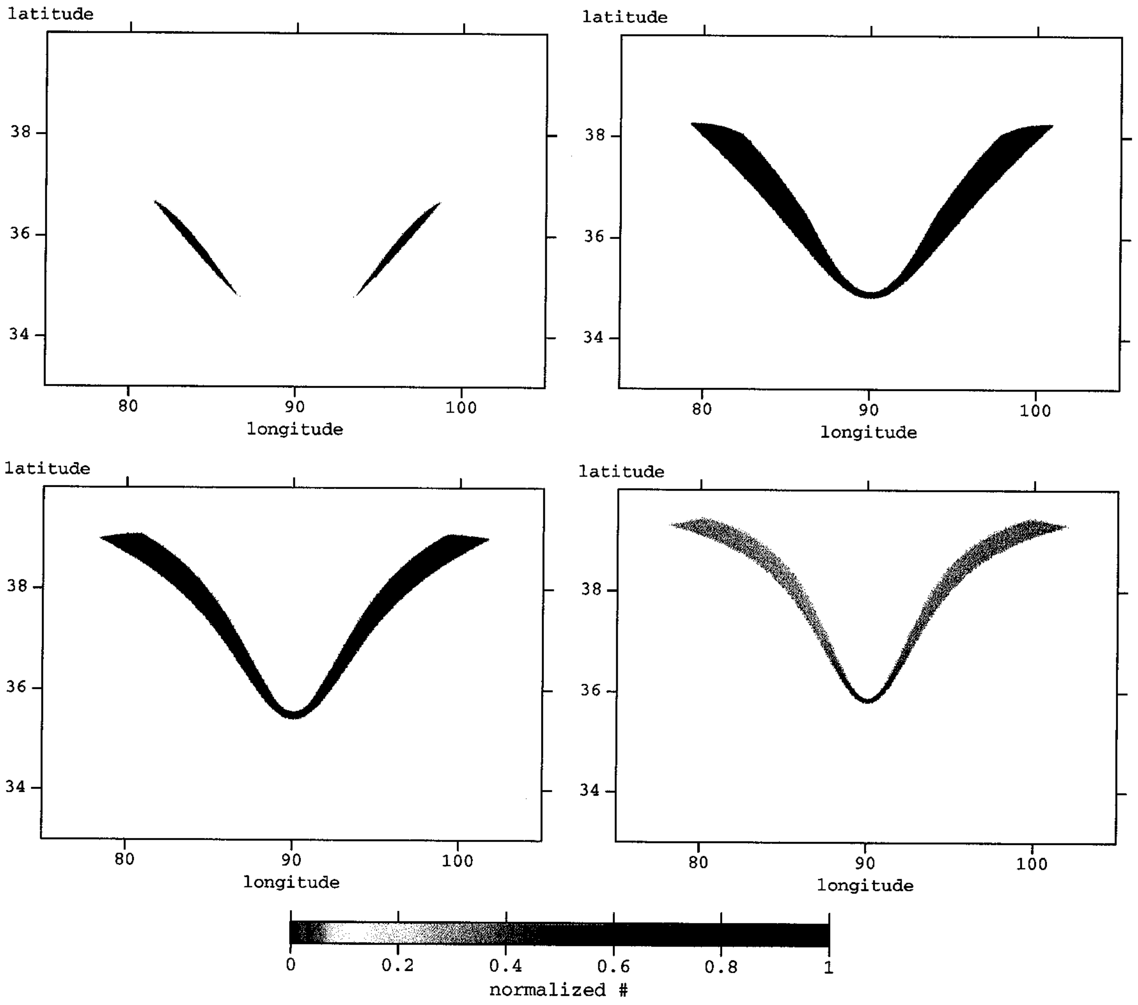

Figure 3.20: The observability functions for meteor showers with radiants in (90°, 36°, $10^{20}$ m) (top left), (90°, 30°, $10^{20}$ m) (top right), (90°, 20°, $10^{20}$ m) (bottom left) and (90°, 10°, $10^{20}$ m) (bottom right). The transmitter coordinates are (90°, 36°, 0 km), and the receiver is located at (90°, 45°, 0 km) with TR distance 1000 km. The maximal length of the trails is 40 km.

The observability function changes with the radiant position. Examples are given in Fig. 3.20. The radiants were set to be aligned with the TR baseline, driving the obvious left-right symmetry on all four shown plots. Obviously, by setting the radiant on the receiver's side, the plots would look identical, with the latitude reversed. Again, the plots are in agreement with [144], Fig. 4.

## 3.5 Illumination Footprint of Individual Meteor Trails

The term "illumination footprint" has roots in the theory of meteor burst communication. It is defined as the geographic region illuminated by a scattered signal from a single meteor. The footprint depends on the beginning, orientation and length of the trail. Basically, it defines the position of all possible receivers capable of receiving the signal emitted from the fixed transmitter and reflected by the given trail. Identifying the region of possible transmitters for a fixed receiver is in principle the same problem, due to symmetry of specular scattering.

A simple technique for calculating the ground illumination footprint of individual trails is discussed in the study done by Jay A. Weitzen in 1990 [149]. His approach is to use Rudie's equation (3.62) to calculate only whether a certain point on flat ground can receive a signal reflected by a given trail. His results are incomplete compared to the data produced using the method discussed here. The two main constraints of Weitzen's technique are the weakness of using Rudie's equation, as discussed in the previous section, and the approximation that the Earth's surface is flat.

The simulation described earlier was used to predict illumination footprints for a fixed receiver positioned at a site with geographic coordinates (90°, 45°, 0 km). The antenna beam of the receiver was uniformly spread over the whole sky. The meteor trails start forming at the point where the meteoroids enter the atmosphere, for example (80.5°, 45°, 110 km). The trail length was limited to 40 km. Four illumination footprints are given in Fig. 3.21 for four different orientations of the trail.

The importance of meteor footprints is that for a fixed receiver a single meteor can reflect only radio waves coming from transmitters in a fixed zone of the Earth's surface. If transmitters are "nicely" spatially distributed, and if one can resolve between different

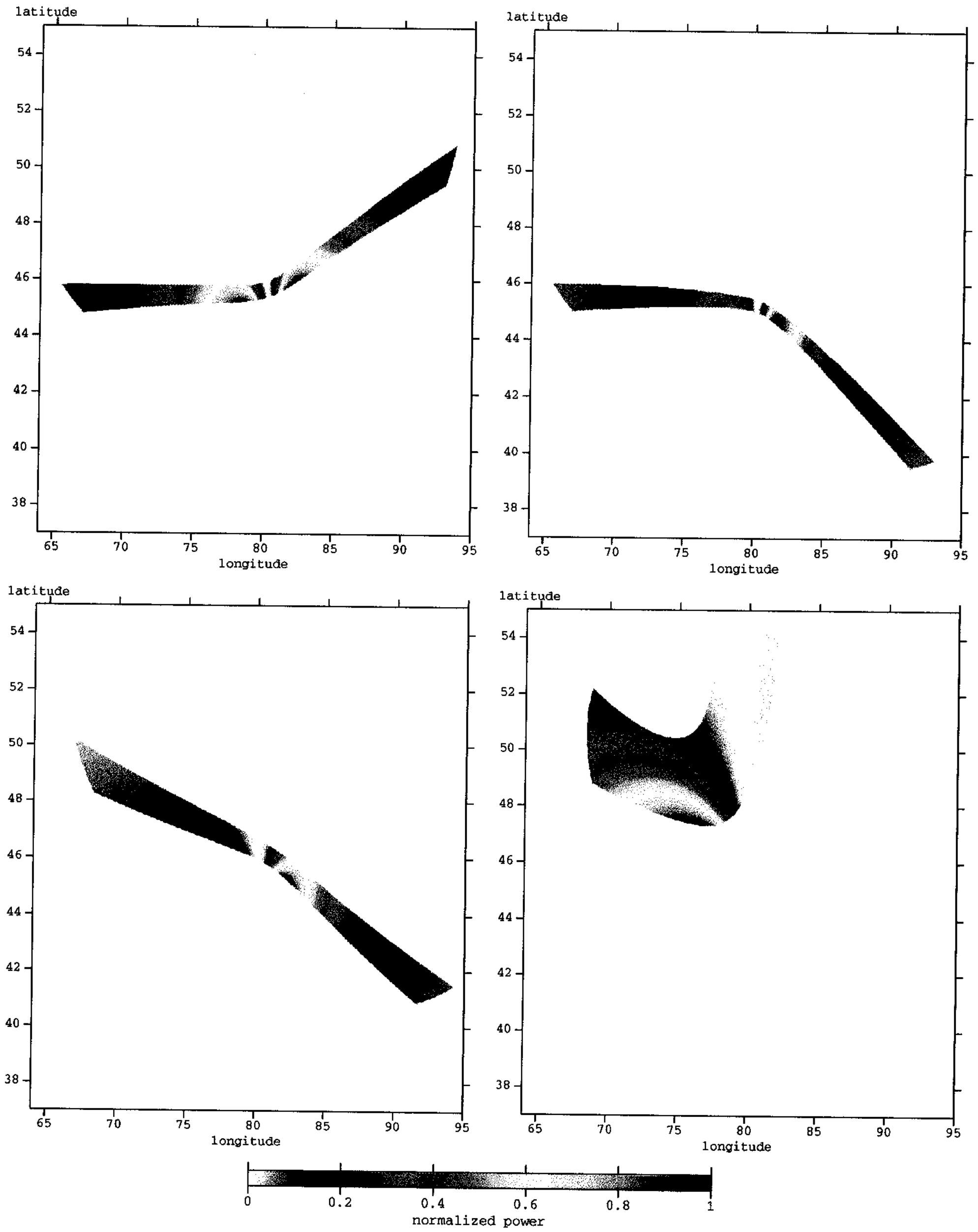

Figure 3.21: The ground illumination footprints for a family of meteors entering the atmosphere at a single point with coordinates (80.5°, 45°, 110 km). The transmitter coordinates are (90°, 45°, 0 km). The maximal length of the trails is 40 km. The orientation of the trails is: Top left $\phi = 60°$; Top right $\phi = 150°$; Bottom left $\phi = 240°$; Bottom right $\phi = 330°$; and $\theta = 20°$.

transmitters, it is possible to define a meteoroid line even without using time delay information.

## 3.6 Observations at a Single Frequency

Most observers using standard single frequency forward-scattering methods are using the data only to count meteors (flux estimates). There are statistical methods of eliminating a certain number of sporadic meteors in order to estimate the number of meteors in a given shower. Oleg Belkovich's group from the Kazan Observatory, Russia, has been applying a statistical method for estimating the meteor flux of a particular shower using data collected in the last few decades [4].

An interesting attempt to approximately calculate the height of the scattering point in forward-scattering observations is described in [12]. In the case of overdense trails with total reflection (overdense type I), a simple relation between the attenuation and the position of a receiver and a transmitter is used to estimate the height $h$ of the scattering point:

$$h \approx \frac{L}{2}\left(\frac{1}{\tan\phi} - \frac{L}{4R_E}\right). \tag{3.70}$$

Here $L$ is the distance between the receiver and the transmitter, $R_E$ is the radius of the Earth, and the angle $\phi$ is defined by:

$$a = \frac{-17.36}{\cos\phi}, \tag{3.71}$$

where $a$ is the attenuation, given in dB, of the incident to the reflected wave with electric fields $\mathbf{E}_i$ and $\mathbf{E}_r$

$$a = 10\log\frac{|\mathbf{E}_i|^2}{|\mathbf{E}_r|^2}. \tag{3.72}$$

Carbognani et al, 2000 used the received signal amplitude in volts to calculate the attenuation $a = 20\log V_R - 2$[dB].

In our observations, we can distinguish between overdense and underdense meteors by observing the time evolution of the signal as shown in Fig. 3.3. If the location of the transmitter is known, then overdense type I trails could be used for testing the above height determination method.

## 3.7 Broadband Observations

Single frequency observations of meteor forward-scattering cannot be used to determine the true position of the scattering point, nor the orbit of the meteoric body. Having only information about when the scattering occurred and the time evolution of the scattered signal is not enough for a serious geometrical analysis.

As discussed above, for a certain class of trails it is possible to calculate the height of the scattering zone. There are a few attempts to build an interferometric system capable of isolating a scattering zone. One such system is currently being developed at the Kochi University of Technology, Japan by Masa-Yuki Yamamoto [155]. Our approach is to use a single receiver capable of recording a single meteor trail using waves from spatially separated transmitters emitting at various frequencies. The data obtained contain intensity and time information for one meteor at a few different frequencies, including the time lag between the first reception at one of the frequencies compared to the time when the signal is detected at the other frequencies. This setup is similar to a radar system of Peter Browns's group at the University of Western Ontario, Canada, which uses multiple receivers and a single transmitter [148]

Having more transmitters makes the geometry of the problem significantly more complex. In the case of multiple transmitters, instead of having only one baseline T-R forming a single ellipsoid, there are multiple baselines $T_i$-R, $i = 1, \ldots N_T$, where $N_T$ is the total number of transmitters. Each baseline defines a family of ellipsoids. The equation of an ellipsoid with foci at any two points of 3D space in the general case is a second order polynomial in 3 coordinates. $N_T$ transmitter-receiver pairs would then give $N_T$ equations for ellipsoid families, since there is one ellipsoid defining coherent scattering for each detected reflection. In principle, it might be possible to form a system of equations with a unique solution defining the trail tangential to one ellipsoid per $T_i$-R family; however, such a problem is hard to solve.

The simplest approach is to pass through all possible radiants and investigate whether for each of the possible transmitters, there is a reflection. Assuming that the observed meteor trail is detected at $N_f$ different frequencies, we isolate all transmitters in a range of 2400 km around the receiver emiting at these $N_f$ frequencies. In the next step we look for the radiants and a set of transmitters capable of causing detection at all $N_f$ frequencies. Finally, the time of receiving a successful reflection is used to isolate the true radiant and obtain the velocity of the meteoroid. In Fig. 3.22, we show four different parameters in the case of detecting a fixed meteor trail at a fixed receiver for all possible transmitters. The main weakness of this method is computation time. A single check whether a reflection occurred for a given transmitter-receiver pair takes $10^{-7}$ s with a top of the line processor. In the case of 10000 transmitters, the computation time is on the order of $10^{-3}$ seconds. Searching through all possible meteors with 100 meter resolution over 1000 square kilometers at an altitude of 140 km will take over 300 thousand years. Computationaly, this is a very hard problem even for the fastest supercomputers.

### 3.7.1 Detecting Aircraft With TREX

A possible future application is using a digital spectrometer as an early warning radar. The typical height range for military aircraft is up to 18 km. An aircraft should produce forward-scattered signals. Such an air defense instrument is completely passive and cannot be targeted by high-speed antiradiation missiles. The commercial transmitters currently used for forward-scattering are not valid military targets and even if destroyed can be easily remounted. Transmitter power can be on the order of 10 watts, which can be produced by small solar generators. The cellular telephone transmitter network is another possible type of transmitter that could be used for military purposes, but in this

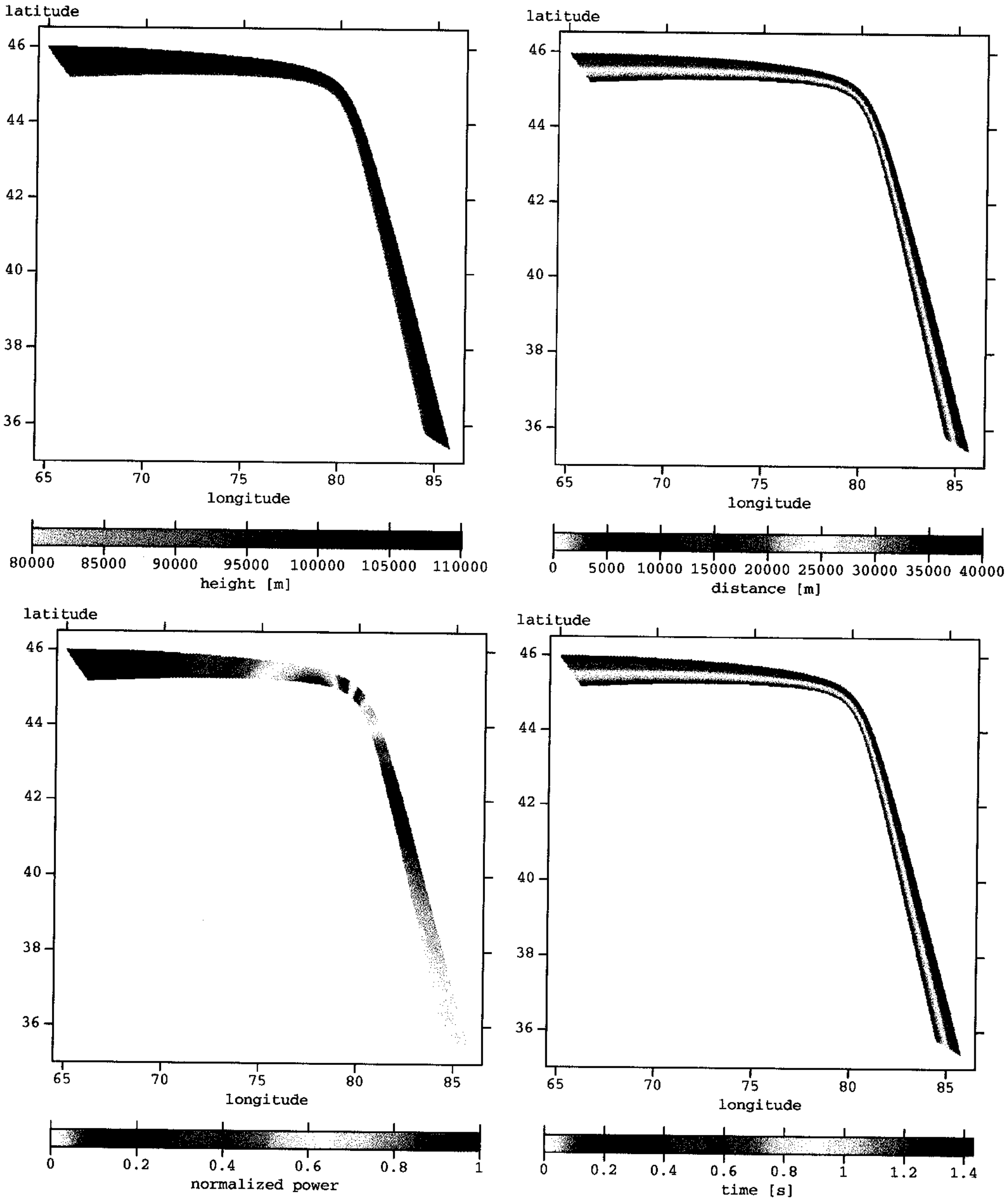

Figure 3.22: Four parameters of successful detections for different positions of transmitters for a fixed meteoroid with the initial point of the trail (80°, 45°, 110 km) and a receiver at (90°, 45°, 0 km). The total length of the trail is limited to 40 km. The parameters are: height of the scattering point (top left), distance from the beginning of the ionized trail (top right), normalized power (bottom left) and time of detection measured starting with the time of the first detection (bottom right).

case, the receiver would need to be reconfigured to work in gigahertz bands.

### 3.7.2 Search for the Orbit: Optimization via Simulated Annealing

We define the problem of determining an orbit of a meteoroid as: for a given set of observed forward-scattered signals transmitted by a set of $N_T$ transmitters and received by a receiver at all FM frequencies, find the most probable orbit of the responsible meteoroid. The observed data are given as the measured intensity $I_f(t)$ at a particular frequency $f$ at time $t$. Examples of $I_f(t)$ are given in the next chapter.

The optimization testing function in the general case must depend on the intensity $I_f(t)$. However, we will use only the information for when the first peak occurred at each frequency for the given meteor trail. The measured spectra intensity includes transmitter antenna parameters which, for most of the transmitters, cannot be extracted from the publicly open databases [130], [140]. In addition, the detected power depends on the polarization angle, which is also an unknown quantity. Above, we showed the geometry of a typical forward-scattering system and introduced the simplest models for predicting the received power for a transmitter-meteor trail-receiver system.

The search problem will be described as an optimization problem over 7 dimensional parameter space. To describe a meteor line we need 4 parameters: radiant position (2) and a single point at the fixed altitude (2). The velocity of the meteoroid is the fifth parameter. When all five of these parameters are known, coordinates of scattering points, if any, can be calculated from (3.68). For a single meteoric line and $N_T$ transmitters, there can be a maximum of $N_T$ scattering points spread over an infinite distance (see Fig. 3.23). The first constraints are the maximal and minimal altitude where the trail can be formed. We also assume the ionized region can be up to 40 km long. Thus, there is a need for a 6th and 7th parameter which describe the altitude where the ionized trail started forming and the altitude where the ionized portion ended.

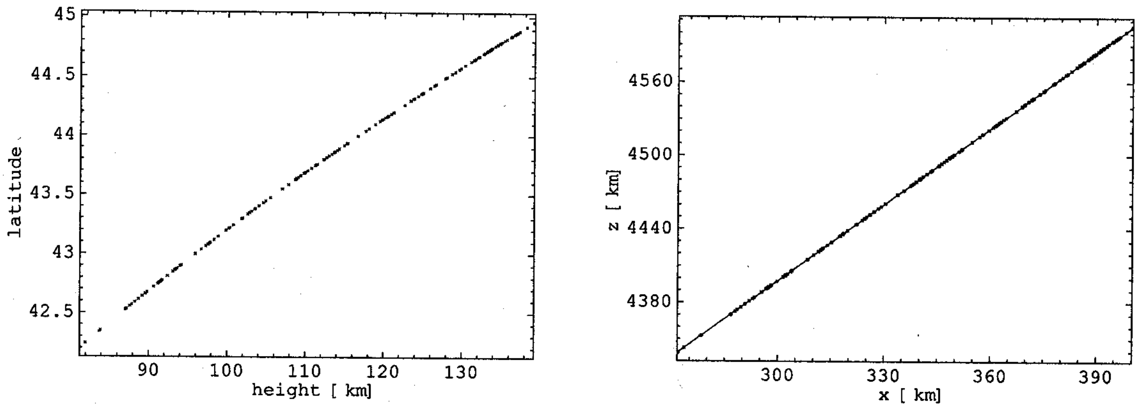

Figure 3.23: Possible scattering points are spread along a path of a meteoroid: latitude vs height (left) and rectangular geographic coordinates $z$ vs $x$ (right). The total length from the first to the last scattering point is 198.7 km.

We define the optimization function as

$$E = \min \sum_{f} [t(f,\ i) - t_0(f)]^2 , \tag{3.73}$$

where $i$ goes from 0 to the number of scattering points for a given line. The time of the first detected peak at the frequency $f$ is $t_0(f)$, defined to be zero for the first peak. $t(f,\ i)$ is the current state time of the first peak at the frequency $f$ normalized at the $i$–th scattering point. The variation of the optimization function given by (3.73) with velocity for a fixed line corresponding to a mock observation of forward scattering is shown in Fig. 3.24. The minimum of $E$ corresponds to the true velocity of the mock observed meteoroid. The function is continuous with only one minima.

The shape of the optimization function becomes much more complex when other parameters are taken into account. In Fig. 3.25 the optimization function is calculated for the latitude of a point at an altitude of 80 km. The radiant, speed and longitude of the point at 80 km altitude are fixed.

In Fig. 3.26, the optimization function is plotted for the points of the orbit at an altitude of 140 km for a receiver positioned at the Algonquin Radio Observatory. We used the full North American FM broadcasting database to compose a full list of transmitters.

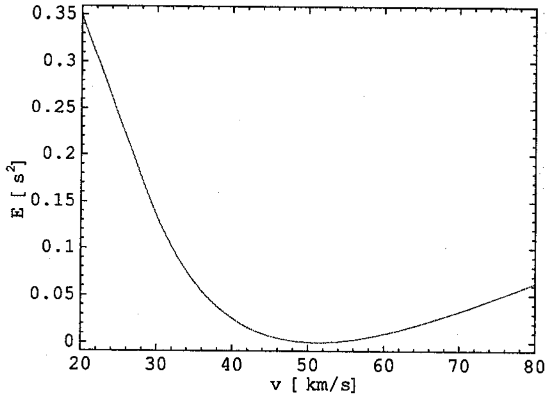

Figure 3.24: Optimization function $E$ versus velocity $v$ for a fixed trail. The correct value for the speed is 51.23 km/s.

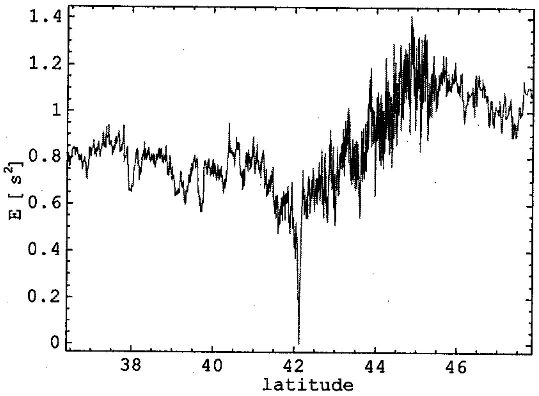

Figure 3.25: Optimization function $E$ versus latitude of a point at an altitude of 80 km. All other meteor parameters are fixed. The correct value is 42°.12827.

The direction of meteor velocity was kept fixed with the angles $\phi = 40°$ and $\theta = 55°$. The mock observation needed to define $t_0(f)$ is obtained for a 40 km/s meteoroid which started forming its ionized trail at (275°, 45°, 140 km). The total length of the mock trail was set to 8 km. There are multiple local minimums of the optimization function visible in the graph. When looking for a global solution, standard $N$-dimensional search methods such as the simplex method do not work well under such assumptions [96]. Searching through the full parameter space with the needed resolution could take thousands of years with computers at the present technological level.

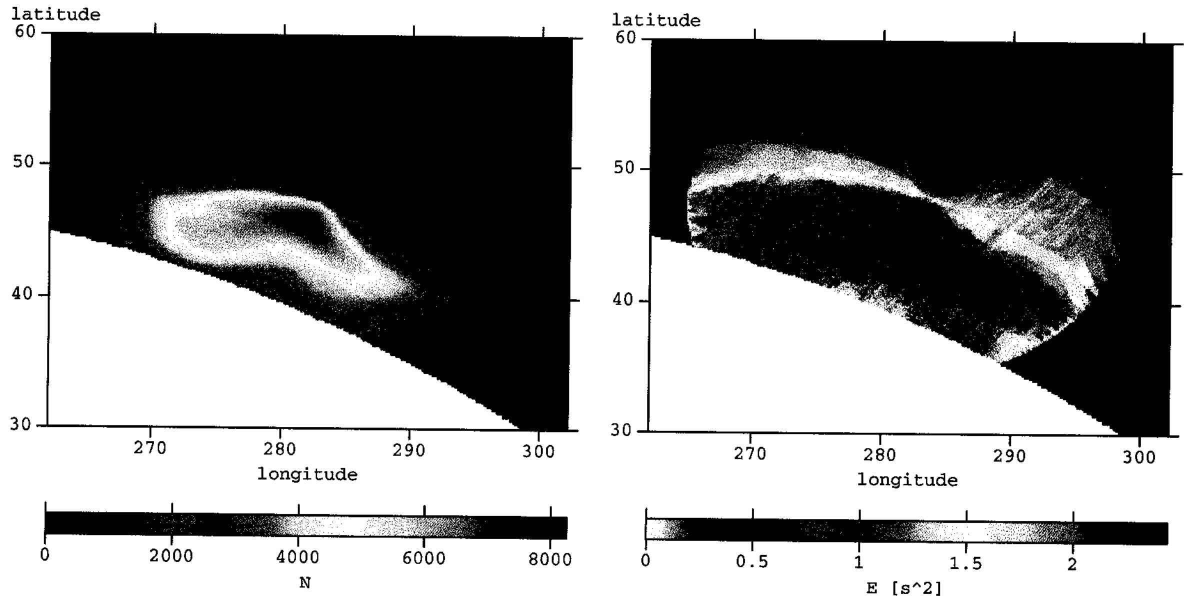

Figure 3.26: The number of scattering points $N$ (left) and the optimization function $E$ (right) at the points of orbit at an altitude of 140 km. All meteoroids are coming from a fixed radiant defined with the angles $\phi = 40°$ and $\theta = 55°$. The receiver is located at the Algonquin Radio Observatory (281°.967, 45°.97, 0.2 km) and transmitters are all North American FM towers. The meteoric lines passing through the points at the left bottom white portions of both images do not intersect the atmosphere at 80 km. The mock measurement is defined by a trail with a starting point at (275°, 45°, 140 km) and speed of 40 km/s.

We propose to use the simulated annealing method in our search for a meteor trail satisfying the observed data. Simulated annealing is an optimization algorithm based on a procedure of controlled heating and cooling of metals in order to reduce the defects of crystal structures [60]. The cooling of a system starts at an initial state where the system at high temperature is highly disorganized. Thereafter, the system slowly evolves toward a more ordered configuration, approaching the ground state with zero temperature. The evolution of the system can go toward a state with higher energy which opens the possibility of avoiding local minima. The method is defined by knowing the energy function

$E$ and by choosing the annealing schedule: the initial temperature $T_0$, the number of iterations for each temperature value, and the rate of cooling. In the general case for a finite problem, simulated annealing will successfully complete the optimization. However, sometimes the time needed to obtain the solution will exceed the time needed to search through the whole parameter space.

The transition from the state with energy $E_1$ of the system into another neighboring state with energy $E_2$ is defined by the probability

$$p = e^{\frac{-(E_2 - E_1)}{kT}},$$

where $k$ is a constant, equivalent to Boltzman's constant for thermodynamic systems. If the energy of the new state is lower than the energy of the first state, the system will move into the new state, otherwise there is a probability $p$ of the transition into the new state.

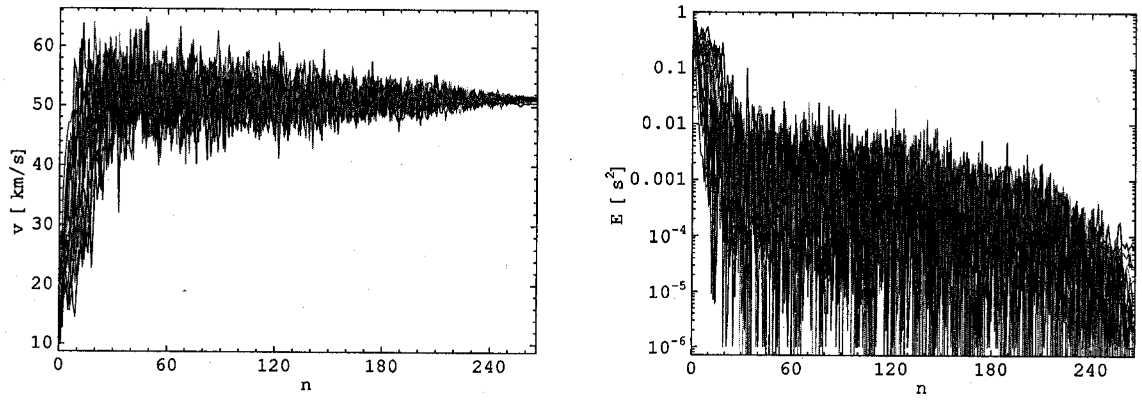

Figure 3.27: Velocity $v$ (left) and optimization function $E_2$ (right) vs number $n$ of probed velocities for a fixed trail. A total of 20 runs were plotted. Each search started with $v_0 = 20$ km/s, $T_0 = 4000$, $dT = 15$, $k = 10^{-7}$. The correct velocity is 51.23 km/s.

A quick test of simulated annealing applied to our problem is done by fixing a meteor line and doing a search for the minimal $E$ over velocity space. Every neighboring state is chosen randomly from a Gaussian distribution with a median set in the previous best solution and a standard deviation depending on $T/T0$. The calculations are done for the example given in plot 3.24. The results of 20 runs are shown in Fig. 3.27.

# Chapter 4

# Observations

This chapter provides a short description of the observations performed in the periods of April 19-24 and June 28 - July 18, 2006 at the Algonquin Radio Telescope site. The main goal of the first observational run was to test the equipment, to estimate the pollution of the VHF part of the spectrum, and to quantify the meteor echoes. The second run was performed in order to collect information on meteor activity and to detect the number of meteor trails visible at multiple frequencies. The data obtained can be used in the future to test our method of determining meteoroid orbital parameters using a single receiver.

## 4.1 April 19-26, 2006

The first forward-scattering observations were performed between April 19-26, 2006 at the Algonquin Radio Observatory. The exact coordinates of the receiver's antenna were (78°4′.22 W, 45°57′.33 N, 226 m). On April 23rd, 2006 the observation site was visited and the equipment was inspected for possible problems due to strong winds. None were found. The Algonquin Radio Observatory does not have a weather station, and the nearest ones are in Petawawa and North Bay. The weather conditions in Petawawa for the given dates are given in table 4.1 [154]. In total, 300 GB of data were collected. The acquisition algorithm was set to collect 80 times $2^{21}$ samples with a 500 MHz A/DC,

| Date | $T$ (°C) | $T_{max}$ (°C) | $H$ | $v_w$ ($\frac{\text{km}}{\text{h}}$) | Clouds | Rain |
|---|---|---|---|---|---|---|
| Apr 19 | 12 | 23 | 47 | 22 | Clear | |
| Apr 20 | 12 | 23 | 36 | 11 | Clear, Partly | |
| Apr 21 | 11 | 18 | 45 | 17 | Clear, Partly, Mostly | |
| Apr 22 | 8 | 11 | 75 | 33 | Clear, Overcast | Light |
| Apr 23 | 6 | 7 | 99 | 17 | Overcast | Light-Heavy |
| Apr 24 | 7 | 9 | 100 | 9 | Overcast | Light-Heavy |
| Apr 25 | 2 | 7 | 80 | 37 | Clear, Overcast | Rain, Light Snow |

Table 4.1: Weather report for Petawawa, Ontario (46.0°N, 77.3°W, 130m) for the time period Apr 19-25, 2006. $T$ is the average daily temperature, $H$ is the humidity index and $v_w$ is the maximal wind speed for the given date. Note: The weather report for North Bay (46.3°N, 79.4°W, 371 m) for the same time interval is very similar.

to perform $2^{15}$-point FFT and to record power spectra as fits format files. Strong FM lines were detected at 92.5 MHz, 96.7 MHz and 99.7 MHz, corresponding to local radio stations.

### 4.1.1 Milky Way

TREX in principle can provide an excellent tool for measuring the spectrum of the Galaxy if some challenges could be overcome. The signal measured by TREX is dominated by the Galactic synchrotron emission. The spectrum measured with our antenna having the Galaxy pass directly over the beam is shown in Fig. 4.1 (bottom). It is obtained with the 50-200 MHz bandpass filter with the resonant frequency in FM band. The cutoff and the resonant frequencies due to filter characteristics can be identified in the spectrum. The lines in the spectrum are due to terrestrial emiters (FM, TV and communication channels). The 21 cm signature detection requires removal of all sources of noise with precision of 5 orders of magnitude smaller than the Galactic signal. The main difficulties when estimating Galactic emission with TREX type of instrument are due to bandpass calibration, and because of changes of the antenna beam with frequency. The system noise and the filter function can be estimated using the thermal noise of a resistor. If the receiver input is terminated with a resistor, the voltage through the resistor will be proportional to the square root of temperature. Changing the temperature, the characteristics of the receiver including filters and amplifiers can be found. The calibration of the antenna could be done with comparing observations for at least three sources. For

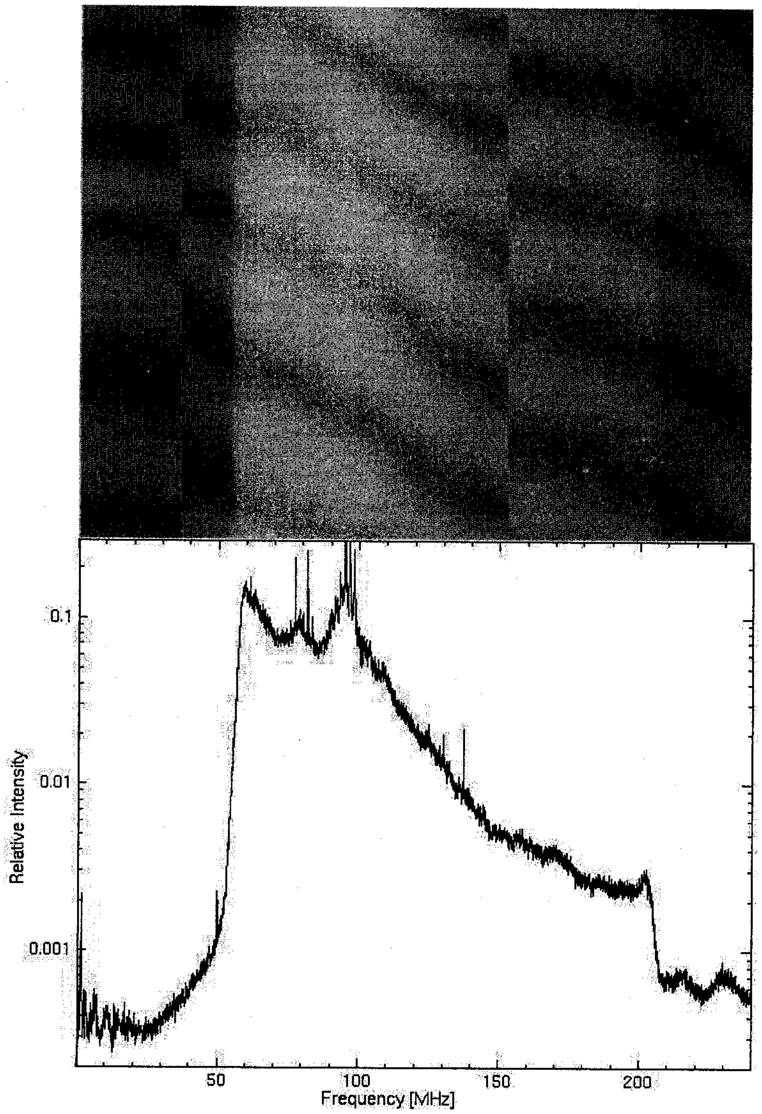

Figure 4.1: The power law growth of the Galactic "noise" toward the lower frequencies (bottom). The intensity is normalized to the highest peak for the given data set. Top: the time evolution of the spectra, showing the stabilty of the instrument, with the time resolution of one data set per second.

a small antenna system, the obvious choices would be Galaxy over the beam, Galaxy bellow the beam and the sun (maybe even Jupiter) over the beam. Differences between these spectra can be used to calibrate the instrument and find a true spectrum of the Galaxy.

The oscillations of the noise level due to the influence of our Galaxy at two different frequencies are shown in Fig. 4.2. The maximal signal is received at the moment when the Milky Way is passing over the antenna beam as plotted in Fig. 4.3. There are significant differences between the diurnal variations of the Galactic noise at 102.1 MHz and 105.1 MHz, shown in Fig. 4.2. Such discrepancies make observations of the 21 cm reionization step very hard. As explained in Chapter 1, the method for detecting the epoch of reionization, using TREX or any other small antenna telescope, requires stability in the level of the Galactic noise on the order of less than 0.01 percent (see Fig. 1.5). The only solution is to find and remove the source of the discrepancy. The possible causes of this problem are either the nature of the hardware, or ionospheric activity. In the first case, it might be that the antenna beam patterns are more frequency dependent than thought, or that there is some impedance matching problem. In principle, the hardware problem can be located by intensive testing and eventually corrected. In the second case, if the problem is in the ionospheric processes, then more observations and better understanding of ionospheric physics might eventually lead to a model to remove the effects.

### 4.1.2 Lyrids

The Lyrid meteor shower was active from April 16-25, 2006, with its maximum on April 22, 2006 at 16h30m UT ($\lambda = 32^\circ\ 32'$) [72]. A typical meteor of this shower has velocity $v = 49$ km/s, and the radiant has equatorial coordinates $\alpha_R = 271^\circ$, $\delta_R = 34^\circ$ (constellation Lyra). In the year 1803, a Lyrid meteor storm with $\sim 700$ meteors per hour was observed over the eastern US. Ever since, the maximal hourly rate of visual meteors has

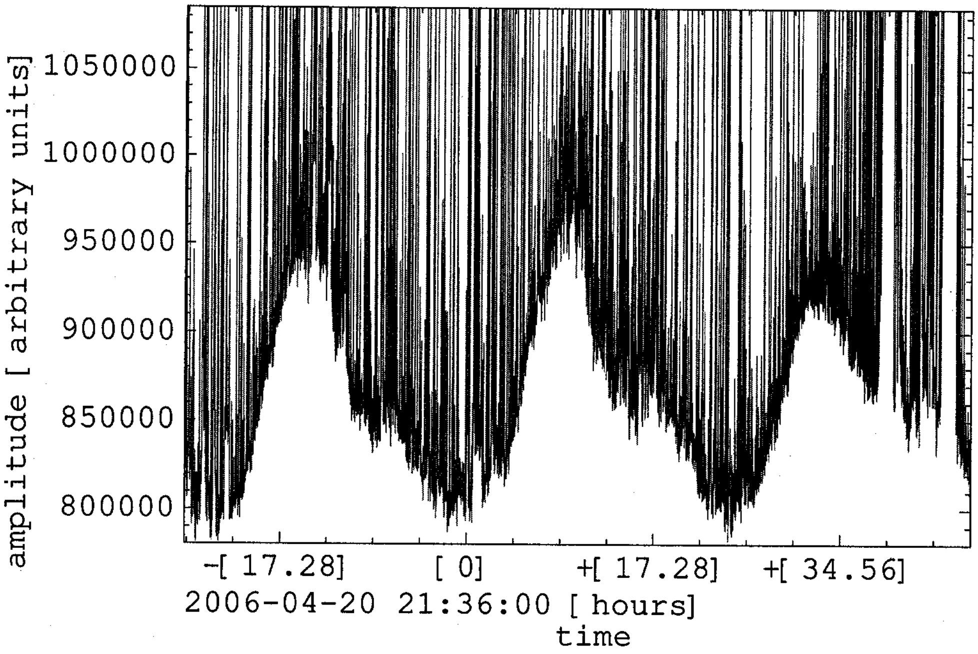

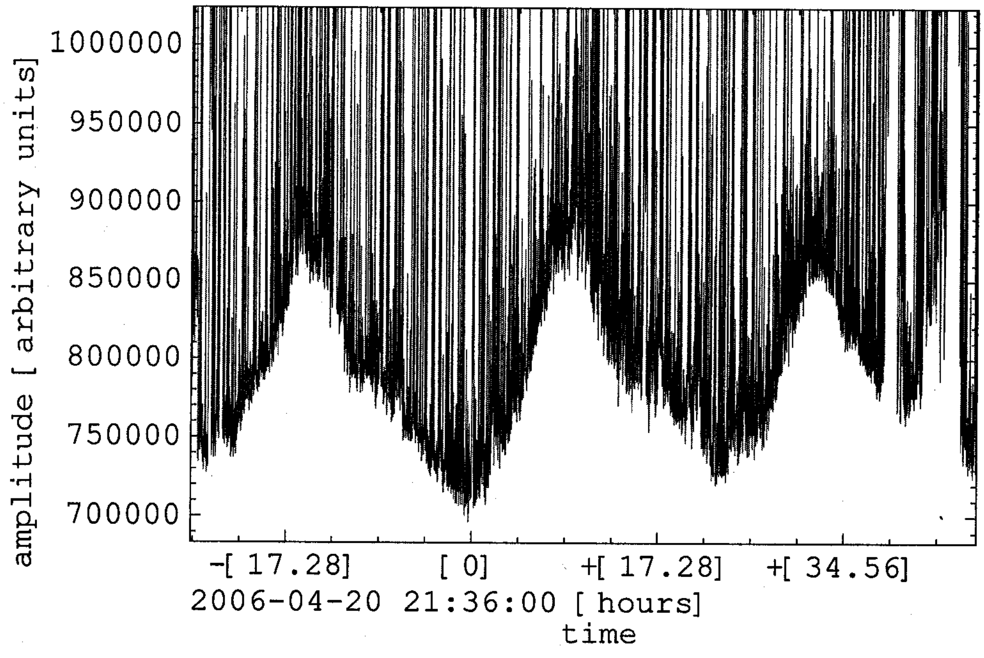

Figure 4.2: Galaxy noise with visible meteor signatures at 102.1 MHz (top) and 105.1 MHz (bottom).

Figure 4.3: Milky Way over the antenna beam. The antenna is pointed toward $\eta$ Aquila.

varied from 10+ meteors per hour.

Increased meteor activity was observed on April 22nd, 2006. In our data, two peaks are detected. Both peaks are confirmed at most of the FM bands. In Fig. 4.2 the activity of the Lyrids can be seen at 102.1 MHz and 105.1 MHz (increased activity during the third galaxy cycle just after time increment of 34.56 hours). An example of a meteor reflection, detected at multiple frequencies, during the time of the Lyrids' maximum, is shown in Fig. 4.4.

### 4.1.3 Toronto Footprint

We have selected 23 frequencies to represent a Toronto footprint. These frequencies were searched for in the data collected during the Lyrid 2006 Algonquin campaign. The list of Toronto FM stations [11] is given in Table 4.2. The goal was to find meteor trails reflecting the signals from the greater Toronto area. If transmitted at the same

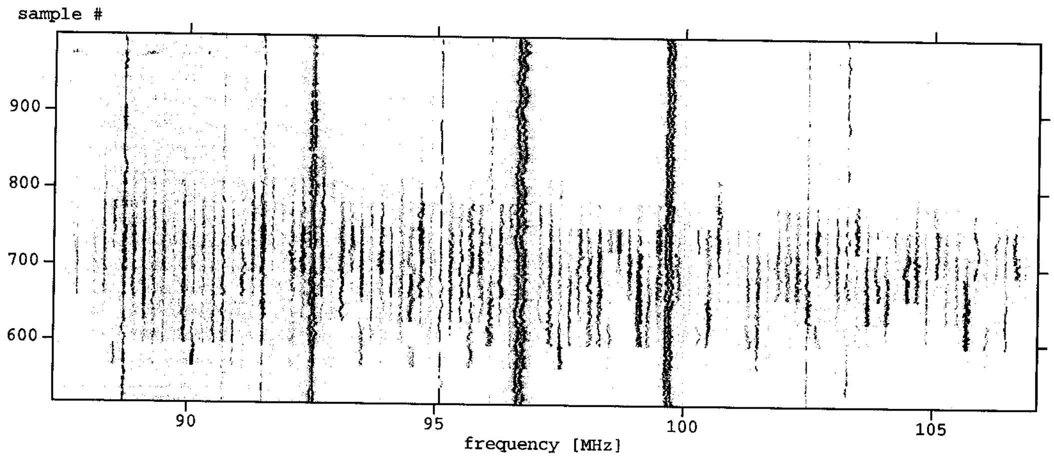

Figure 4.4: An example of meteor forward-scattering detected at multiple frequencies as evidenced by the dark bands running across most frequencies.

| *f* (MHz) | code | name | Longitude [°] | Latitude [°] |
|---|---|---|---|---|
| 88.1 | CKLN | Ryerson University | 79.381944 | 43.648889 |
| 88.9 | CIRV | Multicultural | 79.381944 | 43.648889 |
| 89.5 | CIUT | University of Toronto | 79.381944 | 43.648889 |
| 89.9 | CKRG | Glendon College | 79.381944 | 43.648889 |
| 90.3 | CJBC | Radio-Canada Espace Musique | 79.381944 | 43.648889 |
| 91.1 | CJRT | Jazz FM | 79.387500 | 43.642500 |
| 92.5 | CJAQ | Jack FM | 79.381944 | 43.648889 |
| 93.5 | CFXJ | Flow 93-5 | 79.381944 | 43.648889 |
| 94.1 | CBL | Radio Two | 79.387500 | 43.642500 |
| 97.3 | CJEZ | EZ Rock | 79.387500 | 43.642500 |
| 98.1 | CHFI | Adult contemporary | 79.387500 | 43.642500 |
| 99.1 | CBLA | CBC Radio One | 79.381944 | 43.648889 |
| 99.9 | CKFM | Mix 99.9 | 79.387500 | 43.642500 |
| 100.7 | CHIN | Multicultural | 79.387500 | 43.642500 |
| 101.3 | CJSA | Canadian Multicultural Radio | 79.381944 | 43.648889 |
| 104.5 | CHUM | Hot adult contemporary | 79.387500 | 43.642500 |
| 105.1 | CHOQ | Franco-Ontarian community station | 79.399167 | 43.705556 |
| 105.5 | CHRY | York University | 79.503056 | 43.775556 |
| 106.5 | CFIE | Aboriginal Voices Radio | 79.381944 | 43.648889 |
| 107.1 | CILQ | Q107 | 79.387500 | 43.642500 |
| 88.5 | CKDX | Foxy 88-5 (Newmarket) | 79.519167 | 44.011111 |
| 96.3 | CFMX | Classical 96.3 (Cobourg) | 78.143333 | 44.070556 |
| 102.1 | CFNY | 102.1 The Edge (Brampton) | 79.387500 | 43.642500 |

Table 4.2: Commercial FM stations heard in downtown Toronto. The last 3 are not transmitted from the city's core.

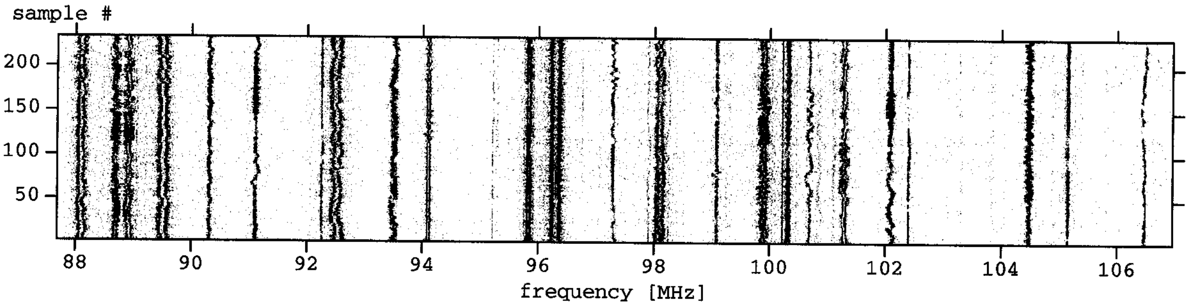

Figure 4.5: Toronto FM stations as measured at UofT. The data agree with the list of FM radio stations given in Table 4.2.

geographic location, the time lag between the first maximum of the detected waves at different frequencies should be on the order of $10^{-4}$ s. In the case of reflections of the same trail at two different frequencies, if the two transmitters are at the same location, the scattering geometry will be the same. In that case, for a fixed meteor trail, the difference between the times of the maximum of these two received signals depends only on the frequency as seen in equation (3.55). The meteoroid reaches the $t_0$ point at the same time for both reflections, and the maxima of the detected signals occur when the meteoroid arrives at the first Fresnel points for the given frequencies, $t_1(f_i)$ and $t_1(f_k)$, where $i$ and $k$ describe FM bands where detections occured. The speed of the meteoroid $v$ can be estimated using equation (3.55)

$$v = \frac{G}{t_1(f_i) f_i^{\frac{3}{2}}}, \tag{4.1}$$

where the constant $G$ carries all geometrical parameters. From the data the difference between $t_1(f_i)$ and $t_1(f_k)$ is known, so the speed can be obtained. The maximal effect is obtained for two frequencies corresponding to the beginning and the end of the FM band $\frac{t_1^B}{t_1^E} = \left(\frac{f_E}{f_B}\right)^{3/2} = 1.34$. The time needed to reach the 1st Fresnel zone after a meteoroid has passed through the $t_0$ point depends on the meteoroid's speed and can take values from $3 \times 10^{-5}$ s up to $3 \times 10^{-4}$ s. During the Lyrid maximum, we found one reflection with a possible Toronto footprint, and estimated the meteoroid speed to be (36 ± 5)

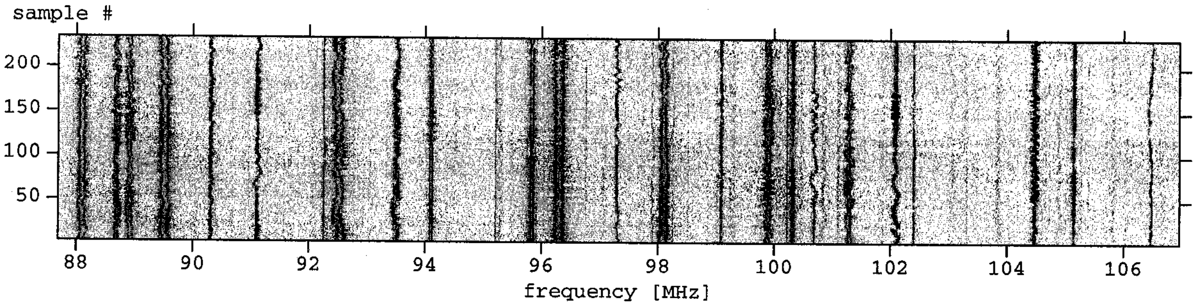

Figure 4.5: Toronto FM stations as measured at UofT. The data agree with the list of FM radio stations given in Table 4.2.

geographic location, the time lag between the first maximum of the detected waves at different frequencies should be on the order of $10^{-4}$ s. In the case of reflections of the same trail at two different frequencies, if the two transmitters are at the same location, the scattering geometry will be the same. In that case, for a fixed meteor trail, the difference between the times of the maximum of these two received signals depends only on the frequency as seen in equation (3.55). The meteoroid reaches the $t_0$ point at the same time for both reflections, and the maxima of the detected signals occur when the meteoroid arrives at the first Fresnel points for the given frequencies, $t_1(f_i)$ and $t_1(f_k)$, where $i$ and $k$ describe FM bands where detections occured. The speed of the meteoroid $v$ can be estimated using equation (3.55)

$$v = \frac{G}{t_1(f_i) f_i^{\frac{3}{2}}}, \tag{4.1}$$

where the constant $G$ carries all geometrical parameters. From the data the difference between $t_1(f_i)$ and $t_1(f_k)$ is known, so the speed can be obtained. The maximal effect is obtained for two frequencies corresponding to the beginning and the end of the FM band $\frac{t_1^B}{t_1^E} = \left(\frac{f_E}{f_B}\right)^{3/2} = 1.34$. The time needed to reach the 1st Fresnel zone after a meteoroid has passed through the $t_0$ point depends on the meteoroid's speed and can take values from $3 \times 10^{-5}$ s up to $3 \times 10^{-4}$ s. During the Lyrid maximum, we found one reflection with a possible Toronto footprint, and estimated the meteoroid speed to be $(36 \pm 5)$

km/s. The main problems with this method of estimating meteor speed are correctly identifying $t_1(f)$ and making sure that the signals producing the first reflections at the given frequencies originated at the given location, in this case Toronto. During the first observation run, the data collection was set up in such a way to try and capture events shorter than $10^{-4}$ s. The data collection was not continuous but rather filled with gaps, which reduced the number of trails with detected $t_1(f_i)$.

## 4.2 June 28 - July 18, 2006

The data collection algorithm for the second run was modified in order to capture underdense echoes with a duration of $\sim 1$ second. $2^{16}$ samples were collected in 10000 buffers amounting to 1 GB of raw data. The data were collected over a period of $\sim 20$ seconds, then during the next $\sim 20$ seconds the spectra were calculated with $2^{14}$-point FFTs, decimated and recorded on the hard disks. We collected 35000 spectra during 20 days of constant observation requiring 550 GB of disk space. To reduce the number of detected trails, the antenna was pointed north with an elevation angle of 70°. A snapshot of the spectra taken on July 9, 2006 is given in Fig. 4.6. Multiple reflections are clearly visible (see Fig. 4.7).

The level of noise is mostly influenced by Galactic emission (see Chapter 1). Since Galactic noise grows with power law toward lower frequencies, we expect to have higher meteor counts at larger frequencies. With our instrument, we are able to verify the power law growth of Galactic noise toward lower frequencies [88]. On the other hand, the detected power for meteor scattering increases with decreasing frequency, resulting in lower meteor counts at larger frequencies as shown in Fig. 4.8. The relative number of meteor trails, detected at the high end of the FM band compared to the number of trails at the low end, is in excellent agreement with equation (3.56). There are 1.8 times more meteors detected at the low end of FM band. We found the average noise level

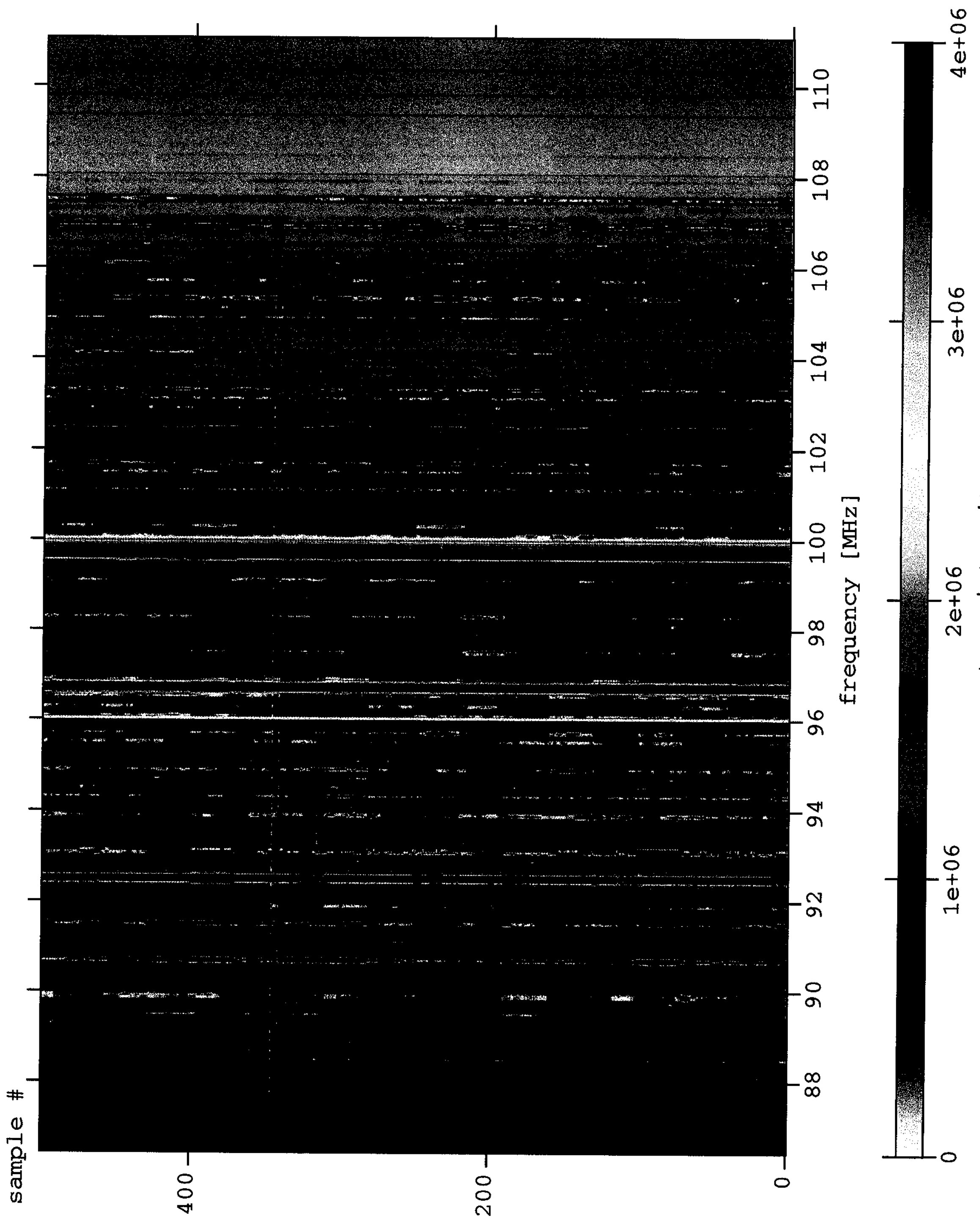

Figure 4.6: Meteor forward-scattering observed on July 9, 2006 from 06:06 until 06:30 local time. The spectrum intensity is given in arbitrary units.

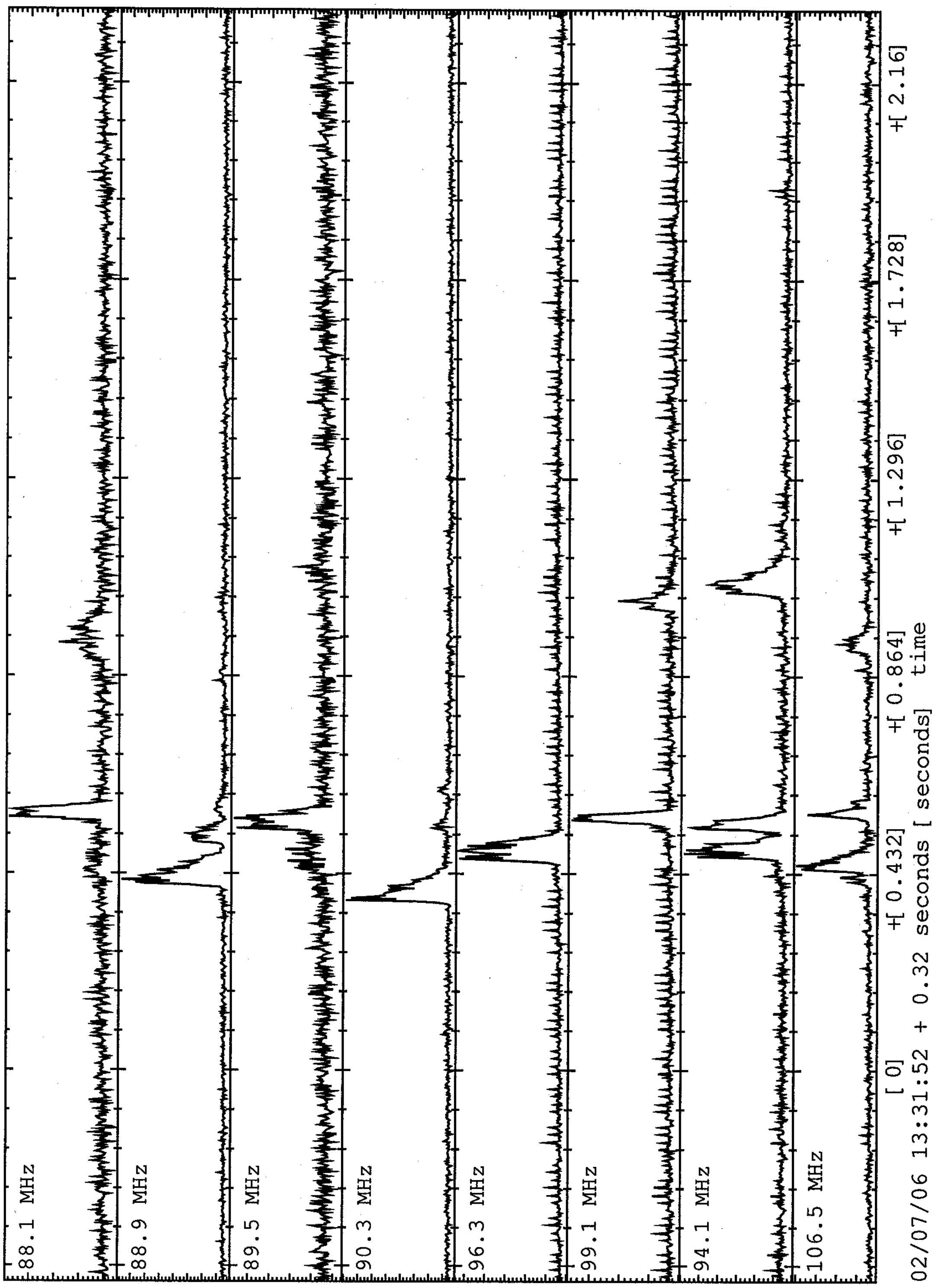

Figure 4.7: An example of forward-scattering at 8 different frequencies.

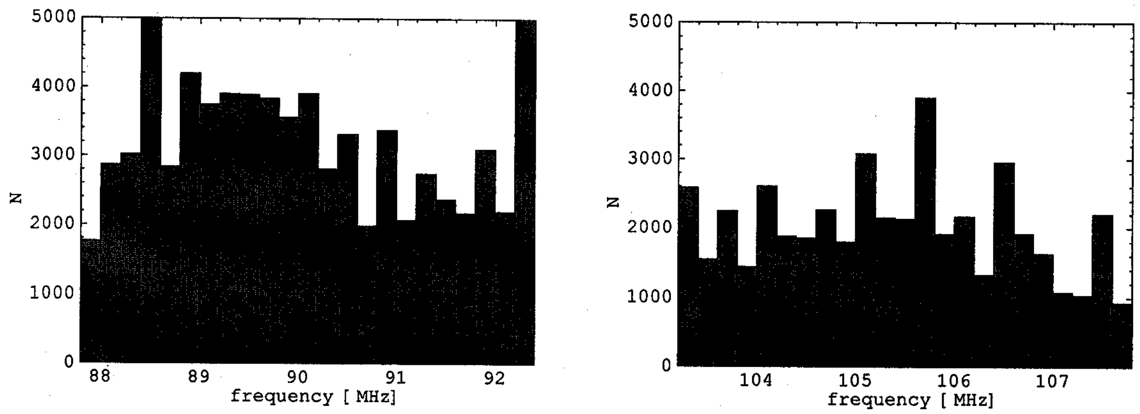

Figure 4.8: Number of detections for FM frequencies lower than 92.5 MHz (left) and higher than 103.1 MHz (right).

at each frequency and used the maximal value to define an absolute threshold level. An algorithm to detect meteor reflection at a given frequency above the threshold level was subsequently applied to the data obtained. The number of counts for three frequencies is shown in Fig. 4.9 for detections lasting less than one second and exceeding the threshold level by 5 times.

The distribution of the time length of the observed trails shorter than 5 seconds is shown in Fig. 4.10. The histogram is made for all meteors collected during the second observation run, having maximal intensity 5 times higher than the threshold, which was set to be two times higher than the average level of noise for 87.9 MHz. As expected (see Chapter 3, equation 3.57), the number of shorter trails increases as power law. Very similar results are obtained when looking at all trails detected at individual FM frequencies. When reducing the threshold level, the number of detections for a given decay time becomes higher, but the overall shape of the histogram does not change.

The distribution of amplitudes for meteor forward-scattering for the same data set is shown in Fig. 4.11. The amplitude is given in units of Kelvin per antenna beam because meteor trails are linear rather than point sources so the total number will decrease as the antenna half power beamwidth. The description of the beam used was given in

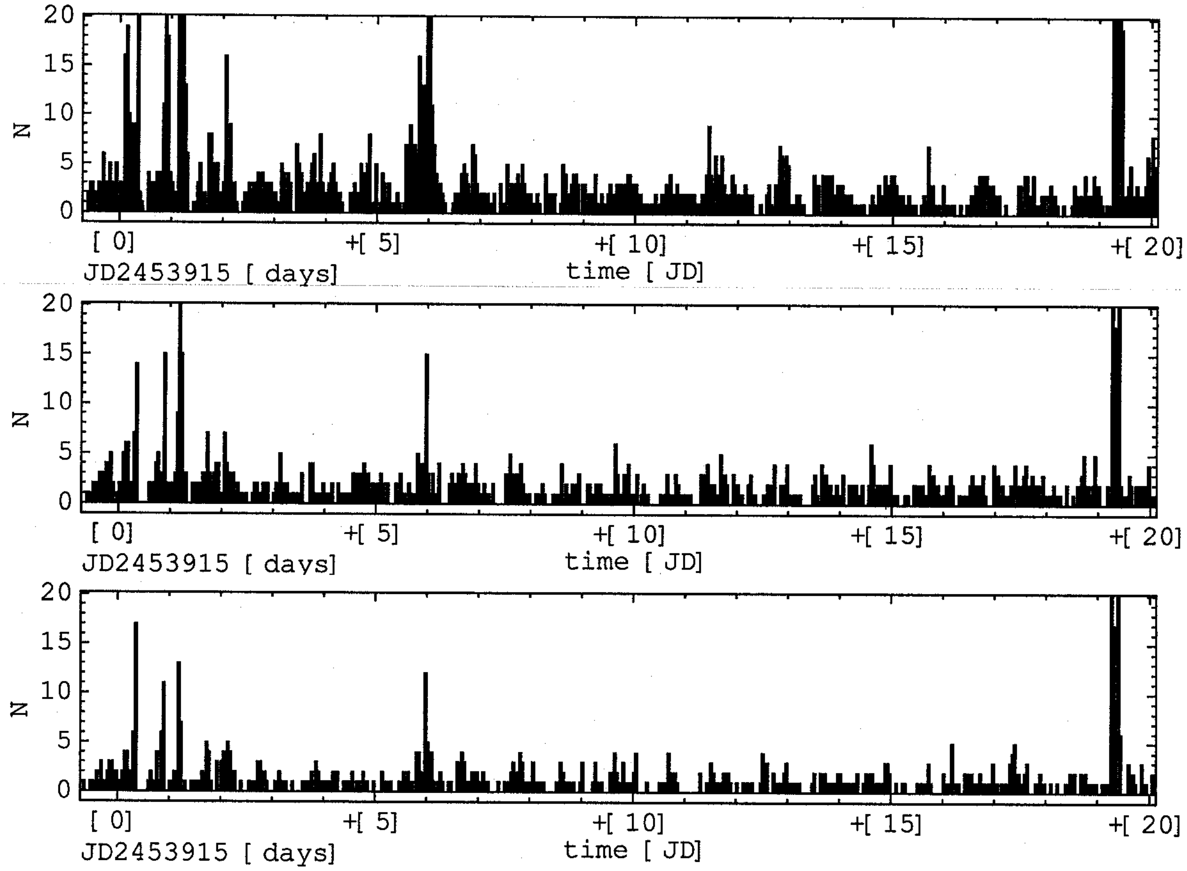

Figure 4.9: Meteor counts at 88.1 MHz (top), 103.5 MHz (middle) and 107.3 MHz (bottom). Each bin represents 1 hour of data.

subsection 2.1.1, Fig. 2.8. The calibration is done by estimating the sky temperature at different frequencies and comparing such numerical results at different time moments with the corresponding real data. The estimation of the sky temperature measured by the antenna is done using the simulated map of the sky at FM frequencies, as in subsection 1.2.2, Fig. 1.2 for a given pointing of the antenna with the beam patterns from Fig. 2.8. Depending on the time of the day and the pointing of the antenna, the Galactic signal changes in magnitude (see Fig. 4.2) alowing us to calibrate the measured signal. The results presented in Fig. 4.11 can be used as a useful reference for estimating levels of noise due to meteor forward-scattering.

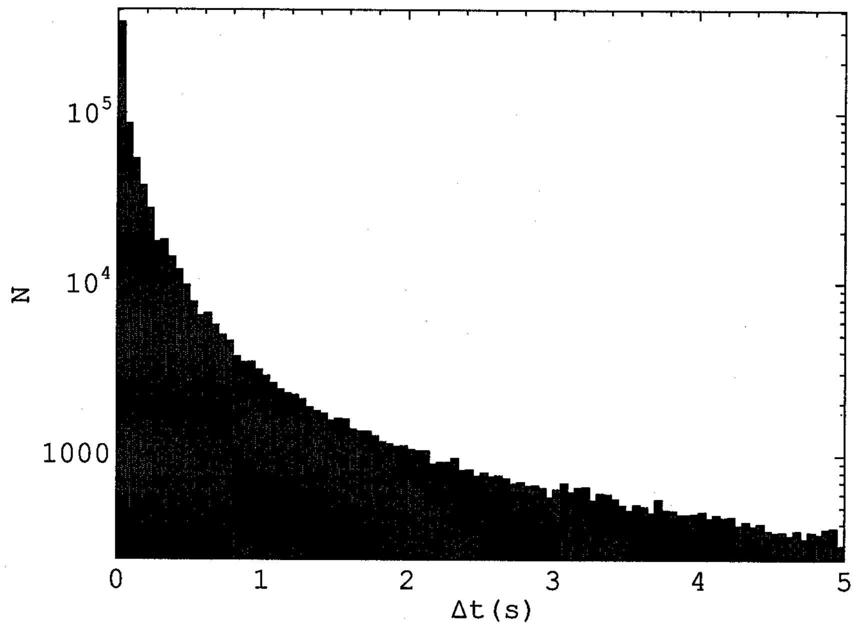

Figure 4.10: Distribution of decay times of meteors collected during 20 day long observation run in June-July, 2007. Each bin is 0.01s wide.

The cumulative number of meteor reflections estimated for a year of observations with a TREX-type instrument, capable of real time data acquisition, is plotted in Fig. 4.12. $N(T)$ is a number of reflections causing a temperature higher than $T$. It is important to note that despite large antenna beam halfwidth (see Fig. 2.8), TREX does not cover the full sky, but rather about one tenth of the sky. In addition, the data from Fig. 4.12 can be extrapolated over the whole Earth. Knowing that meteoroid trails can be detected at distances of up to 1600 km (see subsection 1.4, equation 1.7), the cumulative number of meteoroids, causing brightness temperature in the given range, entering the Earth's atmosphere will be about 1000 times larger than plotted in Fig. 4.12. Also, a certain number of meteoroid trails can not be detected due to geometric constraints. Using the analytic method presented in sections 3.3 and 3.4 I have performed Monte Carlo simulations to estimate which fraction of plasma trails can be detected. It is estimated that TREX detects about 4% of all meteoroid trails entering the Earth's atmosphere.

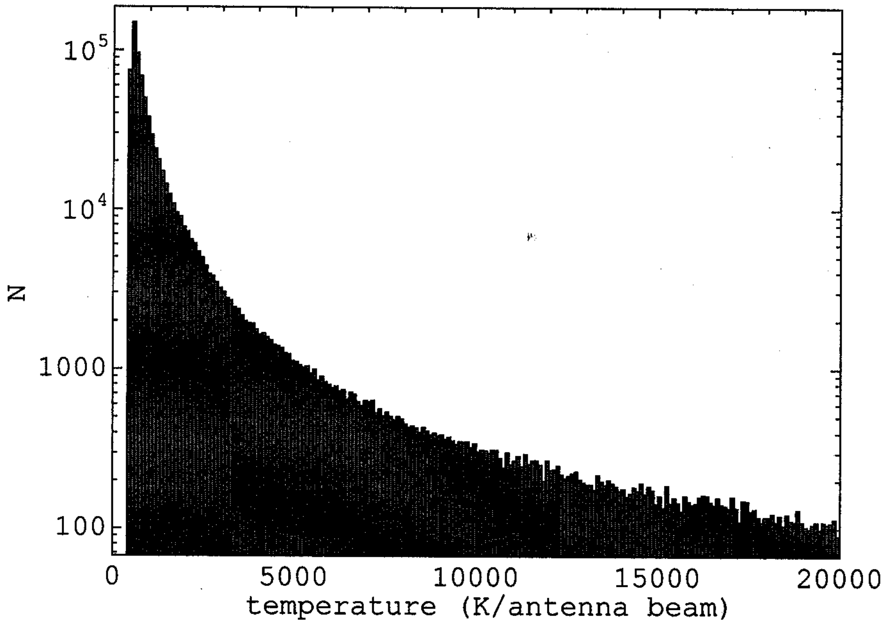

Figure 4.11: Histogram of maximal amplitudes for the forward-scattering data collected in 20 days. Each bin corresponds to change of sky temperature of 100K.

Information about the mass of a meteoroid is carried within the forward-scattering power detected at a receiver. The linear electron density from equation (3.3) can be substituted into equations (3.56) and (3.58) in order to obtain maximal detected power for underdense and overdense trails, respectively. The other parameters in equations (3.56) and (3.58) are geometric in origin and do not depend on physical properties of the observed meteoroid. Fig. 4.13 shows distribution of received power for $10^6$ simulated meteor trails, all with the identical mass, composition and speed. If all meteoroids entering the Earth's atmosphere are of the same size, made of the same material and have identical speed, the observations would produce similar results. The electron density can be exactly determined only when the line describing the ionized trail is known. In the subsection 3.7.2, I have shown that the calculation of orbital parameters from meteor forward-scattering at multiple frequencies cannot be done in real time using the tested numerical algorithms. However, masses of meteoroids detected by TREX can be

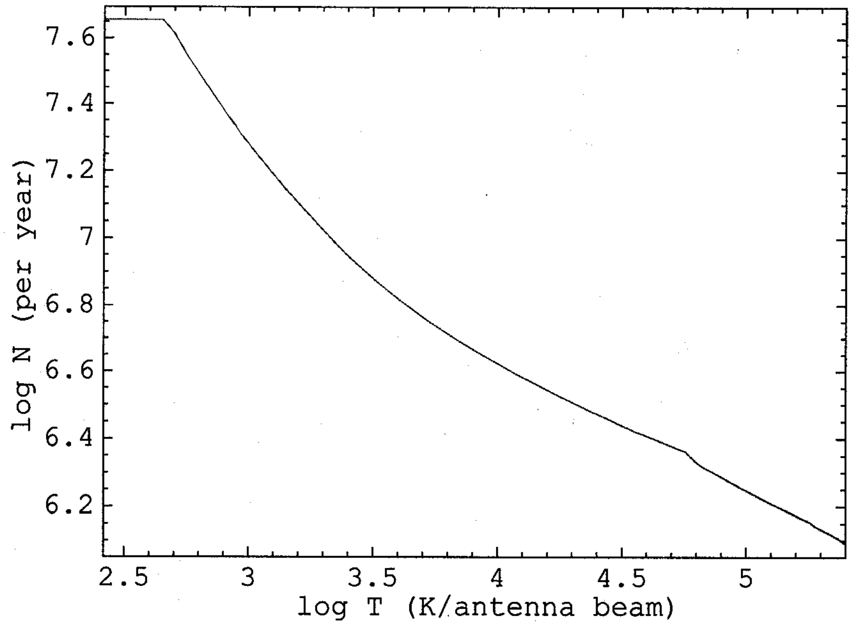

Figure 4.12: The cumulative number of meteor reflections per year detectable with a TREX type of antenna having the brightness temperature larger than or equal to T. Shown are the observed data given in Fig. 4.11 extrapolated over a period of one year. The cutoff at low temperatures is due to the noise threshold level.

estimated by comparing my data with previously published results giving the cumulative number of meteoroids entering Earth's atmosphere per year [67], [24], [15]. Averaging the number of detected meteors with TREX (Fig. 4.12) over the whole surface of Earth, with the beam covering the whole sky, and including those meteor trails which cannot be detected due to geometry, the number of trails per year, at brightness temperature of 500 K is roughly $10^{15}$. That number includes all meteoroids with masses larger than some mass $m_0$. Comparing with the estimates given in Ceplecha et al, 1998 [15] (Fig. 25), it can be concluded that TREX is capable of detecting particles of masses larger than $10^{-8}$ kg.

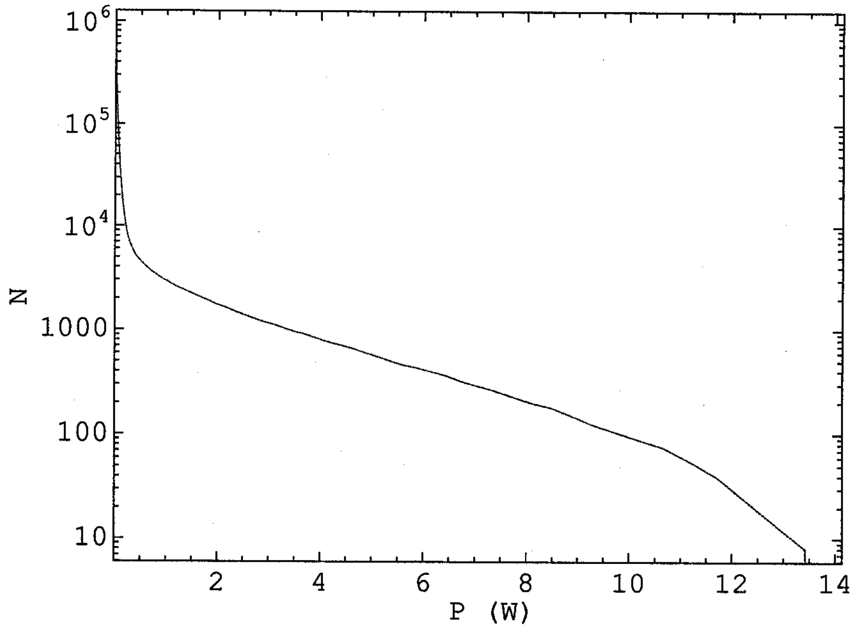

Figure 4.13: Cumulative number of simulated meteor reflections with received power larger than or equal to P. All simulated meteoroids have identical mass, composition and speed, and differ only in velocity direction. The linear electron density is assumed to be $10^{15}$ $\mathrm{m}^{-1}$, the frequencies of all transmitters are set to 100 MHz, and gains of a receiver and the transmitters are 1.

### 4.2.1 Diurnal Variation of Meteor Activity

A maximal number of detected trails is expected at 6 a.m. local time, and the minimal number of trails at 6 p.m. local time [123], [50], [135]. The maximum is in the early morning hours since at that time, the apex is in its highest position in the sky, and the observer is capable of seeing the trails from meteoroids with velocity vectors directed toward the Earth as well as those overtaken by the Earth. When the observer is facing antiapex (early evening hours), only the meteoroids fast enough to overtake the Earth are visible. This diurnal variation is clearly visible in our data. Fig. 4.14 shows the variation in the number of meteors shorter than one second. The effect is also visible when looking at the data for individual FM frequencies (see Fig. 4.9).

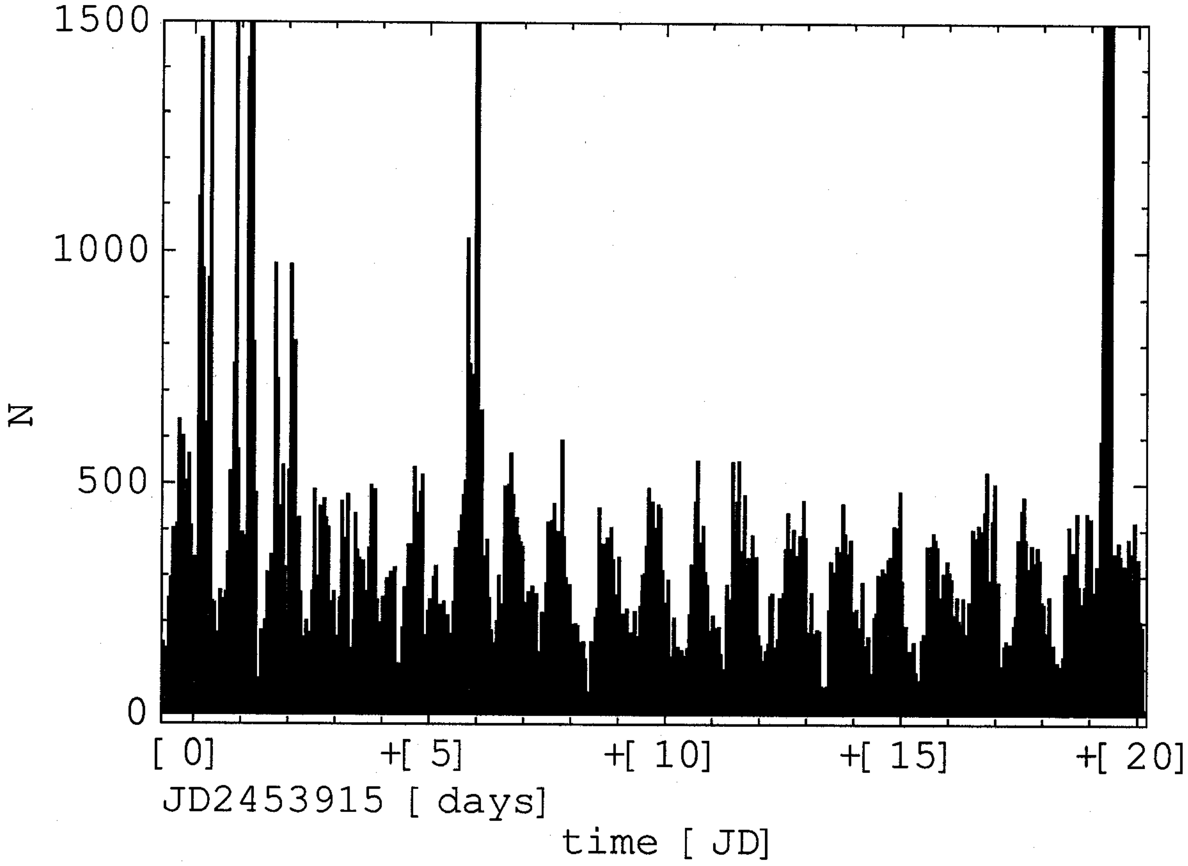

Figure 4.14: Diurnal variations in the number of observed trails. Each bin represents 1 hour of data.

### 4.2.2 Pegasids

The Pegasid meteor shower was supposed to be active from July 07-13, 2006 with its maximum on July 09, 2006 and the radiant at (340°, 15°) [99], [72]. The Pegasids should be fast meteoroids with an average velocity of 70 km/s. Our simulations show that the radiant of this stream is in an excellent position on the sky in the early morning hours at the time of maximum. Our setup, using thousands of FM transmitters, had an excellent opportunity to scan for Pegasid activity.

In our data there are no indications of this shower (see Fig. 4.9 and Fig. 4.14 for Julian date 2453926.0 corresponding to July 9, 2006, noon). Our results confirm the work given in [138] where the authors showed that there is no evidence for this meteor shower in video observations during the 2001-2004 period, but there were some indications that this shower might be detectable in radio observations. At the present time, no one has reported Pegasid activity in 2006 [139].

# Chapter 5

# Conclusion

In this thesis, the design of a radio frequency digital spectrometer called TREX was described. The instrument was built, tested and used to make two sets of observations at the Algonquin Radio Observatory in April and June-July, 2006. The observations were focused on meteor forward-scattering detection and on the characterization of the sky spectrum in the RF band. This is the first study of meteoroid detection at multiple frequencies, revealing properties of the radio sky which will be very useful for the future planning of observatories capable of detecting the epoch of reionization.

Advances in digital electronics now allow us to develop digital spectrometers which can be used to probe the epoch of reionization in the universe and to do meteor physics. Digital radio spectrometers offer many advantages over the traditional approach toward radio observations. These detectors have a much simpler design than the old fashioned receivers which use mixers, as explained in Chapter 2. Perhaps the most important component of an RF spectrometer is its antenna. We used a rectangular approximation of a two arm conical spiral antenna as a basic design for our broadband receiver. This antenna is optimized for capturing frequencies in the 70-250 MHz range.

In order to obtain power spectra from the data collected, a new and efficient FFT algorithm was developed. It was implemented for Intel Pentium 4 SIMD processors.

Working with integers, this algorithm performs 8 FFT calculations at once and is significantly faster than conventional FFT algorithms. We have used it to reconstruct various spectra and to find meteor trail reflections, demonstrating its suitability for our purposes.

Knowledge of the epoch of reionization is a missing key in our understanding of the formation of the first stars. Were the first stars formed simultaneously across the whole Universe? What were the most luminous sources in the reionization epoch? Questions such these can most effectively be addressed only after successful reionization observations have been made and analyzed. In addition, measurement of the reionization signature can be used to probe modern cosmology theories. The 21 cm line of neutral hydrogen emitted during the Dark Ages has been redshifted up to metre wavelengths, or in frequency terms, somewhere between 70-250 MHz. The older the radiation, the longer the wavelength, and the lower the frequency of the received signal. With the reionization of the Universe, and loss of neutral hydrogen, this emission ceased to exist, forming a sharp step in the all-sky broadband spectrum.

Measurement of the reionization step is a difficult task. The signal corresponding to the step is more than 4 orders of magnitude below the galactic noise. The location of an instrument with the purpose of detecting the reionization signal has to be chosen very carefully. The bands where the signal is supposed to be are contaminated by human produced waves. The propagation of waves in the 30-300 MHz range is "in the line-of-sight", and any obstruction in this optical path causes significant attenuation. The transmitter antennas are usually mounted on towers, with a typical line-of-sight range of less than 100 km. The amount of RF frequency radiation correlates with the population density, requiring an observation location that is relatively isolated. Despite these difficulties, we suggest that a spectrometric system, composed of two or more rescaled small telescopes with 1% rescaling can take adventage of the signal's all-sky presence and would be able to measure a temperature step of $\sim 0.02$K in the range of 150-250MHz ($5 < z < 8.5$).

The single dish radio telescope at the Algonquin Radio Observatory works in gigahertz frequency bands and the spectrum pollution in the lower frequency bands ($< 1$ GHz) was not well studied. I have tested the RF frequency noise levels and detected a larger amount of noise in the RF bands than expected, despite the isolation of the site. A portion of the noise is due to human activity: radio stations in the FM band, TV stations, and also by devices in some other communication channels.

There is also the noise introduced by meteor forward-scattering which can seriously affect attempts to observe the 21 cm redshifted line coming from the time of reionization. The number of reflections has daily variations with the maximum occuring in the early morning hours and the minimum in the early evening. Reionization experiments such as CORE will have to design a special software filter in order to account for meteor activity. The postprocessing removal of this type of noise is difficult due to variations in meteor counts, as well as jumps in the power intensity received from each individual scattering. LOFAR will not even attempt to use FM frequencies, while MWA will have the same problem as CORE. Fortunately, the large number of antennas in the array permits an accurate determination of meteor trail position [104]. By analysing a map of the sky at a given moment, the meteor noise can be removed [105].

The main part of this thesis has been concerned with meteor forward-scattering. I have shown that meteoroids produce ionized trails that are in a plasma state. Simple estimates of the power received by radar and forward-scattering observations were given. A variation in signal intensity with time has been modeled and successfully compared to real observations. The geometry of a forward-scattering system was discussed in detail, resulting in an original analytic solution if a particular meteor trail causes the reflection for a given forward-scattering system. For a given meteor line, the method checks whether there exists an ellipsoid, with foci at a receiver and transmitter. Our approach is computationally faster than any of the numerical methods that have been used so far. A simple algorithm that applies our analytical solution has been used to generate ground illumination footprints of meteors and to find the observability functions for a meteor shower.

With more detections of the same meteor at many different frequencies, it is possible to determine its kinetic parameters without making any assumptions about the physical properties of the trail. I have shown that each meteor trail leaves a unique signature in the time evolution of the spectrum. Identifying the correct meteor from observational data is shown to be a very computationally intensive task. To find a meteor that fits the observations, it is best to search through a seven parameter space. A cost function for searching the parameter space has been proposed and tested. However, a "brute force" search through the entire parameter space with the needed resolution, on a single-top-of-the-line computer processor at the present time, would last a minimum of 300000 years. We have also tested a number of numerical methods for parameter searching. However, there are a number of local minima in the search space which make this problem hard to solve.

Commercial FM stations can be used as transmitters for forward-scattering observations. Knowing that in the whole FM band there is enough space for only 100 radio stations, there is a problem identifying the detected transmitter. This makes numerical method fitting of the observed data more complex than in a case when the transmitters are unique and well known. We have shown how observations of meteor forward-scattering at multiple frequencies, with known transmitters at the same location, can be used to characterize meteoroid speeds. Once the speed of the meteor is known, the orbit estimation problem becomes slightly less difficult.

I have demonstrated that the Algonquin site represents an excellent location for observations of meteor forward-scattering. However, for the more precise measurements required to detect the global signature of reionization, the amount of terrestrial man-made noise is too large.

## 5.1 Recommendations for Future Work

The instrument described in this thesis is an obvious demonstration of the potential of a small radio frequency spectrometer. Such an instrument can be optimized in various ways depending on the particular observation target. In the near future, the processing power of small personal computers will be sufficient enough for real time data processing. At the same time, streaming of all data from an 8 bit 500 MHz A/D converter to the main computer memory will be possible. An increase in the speed of data transfer and computation will bring higher temporal and spectral resolution. In the future, the faster FFT algorithm presented here can be expanded to a new generation of processors and graphic cards to maximize the computation speed by combining efficient software with new hardware. By synchronizing two or more TREX systems, a cheap and simple interferometer could be built. The main advantages of using the rectangular approximation of a 2ACSA antenna described in this work are its excellent broadband characteristics, and its mechanical simplicity.

The question of observing the redshifted 21 cm reionization line is still open. I have pointed toward some of the yet unforeseen problems when planning these observations. How to correctly estimate the amount of noise originating from meteor forward-scattering, and the effect of such noise on the reionization signature, is still not known. Despite the construction of large scale instruments such as LOFAR, there are no known algorithms to remove meteor noise. By reducing the bandwith and excluding FM bands, the planners of LOFAR tried to minimize spectrum mitigation. However, forward-scattering also exists in other bands. Algorithms for removing this type of noise will have to be designed and this work is an excellent starting point for such future research.

In the general case, the physics of oblique scattering can be tested using multifrequency observations through data based on a TREX-type of instrument. Seeing a single meteor trail reflection at multiple frequencies permits intensive study of reflections having different geometries. Construction of a forward-scattering system with a number of completely known transmitters, each transmitting at a different frequency, would completely remove the problem of recognizing the location of the transmitters. In addition, the effects of the polarization of the detected waves could be studied.

The method for finding the orbital parameters of a meteoroid, observed at multiple frequencies via single antenna receiver, could be improved by designing an interferometer capable of estimating the location of the ionized trail. The pipeline for extracting information on meteoroid orbital parameters from multi frequency observations proposed in this work is far from a real time application. The parameter space with the six unknowns (see section 3.7.2) is filled with a number of local minima thus making numerical search methods almost useless. The brute force search is computationaly slow and, using a single processor, might last hundreds of thousands of years. Additional information on a given meteor reflection could speed up the search of parameter space. An interesting project would be to build a digital interferometer for estimating the location of the trail and use thus obtained data to constrain the parameter space.

TREX, or a similar multi-frequency instrument, could also be used to test a number of theories on meteors. Determination of trail height from Foschini's work [32] could be tested by knowing the position of transmitters and their radiation patterns. Also, the estimation of a meteor shower flux from Belkovich's work [4] might be tested. Finally, a number of trail and ionospheric parameters, such as diffusion coefficients, could be measured precisely. We have also discussed how an instrument similar to TREX could be used for military purposes.

We are slowly entering a new age in radio astronomy: the age of digital instruments. When this project was started, there were only whispers of low frequency spectrometers. Today, there are a few systems under construction, most of them connected with the SKA project which is expected to be fully operational in 2020. TREX is one of the first digital radio spectrometer projects, but it certainly will not be the last.

# Appendix A

# Coordinate Transformations

In this appendix, general rules for 3D coordinate transformation will be discussed. Firstly, the matrix method will be reviewed followed by a quaternion approach.

## A.1 3D Coordinate Transformations using Rotational Matrix

### A.1.1 Translation

Let **X** be the vector pointing at a point ($x$,$y$,$z$) in the old coordinate system. With **X**' we will describe the coordinates of the same point but in the new coordinate system. Translation is defined as

$$\mathbf{X}' = \mathbf{X} - \mathbf{T}, \tag{A.1}$$

where the vector **T** defines coordinates of the new origin O' with respect to the old coordinate system. Using matrix notation we can rewrite the previous equation as

$$\begin{bmatrix} x' \\ y' \\ z' \end{bmatrix} = \begin{bmatrix} x \\ y \\ z \end{bmatrix} - \begin{bmatrix} \Delta x \\ \Delta y \\ \Delta z \end{bmatrix}.$$

### A.1.2 Rotation in 3D

3D space is defined by three orthogonal axes. Each axis can be rotated by the so called "Euler angle". When one of the positive $x$, $y$, $z$ coordinates is chosen as the axis of rotation, then the rotation is similar to that of 2D space. The rotation around any given axis can be presented as a sequence of three rotations about the Euler angles. A single rotation about the $i$-axis is defined as

$$\mathbf{X}' = \mathbf{R}_i\mathbf{X},$$

where $i$ can be $x$, $y$ or $z$. The rotation matrices for the rotations around $x$, $y$ and $z$ axes about angles $\alpha$, $\beta$ and $\gamma$ are

$$R_x = \begin{bmatrix} 1 & 0 & 0 \\ 0 & \cos(\alpha) & \sin(\alpha) \\ 0 & -\sin(\alpha) & \cos(\alpha) \end{bmatrix},$$

$$R_y = \begin{bmatrix} \cos(\beta) & 0 & -\sin(\beta) \\ 0 & 1 & 0 \\ \sin(\beta) & 0 & \cos(\beta) \end{bmatrix}$$

and

$$R_z = \begin{bmatrix} \cos(\gamma) & \sin(\gamma) & 0 \\ -\sin(\gamma) & \cos(\gamma) & 0 \\ 0 & 0 & 1 \end{bmatrix} \tag{A.2}$$

respectively. One should remember that a positive rotation is assumed to be counter clockwise. The general case is obtained using three sequential rotation

$$\mathbf{X}' = R_x R_y R_z \mathbf{X}$$

It is important to note that the order of performing rotations matters, i.e.

$$R_x R_y R_z \neq R_z R_y R_x.$$

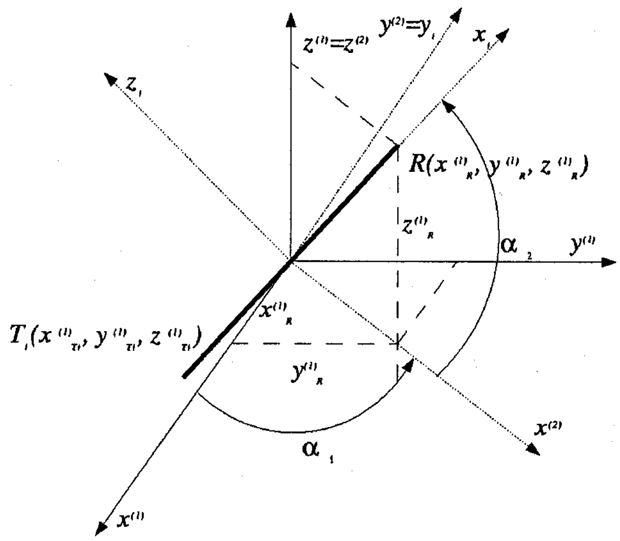

Figure A.1: Rotations needed to bring an initial 3D coordinate system ($x^{(1)}$, $y^{(1)}$, $z^{(1)}$) into the coordinates with x-axis oriented along the TR baseline. The rotation is done in two steps: firstly, the initial system ($x^{(1)}$, $y^{(1)}$, $z^{(1)}$) is rotated about $z^{(1)}$-axis by an angle $\alpha_1$ into the secondary coordinates ($x^{(2)}$, $y^{(2)}$, $z^{(2)}$); secondly, the temporary system is rotated about $y^{(2)}$-axis by an angle $\alpha_2$.

### A.1.3 Ellipsoid Equations in the New Coordinates

The center of the ellipsoid with foci at the receiver ($x_R$, $y_R$, $z_R$) and the $i$-th transmitter ($x_{Ti}$, $y_{Ti}$, $z_{Ti}$) is defined as

$$x_{Ci} = \frac{x_R + x_{Ti}}{2}, \quad y_{Ci} = \frac{y_R + y_{Ti}}{2} \quad \text{and} \quad z_{Ci} = \frac{z_R + z_{Ti}}{2}. \tag{A.3}$$

To switch into coordinates "native" to the $T_i - R$ ellipsoid, we have to translate the origin to the center of the ellipsoid defined by (A.3), and perform two rotations in order to match the $x$-axis with $x_i$. Necessary rotations are shown in Fig. A.1.

Translation of the origin to ($x_{Ci}$, $y_{Ci}$, $z_{Ci}$) is performed according to the transformation of 3D rectangular coordinates rules defined in (A.1). The receiver and the transmitter coordinates in the new coordinates can be called $R^{(1)}(x^{(1)}_R, y^{(1)}_R, z^{(1)}_R)$ and

$T_i^{(1)}(x_{Ti}^{(1)}, y_{Ti}^{(1)}, z_{Ti}^{(1)})$, respectively. Coordinates of the receiver can be written as

$$\begin{aligned} x_R^{(1)} &= x_R - x_{Ci} \\ y_R^{(1)} &= y_R - y_{Ci} \\ z_R^{(1)} &= z_R - z_{Ci}. \end{aligned}$$

Similar expressions can be written for the $i$-th transmitter.

To finish our coordinate transformation we must rotate our axes in such a way that both foci lie on the $x'$-axis. We can start by fixing the $z^{(1)}$-axis and rotating $x^{(1)}$-$y^{(1)}$ by the angle $\alpha_1$

$$\cos\alpha_1 = \frac{x_R^{(1)}}{\sqrt{\left(x_R^{(1)}\right)^2 + \left(y_R^{(1)}\right)^2}},$$

or

$$\cos\alpha_1 = \frac{x_{Ti}^{(1)}}{\sqrt{\left(x_{Ti}^{(1)}\right)^2 + \left(y_{Ti}^{(1)}\right)^2}}$$

to obtain the new intermediate coordinates $x^{(2)}, y^{(2)}, z^{(2)}$. Any of the two expressions should give us the same result since the origin bisects the T-R line. The rotation is performed by using the rotation matrix as defined in (A.2)

$$\begin{bmatrix} x^{(2)} \\ y^{(2)} \\ z^{(2)} \end{bmatrix} = \begin{bmatrix} \cos\alpha_1 & \sin\alpha_1 & 0 \\ -\sin\alpha_1 & \cos\alpha_1 & 0 \\ 0 & 0 & 1 \end{bmatrix} \begin{bmatrix} x^{(1)} \\ y^{(1)} \\ z^{(1)} \end{bmatrix}.$$

In the final step, $y^{(1)} = y^{(2)}$ will be kept constant and $x^{(2)}$-$y^{(2)}$ will be rotated by the angle $\alpha_2$

$$\sin\alpha_2 = \frac{z_R^{(1)}}{\sqrt{\left(x_R^{(1)}\right)^2 + \left(y_R^{(1)}\right)^2 + \left(z_R^{(1)}\right)^2}},$$

or

$$\sin\alpha_2 = \frac{z_{Ti}^{(1)}}{\sqrt{\left(x_{Ti}^{(1)}\right)^2 + \left(y_{Ti}^{(1)}\right)^2 + \left(z_{Ti}^{(1)}\right)^2}}$$

The second rotation written in matrix notation is

$$\begin{bmatrix} x_i \\ y_i \\ z_i \end{bmatrix} = \begin{bmatrix} \cos\alpha_2 & 0 & \sin\alpha_2 \\ 0 & 1 & 0 \\ -\sin\alpha_2 & 0 & \cos\alpha_2 \end{bmatrix} \begin{bmatrix} x^{(2)} \\ y^{(2)} \\ z^{(2)} \end{bmatrix}.$$

In the last step, both rotations written together are $X_i = R_{\alpha_2} R_{\alpha_1} X$. After multiplying the rotation matrices, we obtain

$$\begin{bmatrix} x_i \\ y_i \\ z_i \end{bmatrix} = \begin{bmatrix} \cos\alpha_1 \cos\alpha_2 & \sin\alpha_1 \cos\alpha_2 & \sin\alpha_2 \\ -\sin\alpha_1 & \cos\alpha_1 & 0 \\ -\cos\alpha_1 \sin\alpha_2 & -\sin\alpha_1 \sin\alpha_2 & \cos\alpha_2 \end{bmatrix} \begin{bmatrix} x^{(1)} \\ y^{(1)} \\ z^{(1)} \end{bmatrix}.$$

## A.2 3D Rotations Using Quaternions

The theory of quaternions is a powerful tool describing 3D rotations about an arbitrary axis. Introduced in the 19th century by the Irish mathematician Sir William Rowan Hamilton, quaternions became an important part of modern aerospace calculations, the special theory of relativity, mechanics, and computer graphics [63], [81]. It has been shown that combining many quaternion transformations is numerically more stable than combining multiple matrix transformations. This approach avoids a gimbal lock, a problem caused by the alignment of two of the three Euler angles together so that one of the rotation references is canceled. Quaternions are composed of only 4 components, making their use more attractive than the use of 3x3 rotational matrices. Furthermore, computationally, successive rotations are performed more quickly.

### A.2.1 Mathematical Definition of Quaternions

Quaternions form a 4-dimensional non-commutative division algebra over the field of real numbers with respect to the operations of addition and multiplication. Each quaternion contains 4 scalar variables $\mathbf{q} = (w,\ x,\ y,\ z)$, similar to a 4D vector. For simplicity, the last three variables can be written as a single 3D vector $\mathbf{r}$. The quaternion then becomes $\mathbf{q}=(w,\ \mathbf{r}) = w + x\mathbf{i} + y\mathbf{j} + z\mathbf{k}$, where $i$, $j$ and $k$ are orthonormal vectors satisfying the rules

$$\mathbf{i}^2 = \mathbf{j}^2 = \mathbf{k}^2 = -1$$

$$\mathbf{i} \times \mathbf{j} = -\mathbf{j} \times \mathbf{i} = \mathbf{k}$$

$$\mathbf{j} \times \mathbf{k} = -\mathbf{k} \times \mathbf{j} = \mathbf{i}$$

$$\mathbf{k} \times \mathbf{i} = -\mathbf{i} \times \mathbf{k} = \mathbf{j}$$

Quaternions can be added and multiplied as a single unit in the same manner as real numbers in algebra. Quaternions form a commutative group under addition with the identity element (0, 0, 0, 0). The addition of two quaternions

$$\begin{aligned} \mathbf{q}_1 &= (w_1,\ x_1,\ y_1,\ z_1) = (w_1,\ \mathbf{r}_1) \quad \text{and} \\ \mathbf{q}_1 &= (w_1,\ x_1,\ y_1,\ z_1) = (w_1,\ \mathbf{r}_1) \end{aligned}$$

is performed using the same rule as in the case of vectors

$$\mathbf{q}_1 + \mathbf{q}_2 = (w_1 + w_2,\ x_1 + x_2,\ y_1 + y_2,\ z_1 + z_2),$$

while multiplication is defined by

$$\mathbf{q}_1\mathbf{q}_2 = (w_1w_2 - \mathbf{r}_1\mathbf{r}_2,\ w_1\mathbf{r}_2 + w_2\mathbf{r}_1 + \mathbf{r}_1 \times \mathbf{r}_2).$$

Quaternion multiplication is not commutative ($\mathbf{q}_1\mathbf{q}_2 \neq \mathbf{q}_2\mathbf{q}_1$). The conjugate $\mathbf{q}^*$ of a quaternion $\mathbf{q} = (w,\ \mathbf{r})$ is defined as

$$\mathbf{q}^* = (w,\ -\mathbf{r}),$$

and the norm $||\mathbf{q}||$ is a scalar value

$$||\mathbf{q}||^2 = \mathbf{q}\mathbf{q}^* = w + \mathbf{r}^2.$$

For their application to 3D rotations it is important to define a unit quaternion as any quaternion satisfying $||\mathbf{q}|| = 1$. The inverse of a quaternion is

$$\mathbf{q}|^{-1} = \frac{\mathbf{q}^*}{||\mathbf{q}||^2}, \qquad ||\mathbf{q}|| \neq 0.$$

Every non-zero quaternion has a multiplicative inverse making quaternions a non-commutative division ring. After introducing a distance function $d(\mathbf{q}_1, \mathbf{q}_2)$, quaternions form a metric space (isometric to the usual Euclidean metric on $\mathrm{R}^4$) and the arithmetic operations are continuous. Using the absolute value as a norm, quaternions form a real Banach algebra.

### A.2.2 3D Rotations Using Quaternions

A rotation in 3D space about a unit axis $\mathbf{r}$ for an angle $\theta$ can be significantly simplified using the representing quaternion

$$\mathbf{q} = (\cos\frac{\theta}{2},\ \mathbf{r}\sin\frac{\theta}{2}).$$

For a proper rotation $\mathbf{q}$ must be a unit quaternion. The rotation of the vector $\mathbf{v}$ by an angle $\theta$ about a unit axis $\mathbf{r}$ can be conveniently represented by a quaternion product

$$(0,\ \mathbf{v}') = \mathbf{q} \cdot (0,\ \mathbf{v}) \cdot \mathbf{q}^{-1}. \tag{A.4}$$

Knowing that the quaternion $\mathbf{q}$ is a unit quaternion, its inverse is equal to its conjugate $\mathbf{q}^{-1} = \mathbf{q}^*$. A rotation defined using (A.4) does not change the length of a rotated vector. It is possible to show that rotation using quaternions is mathematically identical to rotation using Euler matrices [82].

To perform an inverse rotation by the angle $-\theta$ to re-obtain the initial position, it is enough to swap the rotation quaternion with its inverse

$$(0,\ \mathbf{v}) = \mathbf{q}^{-1} \cdot (0,\ \mathbf{v}') \cdot \mathbf{q}. \tag{A.5}$$

### A.2.3 Example: Geocentric to Canonic Ellipsoid Coordinates

The specific problem of transforming a geocentric geographical rectangular coordinate system to a system bound for an ellipsoid using quaternions becomes relatively simple. The native ellipsoid system has defined as the positive direction of the $x'$-axis, the line connecting the center of the ellipsoid with one of the foci (R). Let the coordinates of that focus in the geocentric coordinates be $(x_R,\ y_R,\ z_R)$ and the coordinates of the ellipsoid center be $(x_C,\ y_C,\ z_C)$. We can introduce quaternions describing these two points as $\mathbf{q_R} = (0,\ x_R,\ y_R,\ z_R)$ and $\mathbf{q_C} = (0,\ x_C,\ y_C,\ z_C)$

The coordinate transformation can be done in two steps: firstly, the origin will be translated into the center of the ellipse, and then, the rotation to adjust $x$-axes will be performed. The translation of the coordinates is done by simple subtraction

$$\mathbf{p}' = \mathbf{p} - \mathbf{q_C},$$

where $\mathbf{p}$ and $\mathbf{p}'$ are the quaternion before and after the translation.

The angle between the vector connecting the origin with the point $(x_R,\ y_R,\ z_R)$, and the positive direction of the $x$-axis is

$$\alpha = \arccos\left(\frac{x_R}{\sqrt{x_R^2 + y_R^2 + z_R^2}}\right).$$

Thus, the rotation has to be done about a vector $\mathbf{n}$ normal to the plane defined by the $x$-axis and the vector $(x_R,\ y_R,\ z_R)$. The normal can be calculated using a simple vector product

$$\mathbf{n} = (x_R,\ y_R,\ z_R) \times (1,\ 0,\ 0) = (0,\ z_R,\ -y_R).$$

The rotational quaternion $\mathbf{q}$ is

$$\mathbf{q} = (\cos\frac{\alpha}{2},\ 0.0,\ \frac{z_R}{\sqrt{y_R^2 + z_R^2}}\sin\frac{\alpha}{2},\ \frac{-y_R}{\sqrt{y_R^2 + z_R^2}}\sin\frac{\alpha}{2}).$$

The rotation of a quaternion $\mathbf{p}'$ into ellipsoid coordinates is written as

$$\mathbf{p}'' = \mathbf{q}\mathbf{p}'\mathbf{q}^{-1}.$$

# Appendix B

# The Orbital Equation

In this appendix, the equation for the orbit of a celestial body found in the gravity field of a more massive body will be derived. The final goal is to calculate parameters of the meteoroid when only one point on the orbit, and the velocity vector at that point, are known.

The problem of predicting the motion of a body under the influence of a gravitational force due to the existence of some other body was solved by Isaac Newton more than three centuries ago. Starting with Newton's laws and knowing the expression for the force of gravity, Newton was able to solve the diferential equations of motion and obtain the equation of orbit. The final confirmation of his theory came after comparing calculated planet positions with observed ones. He confirmed and slightly modified Kepler's three famous laws [92]. In this section, the basic equations of planetary motion will be derived.

Keplerian motion, or Kepler's problem, describes the central motion of a body under the influence of a force with intensity inversely proportional to the square of the distance to the center of the force [79]. In the general case, the classical equation of motion for a body with mass $m$ in any particular set of coordinates is

$$m\frac{d^2\mathbf{r}_{0B}}{dt^2} = \sum_{i=1}^{n}\mathbf{F}_i,$$

where $\mathbf{r}_{0B}$ is a vector describing the position of the observed body with respect to the origin, and $\mathbf{F}_i$ $i = 1...N$, are all the forces acting on the body.

For the purpose of calculating the orbit of a celestial body inside the Solar System, we can assume that the Solar System is an isolated system where all external forces, such as gravitational forces due to the existence of other stars inside the Milky Way, can be neglected. In addition, one can neglect all non-gravitational forces inside the Solar system. This approximation is not completely valid since effects such as the influence of the solar wind should be included in models trying to describe the long-term motion of small celestial bodies. The differential equation of motion taking into account only gravitational forces inside the Solar System can be written as

$$m\frac{d^2\mathbf{r}_{0B}}{dt^2} = -G\frac{mM}{r_{BS}^3}\mathbf{r}_{BS} + \sum_{i=1}^{n} G\frac{mm_i}{r_{Bi}^3}\mathbf{r}_{Bi}. \tag{B.1}$$

Here $G = 6.673 \times 10^{-11}\frac{Nm^2}{kg^2}$ is the Gravitational constant, $M$ is the mass of the central body (Sun), $\mathbf{r}_{BS}$ is the vector distance from the object to the Sun, $m_i$ are the masses of the all gravitationally important objects inside the Solar System, $\mathbf{r}_{Bi}$ are vector distances from the observed body pointed toward the objects with $m_i$ (see figure B.1).

The Sun attracts the observed body with the force

$$\mathbf{F}_{BS} = -G\frac{mM}{r_{BS}^3}\mathbf{r}_{BS},$$

while the Sun is attracted by the body with the force of the same intensity but the opposite direction

$$\mathbf{F}_{SB} = G\frac{mM}{r_{BS}^3}\mathbf{r}_{BS}.$$

The gravitational force due to the Sun is usually much bigger then the sum of all other forces $\mathbf{F}_{BS} \gg \sum_{i=1}^{n} G\frac{mm_i}{r_{Bi}^3}\mathbf{r}_{Bi}$, unless the distance from the observed body to some other member of the Solar System is small enough to compensate for the effect. For simplicity, we will consider the approximation where $\mathbf{F}_{BS}$ is larger than the sum of all other forces. The correction is addressed in section B.4. The equation of motion for the tested body becomes

$$\frac{d^2\mathbf{r}_{0B}}{dt^2} = -G\frac{M}{r_{BS}^3}\mathbf{r}_{BS}. \tag{B.2}$$

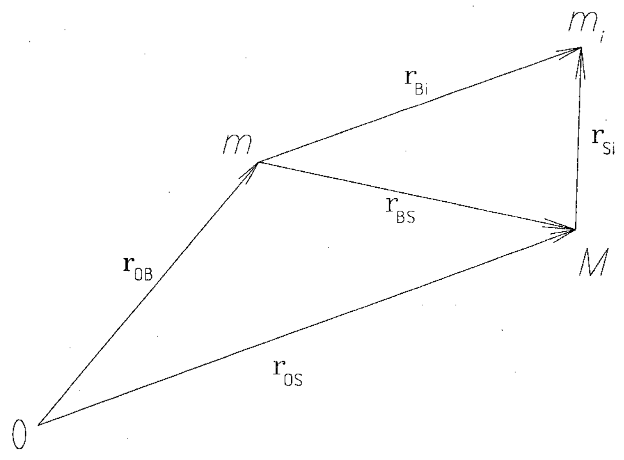

Figure B.1: Definition of the basic elements for the creation of the differential equations of motion for an object with mass $m$ in the gravity field of objects with masses $M$ and $m_i$. O represents the origin of the coordinate system.

Let a vector $\mathbf{r}_{OS}$ define the position of the center of the Sun in a coordinate system with the origin set at the center of mass (baricenter). All coordinate systems with their origin at the baricenter are inertial systems. In a two-body case, the distance from the Sun to the baricenter is

$$r_{OS} = \frac{r_{BS}}{1 + \frac{M}{m}},$$

where $r_{BS}$ is the distance between the Sun and the body of mass $m$. Since the mass of the Sun is much higher then the mass of the Earth, the baricenter is only $\sim$ 450 km away from the center of the Sun.

The equation of motion for the Sun due to the influence of the tested body in baricentric coordinates is

$$\frac{d^2\mathbf{r}_{0S}}{dt^2} = G\frac{m}{r_{BS}^3}\mathbf{r}_{BS}. \tag{B.3}$$

Subtracting (B.2) from (B.3) and knowing that $\mathbf{r}_{0S} = \mathbf{r}_{0B} + \mathbf{r}_{BS}$, we obtain

$$\frac{d^2\mathbf{r}_{BS}}{dt^2} = -G\frac{m+M}{r_{BS}^3}\mathbf{r}_{BS}. \tag{B.4}$$

A constant

$$K = G\,(M + m)$$

and a vector $\mathbf{r} = -\mathbf{r}_{BS}$ can be introduced for the sake of simplicity. The mass $m$ is in the case of meteoroids much smaller than the mass of the Sun, and in principle can be neglected. The equation (B.4) can be rewritten as

$$\frac{d^2\mathbf{r}}{dt^2} + \frac{K}{r^3}\mathbf{r} = 0. \tag{B.5}$$

Similarly, it can be shown that in the general case, the equation of motion including the external center of gravity forces (B.1) written in the coordinate system bound to the baricenter is

$$\frac{d^2\mathbf{r}}{dt^2} = -G\frac{M+m}{r^3}\mathbf{r} + \sum_{i=1}^{n} Gm_i\left(\frac{\mathbf{r}_{Bi}}{r_{Bi}^3} - \frac{\mathbf{r}_{Si}}{r_{Si}}\right). \tag{B.6}$$

The equation of motion (B.5) can be solved either using vector algebra or by direct integration. I have decided to use vector algebra in order to clearly show that planet motion around the Sun happens inside a constant plane. A good choice of a coordinate system for discussing motion inside an orbital plane is a cylindrical coordinate system. For the direct integration technique, a good reference is Wikipedia's article on Kepler's laws of planetary motion [150], as well as the more general approach in the excellent textbook of classical physics by Milić, 1997 [79].

### B.1.1 Kepler's Second Law

Multiplying (B.5) by $\mathbf{r}$,

$$\mathbf{r} \times \frac{d^2\mathbf{r}}{dt^2} + \mathbf{r} \times \frac{K}{r^3}\mathbf{r} = 0,$$

and using

$$\mathbf{r} \times \mathbf{r} = 0$$

$$\frac{d}{dt}\left(\mathbf{r} \times \frac{d\mathbf{r}}{dt}\right) = \frac{d\mathbf{r}}{dt} \times \frac{d\mathbf{r}}{dt} + \mathbf{r} \times \frac{d^2\mathbf{r}}{dt^2}$$

one can see that

$$\frac{d}{dt}\left(\mathbf{r}\times\frac{d\mathbf{r}}{dt}\right)=0.$$

Defining the velocity vector of the orbital motion as the time derivative of the position vector $\mathbf{v}=\frac{d\mathbf{r}}{dt}$, the previous equation gives us

$$\mathbf{r}\times\mathbf{v}=\mathbf{C}_1, \tag{B.7}$$

where $\mathbf{C}_1$ is a constant vector for any point on the orbit. The important conclusion is that the orbital motion is bound to a single plane. With $\mathbf{r}$ and $\mathbf{v}$ the orbital plane is completely defined in space. Knowing the orbital plane, the problem of defining an orbit becomes two dimensional: a coordinate system with its center at the baricenter and $x$ and $y$-axes in the orbital plane can be introduced. The cylindrical coordinates can be written as

$$x=r\cos\theta$$

$$y=r\sin\theta$$

$$z=z.$$

The equation of motion (B.5) in cylindrical coordinates can be written in the form of three scalar equations. It can be shown that the product

$$r^2\frac{d\theta}{dt}=C_1 \tag{B.8}$$

is a constant with a value $C_1=|\mathbf{C}_1|$. A direct consequence of this equation is that if the object is closer to the center of gravity, then its angular velocity will be higher.

The area $ds$ which the position vector $\mathbf{r}$ sweeps out in time $dt$ defined by the angle $d\theta$ is

$$\frac{ds}{dt}=\frac{1}{2}r^2d\frac{\theta}{dt}=\frac{1}{2}C_1. \tag{B.9}$$

Equation (B.7) represents Kepler's well known 2nd law. It shows that orbital motion happens inside a constant plane, with the baricenter in the plane. The constant vector

$\mathbf{C}_1$ is normal to the orbital plane. In equal periods of time, a planet sweeps out equal areas according to equation (B.9).

### B.1.2 Energy Integral

To obtain the energy integral, one can take the dot product of the velocity vector $\mathbf{v} = \frac{d\mathbf{r}}{dt}$ and equation (B.5). The first term is $\frac{d\mathbf{r}}{dt} \cdot \frac{d^2\mathbf{r}}{dt^2} = \frac{1}{2}\frac{d}{dt}\left(\frac{d\mathbf{r}}{dt} \cdot \frac{d\mathbf{r}}{dt}\right)$, while the second term can be expressed as

$$\frac{K}{r^3}\frac{d\mathbf{r}}{dt} \cdot \mathbf{r} = \frac{K}{2\sqrt{(\mathbf{r}\cdot\mathbf{r})^3}}\frac{d}{dt}(\mathbf{r} \times \mathbf{r}) = \frac{d}{dt}\left(\frac{-K}{\sqrt{\mathbf{r}\cdot\mathbf{r}}}\right).$$

The dot product can be written as

$$\frac{d}{dt}\left(\frac{1}{2}\left(\frac{d\mathbf{r}}{dt} \cdot \frac{d\mathbf{r}}{dt}\right) - \frac{K}{r}\right) = 0.$$

After integration, this equation becomes the so-called energy integral

$$\frac{1}{2}v^2 - \frac{K}{r} = h. \tag{B.10}$$

Multiplying the whole energy integral by the mass $m$, it is easy to notice that the integration constant $h$ is the sum of the kinetic and potential energies of the two body system.

### B.1.3 Kepler's First Law

Let us multiply equation (B.5) by $\mathbf{C}_1$:

$$\frac{d^2\mathbf{r}}{dt^2} \times \mathbf{C}_1 + \frac{K}{r^3}\mathbf{r} \times \mathbf{C}_1 = 0. \tag{B.11}$$

Using (B.7), the first term becomes

$$\frac{d^2\mathbf{r}}{dt^2} \times \mathbf{C}_1 = \frac{d\mathbf{v}}{dt} \times \mathbf{C}_1 = \frac{d}{dt}(\mathbf{v} \times \mathbf{C}_1),$$

and the second term can be written as

$$\frac{K}{r^3}\mathbf{r} \times (\mathbf{r} \times \mathbf{v}) = \frac{K}{r^3}(\mathbf{r}\mathbf{v})\mathbf{r} - \frac{K}{r}\mathbf{v} = \frac{d}{dt}\left(\frac{K}{r}\mathbf{r}\right).$$

Finally, (B.11) becomes

$$\frac{d}{dt}(\mathbf{v}\times\mathbf{C}_1) - \frac{d}{dt}\left(\frac{K}{r}\mathbf{r}\right) = 0,$$

or

$$\mathbf{v}\times\mathbf{C}_1 - \frac{K}{r}\mathbf{r} = \mathbf{C}_2, \tag{B.12}$$

where $\mathbf{C}_2$ is a constant vector, a product of the integration. This equation is known as the Laplacian integral, and the vector constant is called the Laplace vector, or the eccentricity vector [5]. Knowing that the product $\mathbf{v}\times\mathbf{C}_1$, as well as the vector $\mathbf{r}$ are lying in the orbital plane, the constant vector $\mathbf{C}_2$ must also be part of the orbital plane. Vectors $\mathbf{C}_1$ and $\mathbf{C}_2$ are then normal to each other and their scalar product must be equal to zero

$$\mathbf{C}_1\mathbf{C}_2 = 0. \tag{B.13}$$

The relation between the intensities of the two vector constants and the energy integral $h$ can be found by taking the dot product $\mathbf{C}_2\cdot\mathbf{C}_2$ as

$$C_2^2 = 2hC_1^2 + K^2. \tag{B.14}$$

Scalar multiplication (B.12) with the vector $\mathbf{r}$ gives

$$C_1^2 - Kr = \mathbf{C}_2\mathbf{r}.$$

By introducing the angle $\varphi$ between vectors $\mathbf{C}_2$ and $\mathbf{r}$, the previous equation becomes

$$C_1^2 - Kr = C_2 r\cos\varphi.$$

When expressing the distance $r$ between the baricenter and the observed body as a function of the angle $\varphi$, the equation of orbit is

$$r = \frac{\frac{C_1^2}{K}}{1+\frac{C_2}{K}\cos\varphi}. \tag{B.15}$$

The equation of a conic section with eccentricity $e$ and parameter of the orbit $p$ is

$$r = \frac{p}{1+e\cos\varphi}. \tag{B.16}$$

Comparing the last two equations, the parameters $p$ and $e$ are

$$p = \frac{C_1^2}{K} \tag{B.17}$$

$$e = \frac{C_2}{K}. \tag{B.18}$$

The object is closest/furthest (periapsis/apoapsis) from the center of gravity when the derivative of the equation (B.16) $\frac{dr}{d\varphi}$ is zero. After taking the derivative we see that $r$ has minimal/maximal values when $\sin\varphi = 0$. By convention, the angle $\varphi$ is measured in the orbital plane from the vector $\mathbf{C}_2$ pointed toward the periapsis in the positive direction. To completely determine the orbit of a body one thus has to know the two constant vectors, $\mathbf{C}_1$ and $\mathbf{C}_2$.

Kepler's first law states that "the orbit of a planet about a star is a conical section with the star at one focus". Mathematically expressed, Kepler's first law becomes equation (B.15).

One of the properties of conic sections is the relation between the semi-major axis $a$ and the parameters $p$ and $e$:

$$p = a(1 - e^2). \tag{B.19}$$

An important consequence of Kepler's 1st law can be obtained by merging (B.14), (B.17), (B.18) and (B.19) into

$$a = -\frac{K}{2h}. \tag{B.20}$$

Thus, the semi-major axis of the conic section depends only on the energy. If the energy has negative value $h < 0$, the semi-major axis is positive $a > 0$ and the conic section is an ellipse. If $h = 0$ then $a$ must also be 0, and the trajectory is parabola. Finally, if $h > 0$, the trajectory is hyperbola with $a < 0$.

### B.1.4 Kepler's Equation

Let us assume that the orbit of the observed body (B.16) takes the shape of an ellipse. In the coordinate system native to the given ellipse with semi-axes $a$ and $b$, the equation of orbit is

$$\frac{x_1^2}{a^2} + \frac{y_1^2}{b^2} = 1.$$

In this coordinate system, the origin is at the center of the ellipse, and the $x_1$ and $y_1$ axes are directed along the principal axes of the ellipse.

Following the approach given in [21], the parametric form of the ellipse equation is

$$x_1 = a \cos E$$
$$y_1 = b \sin E = a\sqrt{1 - e^2} \sin E,$$

where the angle $E$ is measured from the $x_1$-axis toward the radius vector of the object. To switch back to the coordinate system $x - y$ centered at a focus of the ellipse, while preserving the direction of the axes, one can apply

$$x = x_1 - ae = a(\cos E - e) \tag{B.21}$$
$$y = y_1 = b \sin E. \tag{B.22}$$

The coordinates of the celestial body using polar coordinates $r$ and $\varphi$ are

$$x = r \cos \varphi \tag{B.23}$$
$$y = r \sin \varphi. \tag{B.24}$$

Combining the previous four equations, it follows that

$$r = a(1 - e \cos E). \tag{B.25}$$

Using (B.25) with (B.21), (B.23), (B.22) and (B.24), it can be shown that

$$\tan \frac{\varphi}{2} = \sqrt{\frac{1+e}{1-e}} \tan \frac{E}{2} \tag{B.26}$$
$$\cos \varphi = \frac{\cos E - e}{1 + e \cos E}. \tag{B.27}$$

To obtain the position of the body as a function of time, equation (B.9) has to be integrated. Angle $\theta$ in equation (B.9) can be replaced by angle $\varphi$, while the constant $C_1$

can be taken from (B.17) using the property of an ellipse $p = a(1 - e^2)$:

$$r^2 \frac{d\varphi}{dt} = \sqrt{K}\sqrt{a(1 - e^2)}.$$

After taking the integral of this equation and using (B.25), (B.26) and (B.27) we obtain Kepler's equation

$$E - e \sin E = \sqrt{\frac{K}{a^3}}\,(t - \tau)\,. \tag{B.28}$$

Here $\tau$ is the time constant equal to the time of the passage through the periapsis in which case the angle $E = 0$.

In the case where the trajectory follows a parabola or a hyperbola, the above discussion will hold under assumptions that some of the quantities are imaginary numbers. For more details the reader can see Dubyago, 1961 [21].

### B.1.5 Kepler's Third Law

To complete Kepler's laws, the third law can be derived from (B.9) and (B.18). The total area the vector $\mathbf{r}$ sweeps out while making a complete turn around the center of gravity can be calculated by integrating equation (B.9)

$$\int ds = \int \frac{1}{2} C_1 dt. \tag{B.29}$$

Knowing that the orbit is an ellipse, the total area of the orbit with semi-axes $a$ and $b$ is $ab\pi$. The total sidereal time needed for a body to make a complete turn is $T$. Using the property of an ellipse $p = \frac{b^2}{a}$ and equation (B.18) to eliminate $C_1$, (B.29) becomes

$$\frac{T^2}{a^3} G(M + m) = 4\pi^2. \tag{B.30}$$

Kepler's third law states that the square of the orbital period is directly proportional to the cube of the semi-major axis of the orbit, as seen in the above equation. Historically, it is interesting to note that Newton corrected Kepler's original equation by adding the small term $m$. In practice, it is possible to neglect this term if $m \ll M$.

## B.2 Orbital parameters

In the previous section, the equation of the orbit of a small body in the gravitational field of the Sun was derived. The motion is defined by a vector differential equation of second order (B.5). Solving this equation, the two constant vectors $\mathbf{C}_1$ and $\mathbf{C}_2$ appear as products of the integration. Knowing that $\mathbf{C}_1$ and $\mathbf{C}_2$ are orthogonal, we can reduce the six parameters ($C_{1,1}$, $C_{1,2}$, $C_{1,3}$, $C_{2,1}$, $C_{2,2}$, $C_{2,3}$) to the five independent components defining the orbit by using the scalar product:

$$C_{1,1}C_{2,1} + C_{1,2}C_{2,2} + C_{1,3}C_{2,3} = 0,$$

The primary choice for the origin of the coordinate system used to track the motion of celestial bodies inside the Solar System is the center of the Sun. The main coordinate plane $x - y$ is defined as the plane of the Earth's motion around the Sun – the plane of the ecliptic. The $z$-axis is then uniquely defined as a normal to the plane with the center of the Sun as zero point. The $x$-axis is defined to point toward the $\gamma$ point, i.e. the point of the spring equinox. This point represents the intersection of the two celestial circles representing the ecliptic and the equator.

The position of the vernal equinox changes in time due to various processes such as precession and nutation. To eliminate time variability, the $\gamma$ point, as well as the primary plane, have to be used for a specific epoch, for example for 2000.0. An older approach was to pick a specific star, for example Regulus, positioned relatively close to the $\gamma$ point, and use the intersection of the meridian toward Regulus with the $x - y$ plane.

In the general case, the main coordinate plane and the plane of the orbital motion are not the same. The intersection of these two planes is a line, passing through the center of the Sun, called the line of nodes. The points of intersection of the orbit with the main coordinate plane are called the node points $\Omega$ and $\mho$. The $\Omega$ node is called the ascending node, because after passing through the node, the celestial body is moving from the zone with $z < 0$ into the zone with $z > 0$. A similar analogy is valid for the descending $\mho$

node. For a graphical interpretation see Fig. B.2. When the orbit is a paraboloid or a

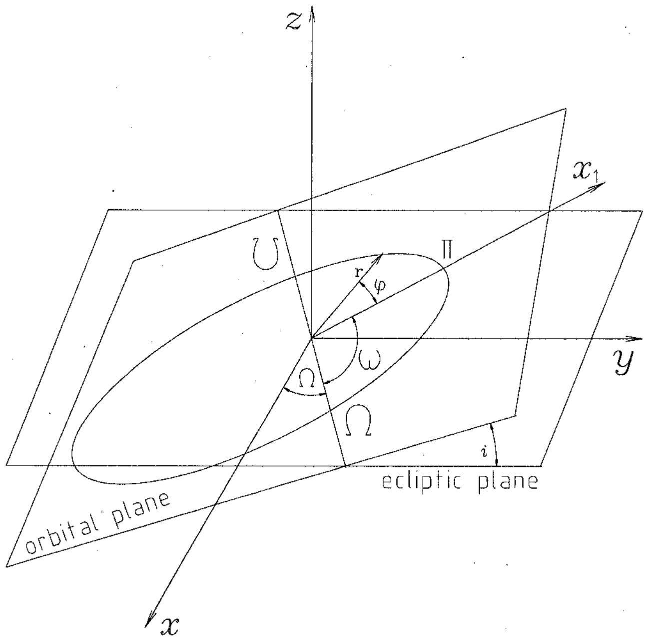

Figure B.2: Definition of the orbital parameters in rectangular heliocentric ecliptic coordinates. The $x$-axis is oriented toward the $\gamma$ point. The $x - y$ plane is the ecliptic plane. The orbital plane is defined by the angles $\Omega$ and $i$. The line of nodes is defined by the intersection of the orbital ellipse with the ecliptic plane at the points $\Omega$ and $\mho$. The $x_1$-axis lies in the orbital plane and is directed toward the periapsis $\Pi$. $\omega$ is the angle between the line of nodes and $x_1$. The observed body has position vector $\mathbf{r}$. $\varphi$ is the angle between $\mathbf{r}$ and $x_1$.

hyperboloid the intersection with the main plane consists of only one node point. If only the $\Omega$ node exists for an orbit, it can be assumed that the $\mho$ node is at infinity. The node line can also be defined using an angle $\Omega$ measured from the positive $x$-axis toward the $\Omega$ node. The angle can take values from 0 to $2\pi$. The ascending node and the angle are both traditionally named using the Greek letter $\Omega$.

The exact position of the orbital plane can be described by an inclination angle $i$

between the $z$-axis and the vector $\mathbf{n} = \frac{\mathbf{C}_1}{C_1}$ normal to the orbital plane. The vector $\mathbf{n}$ is oriented in such a way that when looking from the top of the vector, the body is moving in the direction it indicates. $i$ represents the angle between the main coordinate plane and the orbital plane. It can take values between 0 and $\pi$. When $i = 0$ or $\pi$, the angle $\Omega$ doesn't have a physical meaning and a new coordinate system is needed to describe such an orbit.

The orbit is completely defined, as already discussed in the previous subsections, if the eccentricity $e$ and the parameter $p$ are known. The position of the orbit in the orbit plane can be fixed by introducing the position of the periapsis. The periapsis is the point on the orbit where the body is closest to the center of gravity. If the central body is the Sun, periapsis is called perihelion. The position of the periapsis is specified by the argument of periapsis $\omega$, which is the angle between the node line toward the Sun and the direction of the periapsis, measured in the positive direction. It can take values from 0 to $2\pi$. The point of the farthest distance is called the apoapsis, or aphelion if the central body is the Sun. The time when an orbiting body passes through the periapsis is denoted using the Greek letter $\tau$.

The parameters $\Omega$, $i$, $e$, $p$, $\omega$ and $\tau$ define the position of a celestial body at any moment in time. To find them in practice, one has to perform a set of coordinate transformations starting with some given initial conditions, such as the position of the observed body at three different times, or the position and the velocity vector of the body at a given epoch.

### B.2.1 Determination of Orbital Parameters from Initial Conditions

Assume that a position $\mathbf{r}$ and a velocity $\mathbf{v}$ of a body orbiting the Sun at time moment $t$ is given by rectangular heliocentric ecliptic coordinates $(x,\ y,\ z)$. The first constant of integration, $\mathbf{C}_1$, and the unity vector normal to the orbital plane, $\mathbf{n}$, can be calculated using equation (B.7)

$$\mathbf{C}_1 = \mathbf{r} \times \mathbf{v}$$
$$\mathbf{n} = \frac{\mathbf{C}_1}{C_1}.$$

The orbital plane is completely determined by the two angles $\Omega$ and $i$. The unity vector $\mathbf{n}$ has the following components in rectangular heliocentric ecliptic coordinates $(x,\ y,\ z)$:

$$\mathbf{n} = \begin{bmatrix} \sin\Omega \sin i \\ -\cos\Omega \sin i \\ \cos i \end{bmatrix}.$$

If $\sin i \neq 0$, the angles $\Omega$ and $i$ can be uniquely calculated using the above vector equations.

The parameter $p$ can be calculated from (B.17) and the eccentricity $e$ from (B.18) via the second constant of integration $\mathbf{C}_2$. From equation (B.12) follows

$$\mathbf{C}_2 = \mathbf{v} \times \mathbf{C}_1 - \frac{K}{r}\mathbf{r}. \tag{B.31}$$

The orbital parameter $p$ is given in (B.17).

The unity vector defining the node line has the rectangular heliocentric ecliptic coordinates $\mathbf{l} = (\cos\Omega,\ \sin\Omega,\ 0)$, and the direction toward the periapsis is defined by the vector $\mathbf{C}_2$. The angle between the two vectors can be calculated from the scalar and vector products:

$$\cos\omega = \frac{\mathbf{l} \cdot \mathbf{C}_2}{C_2} = \frac{C_{2x}\cos\Omega + C_{2y}\sin\Omega}{C_2},$$
$$\sin\omega = \frac{\mathbf{C}_1 \cdot (\mathbf{l} \times \mathbf{C}_2)}{C_1 C_2}.$$

In the expression for $\sin\omega$, the dot product with vector $\mathbf{C}_1$ is used to properly carry the sign.

The time of the passage through perihelion $\tau$ can be found from Kepler's equation (B.28)

$$E - e\sin E = \sqrt{\frac{K}{a^3}}\,(t - \tau)\,, \tag{B.32}$$

using the eccentric anomaly $E$ defined in (B.25) and the semi-major axis $a$ from equation (B.19).

### B.2.2 Determination of the Position from Orbital Elements

In this subsection a method for finding the position of the celestial body at a given instance of time $t$ from the elements of the orbit is presented. The position will be given in rectangular heliocentric coordinates. Let us assume that the parameters $\Omega$, $i$, $e$, $p$, $\omega$ and $\tau$ are known.

First, the eccentric anomaly, $E$, has to be found from equation (B.32). The angle $\varphi$ follows from (B.26), and $r$ from (B.16). $r$ and $\varphi$ define the position of the given object in the orbital plane (Fig. B.2):

$$\mathbf{r} = \begin{bmatrix} r\cos\varphi \\ r\sin\varphi \\ 0 \end{bmatrix}. \tag{B.33}$$

To obtain the rectangular orbital plane from the heliocentric ecliptic coordinates, the ecliptic coordinate system has to be rotated by an angle $\Omega$ about the $z$-axis, an angle $i$ about the new $x$-axis, and then by the angle $\omega$ about the new $z$-axis. This transformation can be represented by a quaternion $\mathbf{Q}$ composed of three quaternions corresponding to the three rotations

$$\mathbf{Q} = \begin{bmatrix} \cos\frac{\omega}{2} \\ 0 \\ \sin\frac{\omega}{2} \\ 0 \end{bmatrix} \begin{bmatrix} \cos\frac{i}{2} \\ \sin\frac{i}{2} \\ 0 \\ 0 \end{bmatrix} \begin{bmatrix} \cos\frac{\Omega}{2} \\ 0 \\ 0 \\ \sin\frac{\Omega}{2} \end{bmatrix} \tag{B.34}$$

In this case we need the inverse transformation, so the transformation of some vector $\mathbf{r}$ from the rectangular orbital plane to the heliocentric ecliptic coordinates will be

$$(0,\ \mathbf{r}') = \mathbf{Q}^{-1} \times (0,\ \mathbf{r}) \times \mathbf{Q} \tag{B.35}$$

## B.3 Calculation of Orbital Parameters Based on Observations

For the practical calculation of the orbital parameters of any celestial body, one has to start with observed data. If an observer measures the position and the velocity of the body at some time $t_1$ in any local coordinate system, such data can always be rewritten in a coordinate system with the origin at the center of the gravity field, ie. at the center of the Sun. This is preferable since any local coordinate system is time dependent: a location on the Earth's surface follows day-night rotation, as well as the revolution of the Earth around the Sun. Motion of the Solar System as a whole can be neglected for observations of objects inside the Solar System.

The most convenient coordinate system used to define the observed position of a meteoroid is the universal equatorial coordinate system. There is a difference between the universal and local equatorial systems: in the former, the positions of stars stay fixed in time, while in the latter this is not the case. The Earth's polar axis is used as a $z$-axis for any equatorial system because it is a fixed line with respect to the Earth's rotation. The basic plane is defined as the equatorial plane. Each point on the equatorial plane is moving due to Earth's rotation.

A coordinate system static with respect to the rotation might be defined using a point on the equatorial plane following the Earth's rotation. A convenient choice is the vernal or spring equinox point ($\gamma$). Thus, a position on the sky can be determined by using two angles: the declination angle $\delta$ and right ascension $\alpha$. The declination angle $\delta$ measures the position between the object and the celestial equator and it can take values from $-90°$ to $90°$. The right ascension $\alpha$ is the angle measured on the equatorial plane from the direction toward the $\gamma$ point to the foot of the hour circle passing through the object. It takes values from $0°$ to $360°$.

Switching from any local coordinates to the equatorial coordinate system in which stars have fixed coordinates (universal equatorial system) can be done by first transforming the initial local coordinates (for example horizontal) to the equatorial coordinates moving with the Earth. A celestial object in this system moves in the opposite direction with respect to the Earth's rotation along a small circle defined with constant declination. After a period of one sidereal day (23h 56m 4.091s), the object will pass through the same point. The position of a celestial object in this system is described by declination and the longitudinal angle called the hour angle $t_H$. The great circle where $t_H = 0$ is called the local meridian. By this definition, a celestial object has a constant right ascension $\alpha$, but its hour angle $t_H$ changes with time. $t_H$ will change for the same interval as the elapsed star or sidereal time $s_t$. Sidereal time is measured as an hour angle of the $\gamma$ point. $s_t = 0$ is when the vernal equinox $\alpha = 0$ crosses the local meridian $t_h = 0$. The relation between sidereal time, right ascension and the hour angle is

$$s_t = \alpha + t_h \tag{B.36}$$

### B.3.1 Local to Universal Equatorial Coordinates

The equatorial coordinates moving with the Earth used in this thesis are the projected geographic coordinates. Each point has a geographical longitude $\lambda$ taking values from the interval $[0°,\ 360°)$, a latitude $\varphi$ with values $[-90°,\ 90°]$, and a distance from the origin $r$. As in any equatorial coordinate system, the origin is at the center of Earth, the $z$-axis points toward the celestial north pole, and $x - y$ is the Earth's equatorial plane, with the $x$-axis pointing toward the Greenwich meridian. The reader should notice a difference between the local coordinates used here and the standard local equatorial coordinates used in astronomy.

The standard astronomical definition (see for example [122]) assumes that the $x$-axis is pointed toward the intersection of the equator with the meridian passing through the north celestial pole. A direct consequence of such a definition is that each place on Earth will have a different local coordinate system. The sidereal time in the place of observation is different for different geographic longitudes. The connection between different local equatorial systems used in astronomy is given by equation (B.36). In this thesis we have decided to use the Greenwich meridian to define the $x$-axis.

The declination ($\delta$) coordinate of the universal equatorial system ($\alpha$, $\delta$, $r$) will have the same value as the geographic latitude ($\varphi$) of our local equatorial system ($\lambda$, $\varphi$, $r$):

$$\delta = \varphi,$$

while the right ascension $\alpha$ is the sum of the sidereal time of the zero (Greenwich) meridian $GMST$ and the geographic latitude.

$$\alpha = GMST + \lambda$$

Mathematically, this coordinate transformation is the rotation for an angle $GMST$ about the Earth's polar axis i.e. the $z$-axis.

The changes in position of the vernal equinox, as well as the changes of the rotation axis of Earth in time, cause the equatorial system to change in time. To cope with these changes an epoch for which the coordinates are given should be provided. At the time of writing the epoch 2000.0 is used.

### B.3.2 Sidereal Time at Greenwich

The Greenwich Mean Sidereal Time $GMST$ defines a global standard of sidereal time. It is a sidereal time at the meridian of Greenwich. The International Astronomical Union adopted in 1982 a formula to calculate $GMST$ at $0^h$ UT [75]:

$$GMST_0 = 100.46061837 + 36000.770053608T + 0.000387933T^2 - \frac{T^3}{38710000},$$

where $T$ is directly dependent on the Julian Day $JD_0$ corresponding to the given date at $0^h$ UT

$$T = \frac{JD_0 - 2451545}{36525}.$$

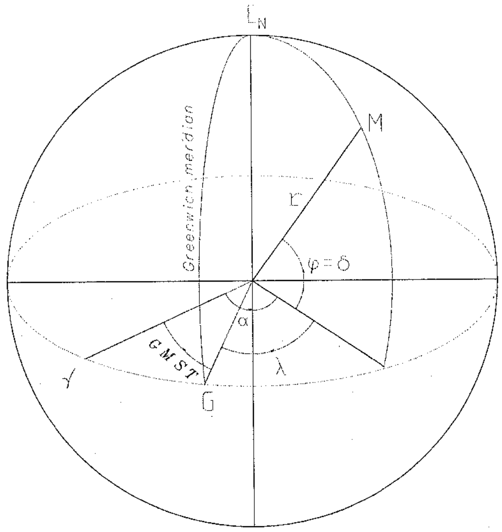

Figure B.3: Transformation of local geographical equatorial coordinates ($\lambda$, $\varphi$) into universal equatorial coordinates ($\alpha$, $\delta$). $E_N$ is pointed toward the north pole, $\gamma$ is the vernal equinox point, $G$ is defined as an intersection point of the equator and the ecliptic, and $M$ is the position of the observed object.

The Julian Day is the number of days elapsed between the beginning of the year -4712 and a given date. It begins at Greenwich mean noon, at $12^h$ UT. The algorithm for calculating $JD_0$ is given in [75]. For a given date in the Gregorian calendar written in the form $Y\ M\ D$:

- if $M <= 2$ then $Y \Longrightarrow Y - 1$; $M \Longrightarrow M + 12$;
- $A =$integer$(\frac{Y}{100})$; $B = 2 - A+$integer$(\frac{A}{4})$
- $JD_0 =$integer$(365.25(Y + 4716))+$integer$(30.6001(M + 1)) + D + B - 1524.5$

where integer() values are truncated, not rounded.

In the case of the Greenwich mean sidereal time for any instant $t_{UT}$ of UT for a given date, $GMST_0$ has to be modified as

$$GMST = GMST_0 + t_{UT} * 1.00273790935. \tag{B.37}$$

$GMST$ can also be calculated directly at the cost of losing numerical precision using

$$GMST = 280.46061837 + 360.98564736629(JD - 2451545.0) + 0.000387933T^2 - \frac{T^3}{38710000},$$

where $JD$ is the total time elapsed and not only the number of elapsed days

$$JD = JD_0 + t_{UT}.$$

A more precise algorithm for calculation of $GMST$ is given in [17].

### B.3.3 Universal Equatorial to Ecliptic Coordinates

The needed orbital parameters are measured in a coordinate system centered on the Sun, and the main plane is defined as the plane in which the Earth orbits the Sun for a certain epoch. The angle between the planes of the equator and the ecliptic is denoted by the Greek letter $\epsilon$. It is changing with time, and has value of approximately 23° (see table B.1) for the current epoch.

The base direction of the geocentric ecliptic coordinates is the $x$-axis which is directed toward the $\gamma$ point. The $z$-axis is the polar axis rotated by the angle $\epsilon$ about the $x$-axis. A position in geocentric ecliptic coordinates is measured using ecliptic longitude $\lambda$ and latitude $\beta$ in the same way as $\alpha$ and $\delta$ are measured inside the universal equatorial system. One should make a clear difference with the $\lambda$ used to denote geographical longitude.

The standard astronomical equations for the transformation of geocentric equatorial coordinates to geocentric ecliptic coordinates [36] are:

$$\cos\lambda\cos\beta = \cos\delta\cos\alpha$$

$$\sin\lambda\cos\beta = \cos\delta\sin\alpha\cos\epsilon + \sin\delta\sin\epsilon$$

$$\sin\beta = -\cos\delta\sin\alpha\sin\epsilon + \sin\delta\cos\epsilon.$$

The inverse transformations are given by:

$$\cos\alpha\cos\delta = \cos\beta\cos\lambda$$

$$\sin\alpha\cos\delta = \cos\beta\sin\lambda\cos\epsilon - \sin\beta\sin\epsilon$$

$$\sin\delta = \cos\beta\sin\lambda\sin\epsilon + \sin\beta\cos\epsilon.$$

To perform a transformation from geocentric to heliocentric coordinates, the position of the Sun must be known. One of the simplest algorithms for finding the coordinates of the Sun is given in [85] and [134]. It provides numerical accuracy of about 1 arc min. Due to the algorithm's simplicity, it will be used only as a starting point to test the basic principles. One interesting and original attempt to find the parameters of the Earth's orbit was made by Rees, 1991, but his results carry relative errors of a few percent [110].

### B.3.4 Coordinates of the Sun

In the simplest, but still usable approach, the ecliptic $(l_S, b_S, r_S)$ and equatorial $(\alpha_S, \delta_S)$ coordinates of the Sun at Julian Date JD of Universal Time (UT) can be approximated using the following equations [85]:

- $D = JD - 2451545.0$;
- $g = 357.529 + 0.98560028D$ (in degrees);
- $q = 280.459 + 0.98564736D$ (in degrees);
- $l_S = q + 1.915\sin g + 0.020\sin 2g$ (in degrees);
- $b_S = 0$ (in degrees);
- $r_S = 1.00014 - 0.01671\cos g - 0.00014\cos 2g$ (in AU);
- $\epsilon = 23.439 - 0.00000036D$ (in degrees);

Using the transformations from geocentric ecliptic to equatorial coordinates, the solar right ascension and declination can be calculated as

- $\sin \alpha_S = \cos \epsilon \sin l_S$;
- $\cos \alpha_S = \cos l_S$;
- $\sin \delta_S = \sin \epsilon \sin l_S$.

For higher accuracy, the algorithm VSOP87 can be used [7], [8]. The full version of the VSOP87 algorithm uses 2425 periodic terms to compute the Solar ephemeris. The maximum error in astronomical longitude does not exceed 0.01 arc seconds. This algorithm also calculates the latitude of the Sun which can be different from zero.

With the known coordinates of the Sun, a transformation from universal equatorial to heliocentric ecliptic coordinates can be done by first performing a rotation for the angle $\epsilon$ about the $x$-axis (pointed toward the $\gamma$ point) to the geocentric ecliptic coordinates, and then performing the transformation to the heliocentric system.

### B.3.5 Apex Position and Earth's Heliocentric Velocity Vector

Conversion of the velocity vector from the geocentric to heliocentric coordinates is straightforward if the Earth's velocity vector at the given time is known. The Earth's velocity vector is completely defined by the position of the point on the celestial sphere toward which the orbital motion of the Earth is directed (apex), and the intensity of the velocity vector. Assuming that the Earth's orbit is a perfect circle, then the geocentric ecliptical coordinates of the apex $(l_\alpha,\ b_\alpha)$ are

$$l_\alpha = l_S - 90^\circ,$$

$$b_\alpha = 0^\circ.$$

The procedure of obtaining the geocentric ecliptic coordinates of the Sun $(l_S,\ b_S)$ was discussed above.

In reality, the coordinates of the apex are going to be slightly changed due to the eccentricity of the orbit. The corrected equation for the apex position can be found by taking the derivatives of the rectangular components of the Earth's position in the heliocentric ecliptical coordinate system $(x_E,\ y_E,\ z_E = 0)$ :

$$\frac{d}{dt}x_E = \frac{d}{dt}\left(r_E \cos l_E\right),$$
$$\frac{d}{dt}y_E = \frac{d}{dt}\left(r_E \sin l_E\right).$$

$r_E = r_S$ and $l_E = l_S - 180°$ are the Earth-Sun distance and the longitude of the Earth, respectively. The expressions for the components of the velocity vector can be written using the coordinates of the apex and the tangential component of the Earth's velocity $v_t$ via

$$\frac{d}{dt}x_E = v_t \cos l_\alpha,$$
$$\frac{d}{dt}y_E = v_t \sin l_\alpha.$$

Following the approach in [21], after combining the previous 4 equations,

$$v_t \sin(l_\alpha - l_S) = -r_E \frac{dl_S}{dt},$$
$$v_t \cos(l_\alpha - l_S) = -\frac{dr_E}{dt}.$$

These two equations can be divided to obtain the cotangent of the angle difference $l_\alpha - l_S$:

$$\cot(l_\alpha - l_S) = \frac{1}{r_E}\frac{dr_E}{dl_S}. \tag{B.38}$$

Kepler's first law can then be used to calculate the derivative of the Earth's radii:

$$\frac{dr_E}{dl_S} = \frac{d}{dl_S}\left(\frac{p}{1 - e\cos(l_S - l_\pi)}\right),$$

where $e = 0.016710219$ is the eccentricity of the Earth's orbit and $l_\pi$ is the longitude of the Earth's perihelion for the equinox at the beginning of the year of the observation $(t_Y)$, given by the formula

$$l_\pi = 102°5' + 1'03(t_Y - 1950). \tag{B.39}$$

(B.38) becomes

$$\cot(l_\alpha - l_S) = -e\sin(l_S - l_\pi).$$

The difference $l_\alpha - l_S$ is approximatly equal to 90°, so a first order Taylor expansion can be used to finally obtain the longitude of the apex:

$$l_\alpha = l_S - 90^\circ + \frac{e}{\tan 1'}\sin(l_S - l_\pi). \tag{B.40}$$

Many authors disregard this correction since the Earth's orbit is nearly circular. The Sun-Earth distance, which is maximal when the Earth is at aphelion, and minimal when the Earth is at perihelion, changes only by about 3%.

Usually, in meteor-related literature, the intensity of the Earth's velocity vector is determined using the energy integral (B.10). The constant $h$ can be found from the position and velocity at some particular point in the orbit

$$h = \frac{1}{2}v^2 - \frac{K}{r}. \tag{B.41}$$

If the Earth's velocity is about 30 km/s (see Table B.1), the kinetic energy term is approximatevely $4.5 \times 10^8\ \mathrm{m}^2/\mathrm{s}^2$.

For an elliptic orbit, the specific orbital energy simplifies to

$$h = -\frac{K}{2a}, \tag{B.42}$$

and in the case of a hyperbolic orbit it is

$$h = \frac{K}{2a}. \tag{B.43}$$

It was already mentioned that for a parabolic orbit $h = 0$.

Combining (B.41) and (B.42) gives the velocity of an object at a distance $r$ from the baricenter moving on an elliptic trajectory around the center of gravity:

$$v = \sqrt{K\left(\frac{2}{r} - \frac{1}{a}\right)}. \tag{B.44}$$

| | | |
|---|---|---|
| Orbital eccentricity | $e_E$ | 0.016710219 |
| Average orbital speed | $v_E$ | 29.783 km/s |
| Longitude of the ascending node | $\Omega_E$ | 348.73936° |
| Argument of the perihelion | $\omega_E$ | 114.20783° |
| Semi-major axis | $a_E$ | $149.5978875 \times 10^9$ m |
| Semi-minor axis | $b_E$ | $149.5769998 \times 10^9$ m |
| Distance to aphelion | $r_\alpha$ | $152.097701 \times 10^9$ m |
| Distance to perihelion | $r_\pi$ | $147.098074 \times 10^9$ m |
| Orbital inclination to ecliptic | $i$ | 0.00005° |
| Sidereal orbit period | $T_E$ | 365.256366 days |
| Mass of the Sun | $M_S$ | $1.98892 \times 10^{30}$ kg |
| Mass of the Earth | $m_E$ | $5.9736 \times 10^{24}$ kg |
| Gravity constant | $G$ | $6.672 \times 10^{-11}$ Nm$^2$/kg$^2$ |
| Obliquity of the ecliptic | $\epsilon$ | 23.4392911° |

Table B.1: Characteristics of Earth's orbital motion for the epoch J2000, and other constants important for orbit calculations.

A similar expression can be derived for the case of hyperbolic motion, where the minus sign becomes a plus.

The position of the Earth orbiting the Sun at any instant is given in terms of the distance to the Sun and the angle $\varphi$ measured from the Sun-aphelion line to the vector position $\mathbf{r}_E$. In the rectangular heliocentric ecliptic system, the vector $\mathbf{r}_E$ is (B.33):

$$\mathbf{r}_E = r_E \cos\varphi_E \mathbf{i} + r_E \sin\varphi_E \mathbf{j}.$$

The time derivative of the position vector leads to the equation for the velocity vector.

$$\frac{d\mathbf{r}_E}{dt} = \left(\frac{dr_E}{dt}\cos\varphi_E - r_E\sin\varphi_E\frac{d\varphi_E}{dt}\right)\mathbf{i} + \left(\frac{dr_E}{dt}\sin\varphi_E + r_E\cos\varphi_E\frac{d\varphi_E}{dt}\right)\mathbf{j}.$$

Kepler's first equation (B.16) has $r_E$ defined using the parameters $p_E$ and $e_E$. The time derivative of (B.16), is

$$\frac{d\mathbf{r}_E}{dt} = \left(\frac{e_E\sin\varphi_E}{p_E}\right) r_E^2 \frac{d\varphi_E}{dt}.$$

Using the time derivative $\frac{d\varphi_E}{dt}$ given in the Kepler's second law (B.9), the Earth's velocity vector is

$$\mathbf{v}_E = \sqrt{\frac{K}{p_E}}\left[-\sin\varphi_E\mathbf{i} + (e_E + \cos\varphi_E)\mathbf{j}\right]. \tag{B.45}$$

The velocity has the highest value when the Earth is at aphelion of the orbit since $\varphi_E = 0$. It is also obvious from (B.45) that at perihelion and aphelion, only the $j$ component is nonzero, and thus the velocity vector is normal to the position vector.

The angle $\varphi_E$ is measured in the plane of the ecliptic, from the aphelion toward the vector $\mathbf{r}_E$. The longitude of the perihelion point for the beginning of the observation year is given in (B.39). The longitude of the Earth is $l_E = l_S - 180°$, where the longitude of the Sun is calculated via the algorithm given in subsection B.3.4. $\varphi_E$ is then

$$\varphi_E = l_S - l_\pi. \tag{B.46}$$

### B.3.6 The Transformation Algorithm: Summary

- Start with observed $i = 1, ...N$ points in geographic coordinates $(\lambda_i,\ \varphi_i,\ r_{GCi},\ UT_i)$;
- Find $GMST_i$ for the given $UT_i$ using (B.37);
- Form position quaternion by switching to rectangular coordinates (see appendix A;
- Transformation to universal equatorial coordinates by rotating about $z$-axis for angle GMST (see subsection B.3.1);
- Find geocentric ecliptic coordinates of the Sun (see section B.3.4);
- Rotate the quaternions about the $x$-axis by the angle $\epsilon$ (see appendix A);
- Translate the quaternions to set the origin at the center of the Sun (see subsection B.3.4);
- Determine the Earth's velocity and use it to find the velocity of the object in the heliocentric system (see subsection B.3.5);
- Find the orbital parameters (see subsection B.2.1).

## B.4 Corrections for a Meteoroid's Orbit

In the previous section, a method for calculating the orbital elements of a body in the gravitational field of the Sun was explained. The calculation was done based on the assumption that the only important force acting on the observed body is the gravitational force of the Sun. It was also assumed that the observed data had already been reduced and that all necessary corrections were done. In this section three needed corrections will be discussed. We will start with the velocity corrections due to atmospheric drag. Next, an analysis of the influence of the Earth's rotation on the measurement of the velocity vector of a meteoroid will be given. At the end of the section, the perturbations due to the gravity field of the Earth will be discussed.

### B.4.1 Velocity Correction due to Air Resistance

Friction between a meteoroid and the atmosphere forces the meteoroid to slow down. As the meteoroid loses altitude, the air resistance increases, manifesting itself as higher velocity loss. The initial velocity of meteoroids is in the range of 10 – 80 km/s, while the thermal velocity of the air molecules is only $\sim 0.5$ km/s. The thermal velocity of the air molecules is usually considered to be negligibly low. The atmospheric density $\rho$ is exponentially dependent on the height $h$ as shown in

$$\rho = \rho_0 e^{\frac{-h}{h_0}}, \tag{B.47}$$

where $h_0$ is the scale height expressed using the gas constant $R$, the absolute temperature $T$, the molecular weight $\mu$ of the air, and gravity constant $g$ as:

$$h_0 = \frac{RT}{\mu g}. \tag{B.48}$$

The drag equation of motion includes the central force (gravity) and the drag force proportional to the velocity vector. It is described by

$$\frac{d^2\mathbf{r}}{dt^2} = -K\frac{\mathbf{r}}{r^3} - \Gamma S\rho\frac{dr}{dt}\frac{d\mathbf{r}}{dt}, \tag{B.49}$$

where $\Gamma$ is the drag coeficient, expressing the portion of the momentum of the oncoming flow that is converted into the deceleration of the meteoroid. It can typically take a value between 0.5 to 1. $S$ is the midsectional area of the meteoric body.

A velocity correction for the drag can be derived from the equations for the velocity and deceleration of the physical theory of meteors [9]. The derivation of this correction is explained in detail in Katasev, 1964 [59] under the assumption that all meteoroids have roughly the same density and that the ablation forces exceed the gravitational force acting on the meteoric body. The velocity of the meteoroid before entering the atmosphere $v_\infty$ is

$$v_\infty = v_0 \left[1 - h_0 \frac{\left(\frac{dv}{dt}\right)_0}{v_0^2 \cos z_R}\right]. \tag{B.50}$$

Here $v_0$ and $\left(\frac{dv}{dt}\right)_0$ are the observed velocity and deceleration, and $z_R$ is the zenith distance of the radiant, or the angle between the velocity vector and the direction toward the center of the Earth. In practice, this equation is sometimes additionaly simplified. For instance, the Advanced Meteor Orbit Radar (AMOR) group is using the empirical correction

$$v_\infty^2 = v_0^2 + 0.81 v_0^{1.6}, \tag{B.51}$$

where all velocities are given in units of km/s [2].

A slight improvement to precision when calculating the effect of the atmosphere on the motion of the meteoroid was discussed by Pecina, 1991 [101]. His approach was to numericaly integrate the equation of motion (B.49), taking into the account the atmospheric drag and the Earth's gravity. The integration was done from the observed heights to the standard reference level of 150 km, where the drag is outweighted by the effect of gravity. His results suggest that the there is a small difference compared to the classical method described above.

### B.4.2 Velocity Correction due to the Earth's Rotation

Since the Earth rotates about its polar axis with period $T = 24$ h, the motion of the observing station has to be taken into account. In the case of observing a distant star, the velocity of the observer causes an apparent shift to a maximum correction of about 0.0008333° at the equator. In the case of a meteor, the corrections are higher by a few orders of magnitude because the velocity of the meteoroid is much smaller than the speed of light. The standard equations for the diurnal aberration [36] lead to

$$\Delta\alpha_R = -\frac{1594.45\mathrm{km/s}}{v_g'}\frac{\cos\varphi_O\cos\theta_R}{\cos\delta_R} \tag{B.52}$$

$$\Delta\delta_R = -\frac{1594.45\mathrm{km/s}}{v_g'}\cos\varphi_O\sin\theta_R\sin\delta_R, \tag{B.53}$$

where $\Delta\alpha_R$ and $\Delta\delta_R$ are the corrections (in angular minutes) for the observed equatorial coordinates of the radiant $(\alpha_R,\ \delta_R)$. The radiant's hour angle $\theta_R$ is given by $\theta_R = GMST - \alpha_R$. The geographic coordinates of the observation site are $(\lambda_O,\ \varphi_0,\ r_0)$.

### B.4.3 Velocity Correction due to Earth's Gravitational Field

The perturbation of a meteoroid's trajectory due to the influence of Earth's gravitational field will be discussed in this subsection. In general, a trajectory with orbital perturbations cannot be solved analytically. The standard approach used for the tracking of comets, is to numericaly integrate the differential equations of motion for the entire period of time [21]. The usual approach in meteor astronomy is to use the so-called zenith attraction: the radiant is effectively shifted toward the zenith [59].

Assuming that the meteoroid trajectory is perturbed only by Earth's gravity, and that the trajectory is hyperbolic, the meteoroid will be seen to be coming from a direction tangent to the hyperbola. If the geographic coordinates of the observation site are $(\varphi_O,\ \lambda_O,\ r_O)$, the initial speed $v_g$ will be changed into $v_g'$ accoring to the relation [59]

$$v_g^2 = v_g'^2 - 2gr, \tag{B.54}$$

where $g$ is the gravitational acceleration and $r$ is a distance from the center of the Earth to the meteoroid, $r = r_O + h$. Assuming that the Earth is not a perfect sphere, but rather, an ellipsoid, the gravitational acceleration varies with the height $h$ as

$$g = g_e \left(1 + \frac{g_0 - g_e}{g_e} \sin^2 \varphi_O\right) \left(\frac{r_O}{r_O + h}\right)^2, \tag{B.55}$$

where $g_0 = 9.823\,\mathrm{m/s^2}$ and $g_e = 9.789\,\mathrm{m/s^2}$ are the values of the gravitational acceleration at the surface of the Earth with latitudes of 90° (poles) and 0° (equator), respectively. The distance, $r_0$, between the observing station and the center of the Earth is

$$r_O = \frac{a_1}{\cos \varphi'_O \sqrt{1 + \frac{a_1^2}{b_1^2} \tan^2 \varphi'_O}}, \tag{B.56}$$

where the angle $\varphi'_O$ is the geocentric latitude given as a function of the geographical latitude $\varphi_O$:

$$\varphi'_O = \varphi_O - 695''.66 \sin 2\varphi_O + 1''.17 \sin 4\varphi_O. \tag{B.57}$$

$a_1 = 6.378136 \times 10^6$ m and $b_1 = 6.356750 \times 10^6$ m are the major (at the equator) and minor (at the poles) semiaxes of the Earth.

The position of the radiant is shifted by the angle $\Delta z_R$ for a fixed meridian, where

$$\tan\left(\frac{1}{2}\Delta z_R\right) = \frac{v_g - v'_g}{v_g + v'_g} \tan\left(\frac{1}{2} z_R\right). \tag{B.58}$$

The true position of the radiant is equal to $\Delta z_R + z_R^{observed}$. Formula (B.58) was derived in 1867 by Schiaparelli [59]. It shows that the zenith correction depends on the zenith angle of the radiant and the meteor's relative velocity. For meteors with a radiant close to the horizon $\Delta z_R \sim 90°$, this correction can reach a few degrees.

One of the numerical methods for the determination of the orbital elements of a meteoroid influenced by the gravitational forces of the Earth and the Sun is described in [102]. The diferential equations of motion taking into account the two centers of gravity, are integrated backward in time, from the time the meteoroid was 150 km from the surface of the Earth, to the moment the meteoroid was at least $10^7$ km away from the Earth.

In this work we use an approximate solution as follows. A meteoroid moves from a region of space where the Sun's gravity plays the major role into a region where the gravitational force of the Earth is stronger. The "spheres of activity" of each body can be estimated using the equation of motion (B.6). If the mass of the second center of gravity (the Earth) is small compared to the mass of the first center of gravity (the Sun), the sphere of activity of the smaller body has radius:

$$\rho_{ES} = r_E \left( \frac{m_E}{M_S} \right)^{2/5} . \tag{B.59}$$

Calculated in this way, the radius of the Earth's sphere of activity is $\sim$ 925200 km. For reference, the radius of the Moon's sphere of activity is $\sim$ 66000 km [91]. Inside the Earth's sphere of activity, the orbit is calculated using only the Earth's gravity. At a distance of $\rho_{ES}$ a switch to the orbital elements inside the Solar sphere of activity has to be performed.

# Bibliography

[1] Badger, D. 2002, *Fine Structure in Radio Meteor Showers*, Ph. D. dissertation, University of Adelaide, Australia;

[2] Baggaley, W. J, *et. al.* 1994, *Q. J. R. astr. Soc.* **35**, 293;

[3] Baggaley, W. J. 2000, *J. Geophys. Res*, **105**, 10353;

[4] Belkovich, O. I, Nedeljković, S. and Verbeeck, C. 2006, *Proc. of the Radio Meteor School 2005*, 55, Oostmalle, Belgium;

[5] Bond, V. R. 1996, *Modern Astrodynamics: fundamentals and perturbation methods*, Princeton University Press;

[6] Borovička, J. 1993, *Astron. Astrophys*, **279**, 627;

[7] Bretagnon, P. and Francou, G. 1987, *Astronomy and Astrophysics*, **202**, 309;

[8] Bretagnon, P. and Simon, J-L. 1986, *Planetary Programs and Tables from -4000 to +2800*, Willmann-Bell, Richmond, Va;

[9] Bronshten, V. A. 1983, *Physics of meteoric phenomena*, D. Reidel Pub. Co, Holland;

[10] Campbell-Brow, M. D. and Jones J. 2006, *Mon. Not. R. Astron. Soc*, **367**, 709;

[11] Web page: Canadian Government Broadcasting Database (2005): `http://strategis.ic.gc.ca`;

[12] Carbognani, A, De Meyere, M, Foschini, L. and Steyaert, C. 2000, *Astron. Astrophys*, **361**, 293;

[13] Ceplecha, Z. 1992, *Astron. Astrophys*, **263**, 361;

[14] Ceplecha, Z, Spurny, P, Borovicka, J. and Keclikova, J. 1993, *Astron. Astrophys*, **279**, 615;

[15] Ceplecha, Z, Borovicka, J, Elford, W. G, ReVelle, D. O, Hawkes, R. L, Porubcan, V. and Simek, M. 1998, *Space Science Reviews*, **84**, 327;

[16] Chippendale, A. P. and Subrahmanyan, R. 2004, *Proc. of the Workshop on Applications of Radio Science*, Hobart, Australia;

[17] Kaplan, H. 2005, *Circular*, **179**, U.S. Naval Observatory, Washington, D.C.

[18] Cook, A. F. 1973, *Proc. of IAU Colloq. 13*, Albany, 183;

[19] Dicke, R. H, Peebles, P. J. E, Roll, P. G. and Wilkinson, D. T. 1965. *ApJ*, **142**, 414;

[20] Djorgovski, S. G, Castro, S, Stern, D. and Mahabal, A. A. 2001, astro-ph/0108009v2;

[21] Dubyago, A. D. 1961, *The Determination of Orbits*, The Macmillan Company, New York;

[22] Dwarakanath, K. S. and Udaya Shankar, N. 1990, *J. Astrophys. Astr*, **11**, 323;

[23] Dyson, J.D. 1959, *IRE Trans. Antennas Propagat*, **7**, 329;

[24] Elford, W. G. 1995, *Earth, Moon and Planets*, **71**, 245;

[25] Elforand, W. G. and Elford, M. T. 2001, *Proc. of the Meteoroids 2001 Conf. ESA SP-495*, Swedish Institute of Space Physics, Kiruna, Sweden;

[26] Elford, W. G. and Campbell, L. 2001, *Proc. of the Meteoroids 2001 Conference*, ESA SP-495, 419;

[27] Eshleman, V. R. 1953, *Trans. IRE*, **AP1**, 37;

[28] Eshleman, V. R. 1957, *J. Atmos. Terr. Phys*, **10**, 57;

[29] Eshleman, V. R and Manning, L. A. 1954, *Proc. of the IRE*, 530;

[30] Fan, X, Carilli, C.L. and Keating B. 2006, *Annu. Rev. Astro. Astrophys.* **44**, 415;

[31] Field, G. B. 1958, *Proc. I.R.E.* **46**, 240;

[32] Foschini, L. 1999, *Astron. Astrophys*, **341**, 634;

[33] Gamow, G. 1948, *Nature*, **162**, 680;

[34] Gnedin, N. Y. 2001, astro-ph/0110290v1;

[35] Goldberg, R. A. and Aikin, A. C. 1973, *Science*, **280**, 294;

[36] Green, R. M. 1985, *Spherical astronomy*, Cambridge University Press;

[37] Greenhow, J. S. and Neufeld, E. L. 1955, *J. Atmos. Terr. Phys*, **6**, 133;

[38] Grun, E. and Zook, H. A. 1980, *Solid Particles in the Solar System*, D. Reidel Publ. Co, Dordrecht, Holland;

[39] Gunst, A, van der Schaaf, K. and Bentum, M.J. 2006, *Proc. from SPS-DARTS 2006, the second annual IEEE BENELUX/DSP Valley Signal Processing Symposium*, Antwerp, Belgium.

[40] Haslam,C.G.T, Stoffel,H, Salter,C.J. and Wilson,W.E. 1982, *A&AS*, **47**, 1;

[41] Hines, C. 0. 1955, *Can. J. Phys*, **33**, 493;

[42] Hines, C. 0. 1958, *Can. J. Phys*, **36**, 117;

[43] Hines, C. O. and Forsyth, P. A. 1957, *Can. J. Phys*, **35**, 1033;

[44] Hocking, W. K, Thayaparan, T. and Jones, J. 1997, *Geophys. Res. Lett*, **23**, 2977;

[45] Hogan, J. 2006. *Nature*, **444**, 138;

[46] Hunsucker, R. D. and Hargreaves, J. K. 2003, *The High-Latitude Ionosphere and its Effects on Radio Propagation*, Cambridge University Press;

[47] IAU FITS Working Group, 2006. *Definition of the Flexible Image Transport System (FITS)*, FITS Support Office, NASA;

[48] Intel C++ Compiler for Linux Systems User's Guide, 2003, Intel Corporation;

[49] International Telecomunication Union Recommendation ITU-R P.843-1;

[50] Janchesa, D. and Chaub J. L. 2005. *Journal of Atmospheric and Solar-Terrestrial Physics*, **67**, 1196;

[51] Janches, D, Mathews, J. D. Meisel, D. D. and Zhou, Q.-H. 2000, *Icarus*, **145**, 53;

[52] Jenkins, H. H. 1991, *Small-Aperture Direction-Finding*, Artech House Inc, USA;

[53] Jones, W. and Jones, J. 1990, *J. Atmos. Terr. Phys*, **52**, 185;

[54] Jones, W. and Jones J. 1990, *Planet. Space Sci*, **38**, 55;

[55] Jones, J. and Jones W. 1990, *Planet. Space Sci*, **38**, 925;

[56] Jones, J. and Jones W. 1991, *Planet. Space Sci*, **39**, 1289;

[57] Jordan, C. E. and Balmain, K. G. 1986. *Electromagnetic Waves and Radiating Systems*, Prentice Hall, New Delhi, India;

[58] Kaiser, T. R. and Closs, R. I. 1952, *Philos. Mag*, **43**, 1;

[59] Katasev, L. A. 1964, *Photographic Methods in Meteor Astronomy*, Israel Program for Scientific Translations;

[60] Kirkpatrick, S, Gelatt Jr. C. D. and Vecchi, M. P. 1983, *Science*, **220**, 671;

[61] Kraus, J. D. 1986, *Radio Astronomy*, Cygnus-Quasar Books, Powell, Ohio;

[62] Kraus, J. D. 2002, *Antennas*, McGraw-Hill, New York;

[63] Kuipers, J. B. 1999, *Quaternions and rotation sequences : a primer with applications to orbits, aerospace, and virtual reality*, Princeton University Press;

[64] Landgraf, M, Baggaley, W. J, Grun, E, Krger, H. and Linkert, G. 2000, *J. Geophys. Res*, **105**, 10343;

[65] Lawson, K. D, Mayer, C. J, Osborne, J. L. and Parkinson, M. L. 1987. *Mon. Not. R. Astron. Soc*, **225**, 307;

[66] Loeb, A. and Barkana, R. 2001, *ARA&A*, **39**, 19;

[67] Love, S. G. and Brownlee D. E. 1993, *Science*, **262**, 550;

[68] Lovell, A. C. B. 1954, *Meteor Astronomy*, Clarendon Press, Oxford;

[69] Madau, P, Meiksin, A. and Rees, M. J. 1997, *ApJ*, **475**, 429;

[70] Manning, L. A. 1958, *J. Geophys. Res*, **63**, 181;

[71] Manning, L, Villard, O, Jr. and Peterson, A. 1952. *Antennas and Propagation, Trans. IRE*, **3**, 230;

[72] McBeath, A. 2006. *IMO Meteor Shower Calendar 2006*, IMO INFO;

[73] McCormack, J. W. 1974. *ASAP*, Master's Thesis, Naval Postgraduate School, Monterey, California;

[74] McKinley, D. W. R. 1961, *Meteor Science and Engineering*, McGraw-Hill Book Company;

[75] Meeus, J. 1998, *Astronomical Algorithms*, Richmond, Va. Willmann-Bell;

[76] Meiksin, A. 1999, *Perspectives on Radio Astronomy - Science with Large Antenna Arrays*, Netherlands Foundation for Research in Astronomy;

[77] Mathews, J. D, Janches, D, Meisel, D. D. and Zhou, Q.-H. 2001, *Geophys. Res. Lett*, **28**, 1929;

[78] Milić, B. 1989, *Osnove Fizike Gasne Plazme* (in Serbian), Gradjevinska Knjiga, Beograd, Srbija;

[79] Milić, B. 1997, *Njutnova Mehanika* (in Serbian), Studentski Trg, Beograd;

[80] Milogradov-Turin, J. 1974, *Mem. Soc. Astron. Ital.* **45**, 85;

[81] Miović, V. 2005, *personal communication*;

[82] Mukundan, R. 2002, *Proc. of the 7th Asian Technology Conference in Mathematics*, Chiang Mai, Thailand;

[83] Murray, N, Weingartner, J. C. and Capobianco, C. 2004, *ApJ*, **600**, 804;

[84] MWA Report 2, 2005. *Mileura Widefield Array Low Frequency Demonstrator, Early Deployment Second Campaign*, Initial Report 16 May 2005, taken from `http://www.haystack.edu/ast/arrays/mwa/News items/ED2 report1.pdf`;

[85] Nautical Almanac Office, *The Astronomical Almanac*, Nautical Almanac Office, United States Naval Observatory;

[86] Nedeljković, S. et al. 2003, *Proc. of the Fifth General Conference of the Balkan Physical Union*, SP02 - 009;

[87] Nedeljković, S. 2006, *Proc. of the International Meteor Conference 2005*, 16, Oostmalle, Belgium;

[88] Nedeljković, S. 2006, *Proc. of the Radio Meteor School 2005*, 108, Oostmalle, Belgium;

[89] Nedeljković, S. and Miović, V. 2005, *Proc. IAU Colloquium No. 197*, 405;

[90] Nedeljković, S. and Netterfield, C. B. 2006. *Publ. Astron. Obs. Belgrade*, **80**, 179;

[91] Nenadović, M. 1979, *Osnovi Kosmičkog Leta* (in Serbian), Institut tehničkih nauka SANU, Beograd;

[92] Newton, I. 1687, *The Principia*, University of California Press, 1999;

[93] Nicol, E. J, MacFarlane, J. and Hawkes, R. L. 1985, *Planetary and Space Science*, **33**, 315;

[94] U.S. Dept. of Commerce, NOAA, Space Environment Center web page, 2004, `http://www.sec.noaa.gov/ftpdir/indices/events/20040730events.txt`;

[95] Novikov, G. G, Blokhin, A. V. and Pecina, P. 1986, *Bull. Astron. Inst. Czeshosl*, **37**, 189;

[96] Press, Wm. H, Flannery, B, Teukolsky, S. and Vettering, Wm. 1986, *Numerical Recipes*, Cambridge University Press, New York;

[97] Oberg, E, Jones, F. D, Horton, H. L. and Ryffell, H. H. 2000. *Machinery's Handbook*, Industrial Press;

[98] Oetting, J. D. 1980, *IEEE Transactions on Communications*,**28**, 1599;

[99] Olech, A. and Wišniewski, M. 2002. *Astronomy and Astrophysics*, **384**, 711;

[100] Parks, G. K. 1991, *Physics of Space Plasmas*, Addison-Wesley Publishing Company;

[101] Pecina, P. 1991, *Bull. Astron. Inst. Czechosl.* **42**, 307;

[102] Pecina, P. 1993, *Planet. Space Sci.* **42**, 677;

[103] Peebles, P. J. E. 1993, *Principles of Physical Cosmology*, Princeton University Press, Princeton;

[104] Pen, U-L, Wu, X-P. and Peterson, J. 2004. `astro-ph/0404083`;

[105] Pen, U-L. 2005. *personal communication*;

[106] Penzias, A. A. and Wilson, R. W. 1965. *ApJ*, **142**, 419;

[107] Picone, J.M, Hedin, A.E, Drob, D.P. and Aikin A.C. 2002, *J. Geophys. Res*, **107**, 1468;

[108] Poole, L. M. G. 1997, *Mon. Not. R. Astron. Soc*, **290**, 245;

[109] Rawer, K. 1993, *Wave Propagation in the Ionosphere*, Kluwer Academic Publishers;

[110] Rees, W. G. 1991, *Eur. J. Phys.* **12**, 96;

[111] Robson, R. E. 2001, *Phys. Rev. E*, **63**, 026404;

[112] Rubini, A. 2001. *Linux Device Drivers, 2nd edition*, O'Reilly & Associates, Inc;

[113] Rudie, N. J. 1967, *The relative distribution of observable meteor trails in forward-scatter meteor communications*, Ph. D dissertation, Montana State University, Bozeman, Montana;

[114] Rumsey, V.H. 1957. *Frequency Independent Antennas, IRE Intern. Conv. Record*, 114;

[115] Rutledge, D. D. 1999, *The Electronics of Radio*, Cambridge University Press;

[116] Schanker, J. Z. 1990, *Meteor Burst Communications*, Artech House, Inc;

[117] Schilling, L. D. 1993, *Meteor Burst Communications: Theory and Practice*, Wiley-Interscience Publication;

[118] Schwieters, J, Cramer, H.G, Heller, T, Jurgens, U, Niehuis, E, Zehnpfenning, J. and Benninghoven, A. 1991, *Journal of Vacuum Science and Technology*, **A9**, 2864;

[119] Shapiro, P. R. 2001. astro-ph/0104315;

[120] Shaver, P. A. and Bruyn, A. G. 1999. *Perspectives on Radio Astronomy - Science with Large Antenna Arrays*, Netherlands Foundation for Research in Astronomy;

[121] Shaver, P. A, Windhorst, R. A., Madau, P. and Bruyn A. G. 1999, *Astron. Astrophys*, **345**, 380;

[122] Simovljević, J. L. 1977, *Osnove Teorijske Astronomije* (in Serbian), Gradjevinska Knjiga, Beograd;

[123] Singer, W, von Zahn, U. and Wei, J. 2004. *Atmos. Chem. Phys.* **4**, 1355;

[124] SKA coolaboration, 2004. *Science with the Square Kilometre Array*, eds: C. Carilli, S. Rawlings, New Astronomy Reviews, **48**, Elsevier;

[125] Smith, S. W. 1996, *The Scientist and Engineer's Guide to Digital Signal Processing*, on-line book `http://www.dspguide.com`;

[126] Smith, W. W. and Smith J. M, 1995. *Handbook of Real-Time Fast Fourier Transforms*, IEEE Press, New York;

[127] Songaila, A, Hu, E. M., Cowie, L. L. and McMahon, R. G. 1999, *ApJ*, 525, L5;

[128] Sophocles, J. 1996. *Introduction to Signal Processing*, Prentice-Hall Inc, New Jersey;

[129] Spergel, D. N. et al. (WMAP collaboration), 2003. *ApJ. Suppl.* **148**, 175;

[130] Industry Canada, Spectrum Management and Telecommunication web site, 2006, `http://strategis.ic.gc.ca`;

[131] Straw, R. D. 2003. *The ARRL Antenna Book*, American Radio Relay League;

[132] Sugar, G. R. 1964, *Proc. IEEE 52*, 116;

[133] Suleymanova, S, Verbeeck C. and Wislez, J-M. 2006, *Proc. of the Radio Meteor School 2006*, Netterland;

[134] U.S. Naval Observatory, 2006, *Approximate Solar Coordinates*, web page: `http://aa.usno.navy.mil/faq/docs/SunApprox.html`;

[135] Szasz, C. et al. 2004. *Earth, Moon, and Planets*, **95**, 101;

[136] Thomas, R. M, Whitham P.S. and Elford, W. G. 1988, *J. Atmos. Terr. Phys*, **50**, 703;

[137] Tozzi, P., Madau, P., Meiksin, A. and Rees, M. J. 2000. *ApJ*, **528**, 597;

[138] Triglav-Čekada, M. and Arlt, R. 2005. *WGN, Journal of the International Meteor Organization*, **33**, 129;

[139] Triglav-Čekada, M. 2006, *personal communication*;

[140] Audio Division of the Media Bureau, USA federal government, FMQ FM Radio Database Query, 2006, `http://www.fcc.gov/mb/audio/fmq.html`;

[141] Vaseghi, S. V. 2000, *Advanced Digital Signal Processing and Noise Reduction*, John Willey & sons, LTD;

[142] Venkatesan, A. 2002, astro-ph/0109129v2;

[143] Verbeeck, C. 1995, *WGN*, **23**, 236;

[144] Verbeeck, C. 1995, *Proc. IMC 1996*, Apeldoorn, Netherlands, 122;

[145] Verniani, F. 1973, *J. Geophys. Res*, **78**, 8429;

[146] Voloshchuk, I. I. and Kashcheev, B. L. 1991, *Astronomicheskii Vestnik*, **25**, 453;

[147] von Zahn, U. 2005, *17th ESA Symposium on European Rocket and Balloon Programmes and Related Research*, ESA SP-590, Sandefjord, Norway, 33;

[148] Webster, A. R, Brown, P. G, Jones, J, Ellis, K. J. and Campbell-Brown, M. 2004, *Atmos. Chem. Phys. Discuss*, **4**, 1181;

[149] Weitzen, J. A. 1990, *IEEE Transactions on Communications*, **38**, 426;

[150] Wikipedia, 2005, *Kepler's laws of planetary motion*, web page: `http://en.wikipedia.org/wiki/Kepler's_laws_of_planetary_motion`;

[151] Wills, R. G. 1985. *Communication & Broadcasting*, **9**, 39;

[152] Wislez, J-M. 1995, *Proc. IMC 1995*, Brandenburg, Germany;

[153] Wouthuysen, S. A. 1952, *ApJ*, **57**, 31;

[154] Weather Underground website (2006): `http://www.wunderground.com/`;

[155] Yamamoto, M.-Y. 2005, *personal communication*;

[156] Yeh, S. Y. and Mei, K. K. 1967. *IEEE Trans. Antennas Propagat*, **15**, 634;

[157] Yeh, S. Y. and Mei, K. K. 1968. *IEEE Trans. Antennas Propagat*, **16**, 14;

[158] Zigo, P. 2006, *personal communication*;